学位論文

Structures within the intra-cluster medium of an early phase cluster merger, CIZA J1358.9-4750

(初期衝突銀河団 CIZA J1358.9-4750 のプラズマの空間構造)

平成 29 年 12 月博士 (理学) 申請
東京大学大学院理学系研究科
物理学専攻
加藤佑一

Abstract

Clusters of galaxies are the largest scale structure in the universe as a self-gravitational system. The size and mass reach 1 Mpc and 10^{14-15} $M_{\odot}$, respectively. It consists of dark mater, intra-cluster medium (ICM) and galaxies, individually contributing about 75%, 20%, and 5%, respectively. In other words, most of the baryon resides in the ICM. Reflecting the depth of the gravitational potential, the ICM has a temperature of 10^{7-8} K, and hence is a strong X-ray emitter. Clusters of galaxies are growing with in-fall of surrounding matters. It also merges with another cluster. The merging events are the largest energy release phenomena in the Universe. The gravitational energy released in the event reaches up to 10^{57} J, and a part of the huge kinetic energy (originally gravitational potential) is injected into the ICM. Merging induces several kinds of observable structures in it, such as shocks, cold fronts and mixing gases. The shocks convert the injected energy into thermal energy of the ICM, particle acceleration and magnetic field amplification.

A half of clusters of galaxies show some traces of mergers. But most of them are in late-phase merger, in which the cores of clusters of galaxies crossed each other. Dozens of such clusters are reported to show clear signatures of shocks and cold fonts. However, in most cases, the shocks have already traveled a long distance and reached low density ICM regions and hence X-ray dim. Therefore, the detailed investigation of the shocks have been hampered because of insufficient statistics and background noise in X-ray observations.

In an early-phase merger, shocks located around clusters' cores reside in the ICM high-density region and thus bright in X-rays. Therefore, the early-phase systems are suitable objects to solve above problems. Up to date, several examples of nearby early-phase systems have been investigated with X-ray observation. None of them, however, show clear signature of shocks and cold fronts.

In this thesis, we investigated CIZA J1358.9-4750, which is a promising candidate of an early-phase cluster merger. The object has two clusters' cores with a distance of 1.1 Mpc, and bright X-ray emission between them. The morphology seems like a bridge constructed between the cores. We revealed that the bridge structure has high temperature and density, compared to the opposite sides of individual cluster cores with Suzaku. These characteristics are consistent with the target being a near-by early-phase merger.

Temperature, pressure and entropy distribution show transitions within the bridge region. We also extracted the X-ray brightness distribution in the bridge region with Chandra and XMM-Newton, which both have better angular resolution than Suzaku. Both of them indicate two jumps forming a hump structure right on those transitions found with Suzaku. The results can be well explained if there are two shocks running opposite direction each other, and we are observing the shocks almost from perpendicular direction. Rankine-Hugoniot relation applied to the temperature jumps provides the Mach number of ~ 1.4. On the assumption of symmetric collision, we were also able to estimate the age of shocks as 55 Myr.

From the ICM temperature of the two clusters' cores and the shocks condition, it is suggested that CIZA 1358.9-4750 is a major merger now colliding with a speed of 1660 km s^{-1}. Observed from the center of gravity, the young shock is propagating at 1300 km s^{-1} in the sky plane.

The hot belt in the bridge region extends to north-east direction, but is weak in the south-west direction. In addition, in the north east region, we detect a clear jump in the X-ray properties. The temperature and density decline rapidly at a certain distance toward north-east. The fact suggests the heated plasma is erupted toward the north-east direction. To explain the east-west difference in the shock geometry, a simple model assuming weak rotation of the clusters is considered as a candidate.

With Chandra, we also extracted X-ray brightness distribution around cores. Then, it is found that both cores have brightness transitions. These are signatures of cold fronts. Therefore, cold fronts are also induced within the object.

With our X-ray analysis, the CIZA 1358,9-4750 cluster is revealed to be an early-phase major merger, located near to us (distance 310 Mpc), with clear twin shocks observed almost perpendicular to the merger axis. It shows bright post-shock region, and hence important for future X-ray observations, such as high-resolution X-ray spectroscopy with XARM and ATHENA.

Contents

List of Figures

List of Tables

Chapter 1

Introduction

The universe is evolving together with the growth of fluctuation driven by gravitational instability from its initial homogenous state. Smaller clumps are constructed first and then larger structures are formed. Therefore, the universe has a characteristic feature called hierarchical structure.

The celestial objects sitting in the thrones of the hierarchical structure are clusters of galaxies. Clusters of galaxies are the largest self-gravitational structure with a typical size of 1 Mpc. It takes several Gyr to be formed and still growing up to date following the hierarchical structure formation. The typical mass of 10^{14-15} $M_{\odot}$ is accomplished via successive merger and matter accretion. The components of clusters of galaxies are dark matter, intracluster medium (ICM) and galaxies. Around $\sim$ 80 % of the total mass is the dark matter which is invisible with any electro-magnetic emission. About 20 % is the ICM captured by the huge gravitational potential of the dark matter. The residual a few percent of the mass is galaxies which are wandering within the ICM.

The ICM has a temperature as high as 10^{7-8} K, which reflects the potent gravity potential, with rarefied density of 10^{-2}–10^{-4} cm^{-3}, and is bright at X-ray wavelengths. The tremendous size of the system makes clusters of galaxies one of the brightest objects in the universe. The temperature and density parameters make the ICM the most ideal non-collisional plasma.

In the process of cluster evolution, two (or more) clusters can collide and merge. In the event of merging of clusters, gravitational energy of 10^{57-58} J is released, which is comparable to 100 million supernova explosions. The mergers induce various phenomena in the ICM such as shocks, cold fronts both as large as a few Mpc in their size, and gas mixing. The former one is activated because the colliding velocity exceeds the sound velocity of the ICM. The cold front is generated by ram pressure. Because these dynamical structures within the ICM reflects the micro-physics of an ideal plasma in this large scale, astrophysicists tried to shed light on those phenomena from observations and numerical simulations.

Although many efforts have been devoted to understanding the energy release or dissipation within the ICM, many questions are still remained. For example, ratio of amount of energy injected from the shock into individual forms such as thermal heat, magnetic field,

particle acceleration and turbulences, is not yet known. The largest obstacle to tackle the above questions is the low surface brightness of those systems in X-ray bands which prevent us from detailed analysis of the ICM behavior. This is because almost all merging clusters known to date, in particular those near-by which are easy to be observed in detail, are objects in which clusters' cores has already crossed each other. In these"late phase mergers", the shocks in the ICM have been already reached the outermost and dim regions of the cluster, and mixing of the ICM is so significant that estimating the initial condition of the merger is already difficult in many cases (e.g. Briel et al. 2004, Nakazawa et al. 2009, Finoguenov et al. 2010, Akamatsu et al. 2013). In other words, it is not only difficult to measure the shock structure itself, but also to estimate the initial kinetic energy. Therefore, objects in the early phase of the merger, in which clusters' cores have not yet passed each other, is very important. In such a system, the initial merger condition can be traced back because of less mixing of the ICM, and the shocks are located within regions much near the center of the clusters where the ICM density is relatively high and hence its X-ray emission is bright.

In this thesis, we investigated a cluster of galaxies CIZA J1358.9-4750, a candidate of an early phase merger. In the system, two clusters are located with a distance of 1.1 Mpc each other. The intermediate region between the clusters has a rich X-ray emission caused by the interaction. In order to inspect the existence of shocks and cold fronts within the ICM, we conducted observations with three latest X-ray observatories, Suzaku, Chandra, and XMM-Newton. With Suzaku, the ICM parameters distribution such as temperature, density, pressure and entropy are derived all over the system, out to 1.2 Mpc. Chandra and XMM-Newton are utilized to understand fine structures of the object.

Noted, in this thesis, Λ CDM model is assumed with parameter of Ω_M=0.3, Ω_Λ=0.7 and H_0=70 km s^{-1} Mpc^{-1}. Therefore, the distance of $1''$ corresponds to 80.2 kpc with redshift of 0.07. Error bars are shown with 68% confidence (1σ) level for one parameter, otherwise noted.

Chapter 2

Review

2.1 The structure of clusters of galaxies

2.1.1 The history of cluster of galaxies

The research of clusters of galaxies starts from optical band by identifying systems containing large population of galaxies, as the name indicates. The Virgo cluster of galaxies has already been discovered in 1781 as the first example, by Charles Messier, an astronomer in France.

Because a cluster of galaxies is a gravity bounded system, it reaches dynamical equilibrium after a certain period of time has elapsed. Assuming equilibrium, we can estimate mass of a cluster from Virial theorem as,

$$M = \frac{2\langle v^2 \rangle}{G\langle 1/r \rangle}. \tag{2.1}$$

Here, $\langle v^2 \rangle$ is the average root mean square of particles' relative velocity weighted by masses, $\langle 1/r \rangle$ is the inverse of mean distance between the particles, and G is the gravitational constant. The method was first applied with the line of sight velocity of galaxies which belongs to the cluster by Zwicky (F.Zwicky 1937). The mass of galaxies is able to be derived in the same way using the velocity of stars within the system. Then, he also compared the mass-luminosity ratio, M/L, of clusters of galaxies to galaxies and found that the former has a few hundreds times larger value. M/L of 244 $h\ M_\odot/L_\odot$ was obtained for clusters of galaxies in a recent study (Andernach et al. 2005), while 5–15 $h\ M_\odot/L_\odot$ was for galaxies (Binney et al. 1987). Here, h is hubble constant in unit of 70 km s^{-1} Mpc^{-1}, and $M_\odot$, $L_\odot$ are mass and luminosity in unit of solar, respectively. The results implied clusters of galaxies are filled with matters invisible in the optical band.

In 1967, an aerobee rocket was lunched from White Sands Missile Range to detect X-ray emission from the Virgo cluster. Surprisingly, it was discovered that M87 galaxy in the cluster is bright in X-ray with luminosity of 7×10^{42} erg s^{-1} in the energy band of 1.5–6.0 keV, which is six orders of magnitude larger than the Club neubla, a well-known bright X-ray source, which is a pulsar-wind nebula in our galaxy (Buram et al. 1967). Clusters of galaxies became

the first identified objects as extragalactic X-ray sources. Uhuru, the first X-ray satellite, was lunched in 1970 as a X-ray sky survey mission. It revealed clusters of galaxies are bright in X-ray band commonly. The mechanism of X-ray emission, however, was not clear then. There are three models to explain the strong X-ray emission; (1) thermal emission from hot plasma gas, ICM. (2) inverse Compton scattering emission of cosmic microwave background (CMB) by relativistic non-thermal (∼GeV) electrons, and (3) superposition of emission from compact sources such as galactic nuclei or the binary compact objects. Ariel 5 rocket experiment ascertains line emission from Fe^{+24} and Fe^{+25} in the Perseus cluster. The detection of fluorescence lines from highly ionized Fe ions is a direct evidence of existence of hot and ionized gas within the cluster, and it is shown that thermal emission explanation is plausible.

In the thermal emission scenario, the thermal pressure has to balance the gravitational potential, which gives,

$$k_B T \sim G\frac{m_p M}{R_{cl}} \sim 2\left(\frac{2\mathrm{Mpc}}{R_{cl}}\right)\left(\frac{M_{cl}}{10^{14}M_\odot}\right)\ \mathrm{keV}, \tag{2.2}$$

in which k_B is Boltzmann constant, m_p is proton mass, and R_{cl} and M_{cl} are the radius and the total mass of the clusters of galaxies, respectively. The derived value of a few keV matches very well with the temperature obtained from the X-ray spectrum fitted with thermal bremsstrahlung. The spectrum also provides plasma density by assuming the volume of the system. The typical density of ICM is 10^{-3} cm^{-3}. The total mass of ICM can be estimated in assumption of spherical shape. The ICM mass integrated out to the Virial radius is typically 20-30% of the total gravitating mass. Although the ICM X-ray emission is virtually invisible in the optical band, the X-ray results confirmed ICM cannot be the "dark" mass, and hence the existence of the dark matter is show again. It was also confirmed from other phenomena such as rotating velocity of spiral galaxies, temperature fluctuation of CMB with WMAP and so on as well. As described above, clusters of galaxies came to be known as the system consisting of dark matter, ICM and several hundreds of galaxies.

The rough calculation of the numbers of clusters of galaxies in the universe is achievable in the ΛCDM model (e.g. Weinberg 2008). The current critical energy density is $\rho_{0,crit} = \frac{3H_0^2}{8\pi G} = 9.202\times10^{-23}h^2\ \mathrm{kg\ m}^{-3}$ from Friedmann equation. Here, H_0 is current hubble constant. The ratio of energy density of non-relativistic matter to $\rho_{0,crit}$ is $\Omega_M = 0.3$. If we assume all of the "non-relativistic matter" resides in clusters of galaxies, the age of universe, t_0=138 billion years, and the mass of clusters of galaxies of M_{cl} gives N_{cl}, number of clusters of galaxies in our universe as,

$$N_{cl} = \frac{\frac{4\pi}{3}(ct_0)^3\rho_{0,crit}\Omega_M}{M_{cl}} = 10^{9-10}\ \mathrm{universe}^{-1}. \tag{2.3}$$

Observationally, about 5000 clusters of galaxies have been found mainly with optical observations by 2000. A famous catalog is Abell/ACO catalog (Abell, Corwin and Olowin 1989),

which contains 2712 and 1364 systems in northern and southern sky, respectively. The catalogue is produced by Geroge Abell by visual inspection of an optical all-sky map image and includes most of the near-by ($z < 0.2$) clusters of galaxies.

2.1.2 Cluster dynamical evolution

Since clusters of galaxies grow by gravity, the dynamical evolution time scale is estimated from equations of motion as

$$t_{\rm dyn} \sim \sqrt{\frac{R_{cl}^3}{GM_{cl}}} \sim 40 \left(\frac{R_{cl}}{2{\rm Mpc}}\right)^{3/2} \left(\frac{M_{cl}}{10^{14} M_\odot}\right)^{-1/2} \text{ billion years.} \tag{2.4}$$

The value indicates clusters of galaxies are in the middle of evolution, even with the age of our universe. It is known that the arrangement of galaxies in the universe forms a characteristic shape called cosmic web or large scale structure. Clusters of galaxies are located just at the junctions of the cosmic web. Matter falls along the cosmic web into the cluster with their huge gravity. In some cases, clusters collide each other. This event is called cluster merger.

Let's assume two clusters as point sources to calculate the colliding velocity and the released energy in the event. The schematic colliding geometry is shown in Fig.2.1. Position and velocity of each cluster's center are represented as $\vec{r_1}$ (or $\vec{r_2}$), and $\vec{v_1}$ (or $\vec{v_2}$). Also their mass is denoted as M_1 (or M_2). Equations of motion for individual cluster are given as,

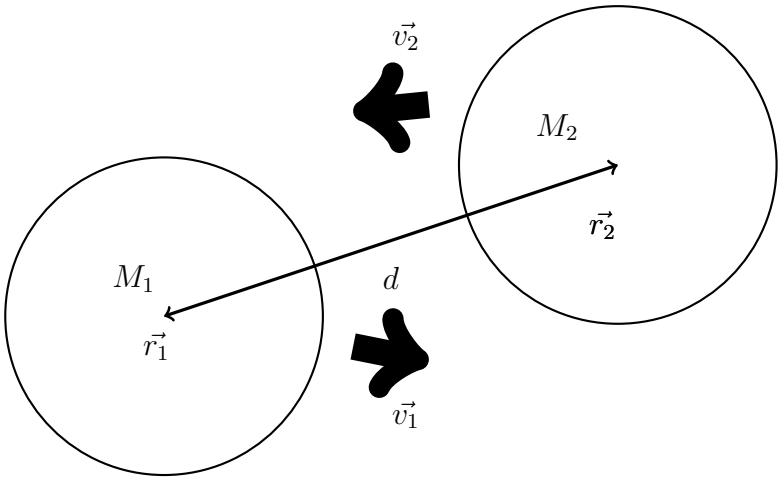

Figure 2.1: A schematic diagram of cluster merger having masses of M1, M2 and velocities $\vec{v_1}$, $\vec{v_2}$, respectively, with cluster center distance of d.

$$M_1 \frac{d\vec{v_1}}{dt} = -G \frac{M_1 M_2}{|\vec{r_1} - \vec{r_2}|^2} \frac{\vec{r_1} - \vec{r_2}}{|\vec{r_1} - \vec{r_2}|}, \tag{2.5}$$

$$M_2 \frac{d\vec{v_2}}{dt} = -G \frac{M_1 M_2}{|\vec{r_1} - \vec{r_2}|^2} \frac{\vec{r_2} - \vec{r_1}}{|\vec{r_1} - \vec{r_2}|}. \tag{2.6}$$

Subtracting (2.6) from (2.5) gives

$$\mu \frac{d}{dt}(\vec{v_1} - \vec{v_2}) = \frac{G(M_1 + M_2)}{d^2} \frac{(\vec{r_1} - \vec{r_2})}{d}. \tag{2.7}$$

Here, $\mu = \frac{M_1 + M_2}{M_1 M_2}$ and $d = |\vec{r_1} - \vec{r_2}|$ are reduced mass and the distance between clusters's center, respectively. Taking inner product with $\vec{v_1} - \vec{v_2}$ or cross product with $\vec{r_1} - \vec{r_2}$ on equation (2.7) provides energy and angular momentum conservation equations as below,

$$\frac{1}{2}\mu(\vec{v_1} - \vec{v_2})^2 - \frac{GM_1 M_2}{d} = const, \tag{2.8}$$

$$\mu(\vec{r_1} - \vec{r_2}) \times (\vec{v_1} - \vec{v_2}) = const. \tag{2.9}$$

The initial relative velocity, distances, and the angle between the relative velocity and position are v_0, d_0, and θ_0, respectively. At the distance d, the relative velocity and the angle between the relative velocity and position become v and θ. Applying the energy and angular conservation equations gives,

$$\frac{1}{2}\mu v_0^2 - G\frac{M_1 M_2}{d_0} = \frac{1}{2}\mu v^2 - G\frac{M_1 M_2}{d}, \tag{2.10}$$

$$\mu v_0 d_0 \sin\theta_0 = \mu v d \sin\theta. \tag{2.11}$$

Eliminating v_0 provides the colliding velocity from the above equations at arbitrary time,

$$v = \left(2G\left(M_1 + M_2\right) \frac{1}{d} \frac{1 - \frac{d}{d_0}}{1 - \left(\frac{d sin\theta}{d_0 sin\theta_0}\right)^2} \right)^{1/2} \tag{2.12}$$

$$= 2940 \left(\frac{M_1 + M_2}{10^{15} M_\odot}\right)^{1/2} \left(\frac{d}{1Mpc}\right)^{-1/2} \left(\frac{1 - \frac{d}{d_0}}{1 - \left(\frac{d sin\theta}{d_0 sin\theta_0}\right)^2} \right)^{1/2} \text{km s}^{-1}. \tag{2.13}$$

The point sources assumption is no longer correct when two clusters start contacting. The gravitational energy of when two clusters contact would yield a good approximation of the

released energy in the merger. Let's assume $M_{1,2} = 5.0 \times 10^{14}$ $M_\odot$ and $d = 1$ Mpc as a typical value and assume face-to-face geometry so that the third term becomes unity. The released energy is calculated as $E = \frac{GM_1M_2}{d} \sim 10^{57}$ J. Significant portion of this tremendous energy is injected into the Mpc-scale merger shocks in the ICM, as thermal heat, invoking turbulence, amplifying magnetic field, and accelerating particles. The shocks work as the largest (in both total energy and and its size) energy convertor in the universe. Merger does not only induce shocks in ICM but also causes cold fronts, which are contact discontinuities having identical pressure but different temperature in front and behind. Those phenomena also contain fundamental micro plasma physics implication.

2.1.3 Advantages of X-ray observations

As specified in Sec.2.1.1, the study of clusters of galaxies began with optical observation. X-ray observation, however, is indeed a powerful tool to analyze the objects. The X-rays from ICM is thermal emission, thus the emissivity is proportional to n_e^2. Assuming that electrons and galaxies density are proportional everywhere in the universe i.e. $\mathrm{n}_e \propto \mathrm{n}_{gal}$, the X-ray emissivity will be proportional to square of galaxies density. Meanwhile, optical emission is proportional to galaxies density. Comparing the signal level divided by the background (or free of source region) counts gives,

$$\mathrm{X-ray}: \quad \frac{\int_{-\mathrm{R_{cl}}}^{\mathrm{R_{cl}}} \mathrm{n}_{\mathrm{gal}}^2(\mathrm{cluster})\mathrm{dl}}{\int_0^{\mathrm{R_H}} \mathrm{n}_{\mathrm{gal}}^2(\mathrm{universe})\mathrm{dl}} \sim \frac{n_{gal}^2(\mathrm{cluster})}{n_{gal}^2(\mathrm{universe})}\frac{2R_{cl}}{R_H} \sim 1000, \tag{2.14}$$

$$\mathrm{Optical}: \quad \frac{\int_{-\mathrm{R_{cl}}}^{\mathrm{R_{cl}}} \mathrm{n}_{\mathrm{gal}}(\mathrm{cluster})\mathrm{dl}}{\int_0^{\mathrm{R_H}} \mathrm{n}_{\mathrm{gal}}(\mathrm{universe})\mathrm{dl}} \sim \frac{n_{gal}(\mathrm{cluster})}{n_{gal}(\mathrm{universe})}\frac{2R_{cl}}{R_H} \sim 1. \tag{2.15}$$

Here, R_H is the observational horizon. $R_H = c/H_0$ and about 3000 h^{-1} Mpc. n_{gal}(universe) and n_{gal}(cluster) are the average density of galaxies in universe and cluster, respectively. Those values are roughly $\mathrm{n}_{gal}(\mathrm{universe}) \sim 10^{-2}/(h^{-1}\mathrm{Mpc})^3$ and $\mathrm{n}_{gal}(\mathrm{cluster}) \sim 10/(h^{-1}\mathrm{Mpc})^3$, respectively. Thus, the contrast in X-ray is 1000 times stronger than optical band so that observing clusters of galaxies is much easier in X-ray band [1].

2.2 X-ray emission from ICM

The optical thickness of ICM is represented as

$$\tau = \int n_e \sigma_T ds = 2 \times 10^{-3} \left(\frac{n_e}{10^{-3}\mathrm{cm}^{-3}}\right)\left(\frac{l}{1\mathrm{Mpc}}\right) \ll 1, \tag{2.16}$$

[1] It originates from a intensive course in Tokyo Institute of Technology by Suto in 2002.

Here, n_e and σ_T are density of electrons and cross section of Thomson scattering, respectively. The number shows ICM is optically thin. ICM has also been thermalized, and ions within ICM are ionized via collisions with electrons mainly. Therefore, X-ray emissions from ICM are dominated by thermal bremsstrahlung continuum and line fluorescent emissions from ionized gas, such as He/H-like ions.

2.2.1 Thermal Bremsstrahlung

A continuum emission produced via deceleration of a charged particle by an electric field induced by another particle is called bremsstrahlung. In particular, the bremsstrahlung emission caused by maxwellian-distribution particles is called thermal bremsstrahlung. The emissivity is expressed as

$$\frac{dW(T,\omega)}{d\omega dV dt} = \frac{32\pi}{3}\sqrt{\frac{1}{6\pi}} n_i n_e \frac{Z^2 e^2}{\hbar c}\left(\frac{e^2}{m_e c^2}\right)^2 \left(\frac{m_e c^2}{k_B T}\right)^{\frac{1}{2}} \hbar c\, \bar{g}_{ff}\,(T,\omega)\, e^{-\frac{\hbar\omega}{k_B T}}. \tag{2.17}$$

Here, n_i, m_e and Z are ions density, mass of electrons and charge of ions, respectively. $\bar{g}_{ff}$ is a maxwellian-distribution velocity averaged Gaunt factor, which is roughly proportional to $h\nu^{0.4}$ in X-rays. An important feature is the emissivity depending on the factor of $e^{-\frac{\hbar\omega}{k_B T}}$. The continuum spectra are almost flat up to the cut off of the exponential so that it is possible to measure plasma temperature accurately if the wavelength which is comparable to the temperature of plasma is observed. Integrating the emissivity over wavelength yields the bolometric emissivity as

$$\frac{dW(T)}{dV dt} = \frac{32\pi}{3}\sqrt{\frac{1}{6\pi}} n_i n_e \frac{Z^2 e^2}{\hbar c}\left(\frac{e^2}{m_e c^2}\right)^2 \left(m_e c^2\right)^{\frac{1}{2}} (k_B T)^{\frac{1}{2}}\, c\, \bar{g}_B, \tag{2.18}$$

where $\bar{g}_B$ is frequency averaged Gaunt factor, and shows value of $1.1 - 1.5$ (Rybicki G. B. & Lightman A. P. 1979). The surface brightness is heavily dependent on the density rather than plasma temperature so that X-ray is suited for observing around center of clusters of galaxies. Considering a system having the volume of 1 Mpc, temperature of 5 keV and density of 10^{-3} cm^{-3}, Eq.(2.18) yields the luminosity of 2×10^{42} erg s^{-1} which is the typical luminosity of clusters of galaxies. Noted that, bremsstrahlung emission coming from space is originated from electrons since the emissivity is proportional to $1/m^2$, and no significant emission from protons is expected.

In the temperature range of clusters of galaxies, thermal bremsstrahlung works to cool the plasma as a dominant emission. The rough time scale of ICM cooling is calculated by dividing energy of plasma, $\frac{3}{2} k_B T\,(n_e + n_p)$, by Eq.(2.18) as below

$$\tau_{cool} \sim 60 \times 10^8 \left(\frac{n_e}{10^{-3}\ \mathrm{cm}^{-3}}\right)^{-1} \left(\frac{k_B T}{5\ \mathrm{keV}}\right)^{-1/2} \quad \text{year}. \tag{2.19}$$

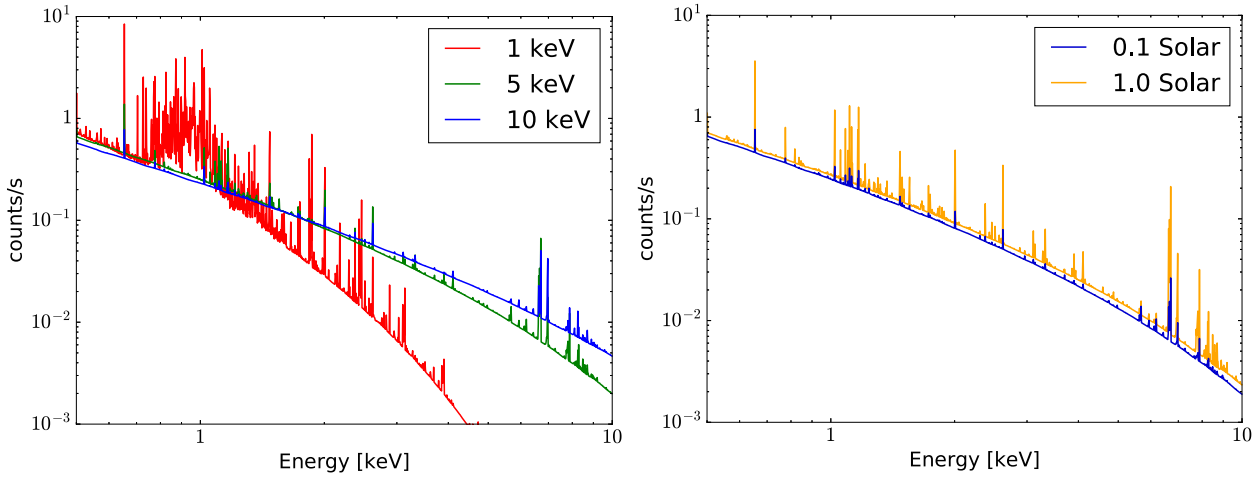

Figure 2.2: ICM spectra produced with apec model in Xspec with an arbitrary detector response. Vertical axis is discretionary. *Left panel*: Spectra having different temperature with fixed metal abundance of 0.3 Solar each. *Right panel*: Different metal abundance spectra with fixed temperature of 5 keV. The reason why 1.0 Solar spectrum has higher intensity slightly than 0.1 Solar one is due to contribution of radiative recombination emission.

Compared to the age of universe $\sim 10^9$ years, the effect of cooling is non-negligible in the center of clusters, causing central cool component in some clusters (e.g. Makishima et al. 2000). On the other hand, it can be ignored within a merger dynamical timescale.

2.2.2 Line emission

Since ICM is optically thin, ions are excited via collisions, and not by photo-excitation. Excitation by collisions is caused by coulomb force and the collision frequency of electrons is much higher than protons in temperature equilibrium so that it mainly happens between electrons and ions. Ions are exited either by a collision directly or through recombination. Due to the small density, ions are almost in the ground state, and collisional de-excitation, additional excitation or ionization are negligible. When the excited higher state transit to lower state, a photon with the energy difference between the states is emitted, and this is called fluorescence line emission. The central energy, intensity, and ratio of line emission flux enable us to diagnostic ionization state, heavy ion (or metal) abundance and temperature as well as density under certain circumstances. For example, Fe Kα emits around 6.4 keV in the ionization state of Fe I–XVII, meanwhile 6.7 or 6.96 keV in Fe XXV/XXVI (He/H-like) state. This is because the effective charge becomes large and electro-static potential becoming deep in high ionization states (e.g. Jacoo Vink 2012).

The line emission from the H-like state, the simplest atomic structure, is expressed as

$$E_n = \frac{m_e Z^2 e^4}{2\hbar^2}\left(\frac{1}{m^2}-\frac{1}{n^2}\right) \quad (m,n=1,2,3,...:m<n) \tag{2.20}$$

$$= 13.6Z^2\left(\frac{1}{m^2}-\frac{1}{n^2}\right)\ [\mathrm{eV}]. \tag{2.21}$$

Here, m and n are lower and higher states where electrons are transited, respectively. Line emission becomes stronger in low temperature, as shown in Fig.2.2. Fe-L line emission becomes outstanding around 1 keV when temperature is less than 2 keV with a typical abundance of 0.3. Oxygen H/He-like ions make strong lines with plasma temperature of 0.5 keV. The emissions surrounding the earth coming from Local hot bubble are notorious for contamination of X-ray astronomy in low energy band, and electro-static potential becoming deep.

2.3 Basic physical parameters in ICM

ICM is almost fully ionized due to the high temperature of 10^{7-8} K. Combined with its low density of 10^{-4}–10^{-2} cm^{-3}, ICM has some particular characteristics. In general, plasma is defied with 5 conditions;

1. It is a medium which contains both plus and minus charged particles,
2. electrically neutral in a large scale,
3. charged particles have random thermalized motion,
4. plasma frequency is higher than collision frequency,
5. and the scale of medium is much larger than debye length.

In this section, we review the plasma feature of ICM by showing the fundamental plasma parameters.

Thermal velocity

Usually, particles within plasma have Maxwell distribution so that thermal velocity is defined from relation between particles velocity and temperature as,

$$\sqrt{\langle v^2\rangle} = \sqrt{\frac{3k_BT}{m}}. \tag{2.22}$$

The value of electrons and protons are $v_{th,e} = 5.1\times10^4$ km s^{-1} and $v_{th,p} = 1.2\times10^3$ km s^{-1} with the typical cluster galaxies's temperature of 5 keV.

Plasma frequency

Plasma consists of protons and electrons in addition to small quantity of heavy ions. Movement of particles breaks neutrality but an electric field emerges and drags electrons in order to sustain the neutrality. Electrons cannot stop at the point establishing neutral because of inertia and make an electric filed again. Then, electrons are dragged-back, and ocscillates. The oscillation frequency is called 'Plasma frequency' found by Irving Langmuir and Lewi Tonks 1920s (e.g. Spitzer 1965), and expressed as,

$$\omega_{pe} = \sqrt{\frac{n_e e^2}{m_e \varepsilon_0}} = 1.8 \times 10^3 \left(\frac{n_e}{10^{-3}\ \mathrm{cm}^{-3}} \right)^{1/2}\ \mathrm{s}^{-1}, \tag{2.23}$$

where n_e, e, m_e and ε_0 are electrons density, charge mass and dielectric constant, respectively. It determines the physical time scale of the plasma. For example, electro-magnetic wave with frequency lower than this value cannot penetrate the plasma. Apparently, ICM plasma stops kHz radio, but not optical or X-ray photons. Although each particle has its own plasma frequency, the lightest particle, electron, is the most important.

Debye length

Considering a situation in which a small size of region is charged within plasma, electrons move to counteract the electric field created from the charge. Thus, the electric potential is diluted as,

$$\phi \sim \frac{1}{r} \mathrm{exp} \left(-\frac{\mathrm{r}}{\lambda_{\mathrm{De}}} \right). \tag{2.24}$$

Here, λ_{De} is the debye length and given as

$$\lambda_{De} = \sqrt{\frac{\varepsilon_0 k_B T_e}{n_e e^2}} = 1.7 \times 10^4 \left(\frac{k_B T}{5\ \mathrm{keV}} \right)^{1/2} \left(\frac{n_e}{10^{-3}\ \mathrm{cm}^{-3}} \right)^{-1/2}\ \mathrm{m}. \tag{2.25}$$

Electrical potential in plasma is reduced in a length of much shorter than in vacuum due to the term of exponential. Debye length is the range where a electric field driven by a charge can extent within a plasma.

Collision frequency

Particles in plasma are colliding each other via coulomb collision. The scattering cross section is

$$\sigma_{1,2} = \frac{q_1^2 q_2^2}{4\pi \varepsilon_0^2 \mu^2 v^4} \ln\Lambda, \tag{2.26}$$

in which q_1, q_2 are charges of colliding particles. Also v and n_{gas} are relative velocity between particles and gas density, respectively, and Λ is $n_{gas}\lambda_{De}^3$, expressing the number of particles within a sphere with a radius of Debey length. The most frequent collision in plasma is between electrons and protons when those temperature is in equilibrium, thus the collisions represent this collision frequency of plasma, $\nu_{e,p}$

$$\begin{aligned}
\nu_{e,p} &= n_{gas}\sigma_{e,p}v_{e,p} = \frac{n_{gas}e^4}{16\pi\varepsilon_0^2 m_e^2 v_{e,p}^3}\ln\Lambda && (2.27)\\
&= \frac{n_{gas}e^4}{48\sqrt{3}\pi\varepsilon_0^2 m_e^2 v_{e,p}^3\sqrt{m_e}}\frac{1}{(k_BT)^{3/2}}\ln\Lambda && (2.28)\\
&= 5.4\times10^{-14}\left(\frac{n_{gas}}{10^{-3}\ \mathrm{cm}^{-3}}\right)\left(\frac{k_BT}{5\ \mathrm{keV}}\right)^{-3./2}\ \mathrm{Hz}. && (2.29)
\end{aligned}$$

Taking the ratio of collision frequency to plasma frequency, $\nu_{e,p}/\omega_{pe} \sim 1/\Lambda$, provides whether particles collisions are negligible. The plasma which satisfies $\nu_{e,p}\omega_{pe} << 1$ called non-collisional (or collison-less) plasma. Λ in ICM is $\sim 10^{15}$, thus the ICM is an ideal non-collisional plasma.

Mean free path

Mean free path is an average distance in which a particle experiences a collision. It is expressed as $l_{mfp} = v_{1,2}/\nu_{1,2}$, thus the mean free path of electrons and protons in the case of coulomb scattering with Maxwell distribution is

$$l_e = l_p = \frac{9}{4\pi}\frac{(k_BT)^2}{n_{gas}\left(\frac{e^2}{4\pi\varepsilon_0}\right)^2\ln\Lambda} = 7.8\left(\frac{k_BT}{7\ \mathrm{keV}}\right)^2\left(\frac{n_{gas}}{10^{-3}\ \mathrm{cm}^{-3}}\right)^{-1}\ \mathrm{kpc}. \quad (2.30)$$

The size is comparable to the radius of galaxies and is much smaller than clusters of galaxies itself, and it justifies the ICM is treated as a fluid.

Sound velocity

Sound velocity is the transmission velocity of compressive waves or information within a medium. In an ideal fluid such as the ICM, sound velocity is expressed as,

$$C_s = \sqrt{\frac{\gamma k_BT}{\mu m_p}}. \quad (2.31)$$

Here, μ and γ are mean molecular weight and ratio of specific heat. μ is about 0.6 within plasma of space. The sound velocity of ICM is about 1150 km s^{-1} with temperature of 5 keV.

Magnetic field

Plasma is always magnetized, and the strength within the ICM have been measured with mainly Rotation Measure. This method utilizes multiple radio sources with linear-polarization. Since the line-of-sight magnetic field within a plasma rotates the polarized angle dependent on the frequency, it can be measured by observing radio polarization in a few frequencies. Because the magnetic field is considered to be in random form, its typical length is needed to be estimated to relate it with the Rotation Measure. Also, plasma density is needed (e.g. Clarke 2004). The observations revealed the magnetic field of the ICM is a few μG. The magnetic field waves also transmit information as well as compressive waves. The velocity called "Alfven" velocity and is expressed as,

$$v_A = \sqrt{\frac{B^2}{\mu_0 \rho_{gas}}} = 90 \text{ km} \left(\frac{B}{1\ \mu\text{G}}\right)^{1/2} \left(\frac{n_{gas}}{10^{-3}\ \text{cm}^{-3}}\right)^{-1/2}, \tag{2.32}$$

where B and ρ_{gas} are strength of magnetic field and mass density of gas, respectively. The ratio of $v_A/C_s < 1$ indicates that the magnetic filed is ignorable in the ICM when we consider the dynamical reaction of the ICM.

In contrast to the preceding argument, it has a important role in small scale structures. The magnetic field bents the trajectories of charged particles in normal to the field. The gyro radius of a thermal electron is represented as,

$$r_g = \frac{\sqrt{3mk_BT}}{|q|B} = 10^{-14} \text{ kpc} \left(\frac{k_BT}{5\ \text{keV}}\right)^{1/2} \left(\frac{B}{1\ \mu\text{G}}\right)^{-1} \tag{2.33}$$

The size is much smaller than Coulomb mean free path, even though the magnetic field strength is very small. Therefore, it suppresses the diffusion and decrease thermal conductivity dramatically along the direction of normal to the magnetic field.

2.4 Shocks

Shocks are induced when an object moves within a medium faster than the sound velocity. On the ground, shocks are activated via collisions of particles. In the space, the medium is often ionized, and hence is a plasma because of low density and high temperature. In such a condition, shocks are not activated via collisions, but electromagnetic interaction within plasma. It is called "collision-less" shock. The feature is the extremely short transition layer compared to Coulomb collision mean-free-path.

The phenomena have been observed in variety of places such as interplanetary plasma, supernova remnants, and active galactic nuclei and others. Merging clusters of galaxies are one of the objects in which shocks are often seen. The peculiar characteristic of shocks within clusters of galaxies is the low Mach number of $1-5$. This is because the temperature

of the pre-merger clusters' ICM has already reached individual clusters' Virial temperature, and the colliding velocity cannot largely exceed the sound velocity.

2.4.1 Rankine-Hugoniot relations

The pre- and post-shock regions parameters are connected with Rankine-Hugoniot relations. The relation is derived from the three conditions of fluid equation. (1) conservation of mass, (2) conservation of momentum, and (3) conservation of energy. Here, we consider one dimension for simplicity. Those conditions are expressed as,

$$\rho_1 v_{x1} = \rho_2 v_{x2}, \tag{2.34}$$

$$P_1 + \rho_1 v_{x1}^2 = P_2 + \rho_2 v_{x2}^2, \tag{2.35}$$

$$\left[\rho_1 v_{x1}\left(\frac{1}{2}v_{x1}^2 + \frac{\gamma}{\gamma-1}\frac{P_1}{\rho_1}\right)\right] = \left[\rho_2 v_{x2}\left(\frac{1}{2}v_{x2}^2 + \frac{\gamma}{\gamma-1}\frac{P_2}{\rho_2}\right)\right], \tag{2.36}$$

where ρ is mass density. The subscripts 1 and 2 represent pre- and post-regions. We ignored magnetic field for simplicity. Combining these equations provides,

$$\frac{\rho_2}{\rho_1} = \frac{4M^2}{M^2+3}, \tag{2.37}$$

$$\frac{P_2}{P_1} = \frac{5M^2-1}{4}, \tag{2.38}$$

$$\frac{T_2}{T_1} = \frac{5M^4+14M^2-3}{16M^2}. \tag{2.39}$$

Here, we assumed single atom ideal gas so that $\gamma = 5/3$. It indicates that the pressure and temperature of post-shock region become larger as the Mach number gets larger. Meanwhile, the density of post-shock region has limitation, i.e . less than 4, within the single atom ideal gas at $M \gg 1$. Fig.2.3 shows the three Rankine-Hugoniot relations as a function of Mach number.

2.4.2 Entropy

Shocks transform a part of the kinetic energy of its motion of the pre-shock region into thermal heat. Therefore, the post-shock region has higher entropy than the pre-shock region. The entropy is expressed as,

$$S = C_v \ln\frac{P}{\rho^\gamma} + const. \tag{2.40}$$

The difference of entropy between the pre- and post-shock regions is,

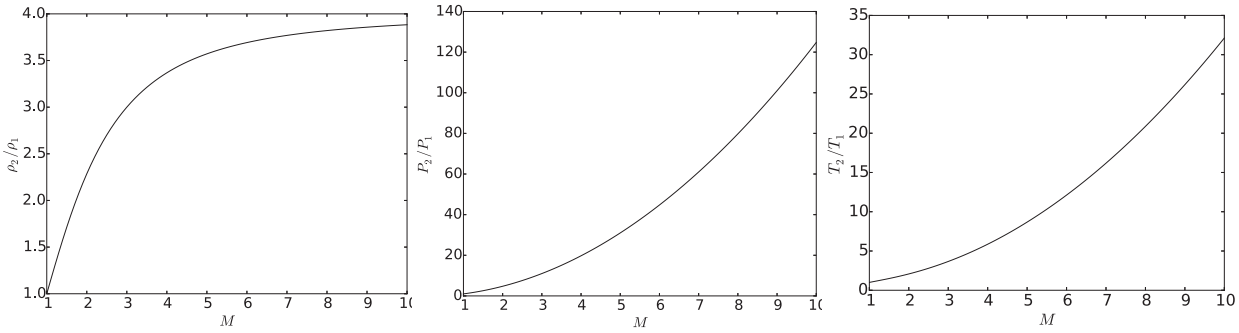

Figure 2.3: The Rankine-Hugonio relations of density (left), pressure (middle), and temperature (right).

$$S_2 - S_1 = C_v \ln \left[\frac{P_2}{P_1} \left(\frac{\rho_1}{\rho_2} \right)^{\gamma} \right]. \tag{2.41}$$

Inserting Rankine-Hugoniot relations into the Eq.(2.41) gives,

$$S_2 - S_1 = C_v \ln \left\{ \left[1 + \frac{2\gamma}{\gamma+1} \left(M^2 - 1 \right) \right] \left[\frac{(\gamma-1) M^2 + 2}{(\gamma+1) M^2} \right]^{\gamma} \right\}. \tag{2.42}$$

M has to be larger than 1 so that $S_2 - S_1 \geq 0$. Therefore, shocks increase the entropy of post-shock region.

Entropy is defined as $s = \frac{3}{2} k_B \ln \left(\frac{k_B T_e}{\rho^{2/3}} \right)$ for an ideal gas. The contents of logarithmic, $K = \frac{k_B T}{(n_e)^{2/3}}$, is referred as "entropy" (or astrophysical entropy) in astrophysics conventionally. Note that if there is no shock but just compression, i.e. the bulk motion is sub-sonic, entropy will be unchanged.

2.5 Cold fronts

The first discoveries of cold fronts are in Abell 2142 and Abell 3667 by Chandra observations (Markevitch et al. 2000, Vikhlinin et al. 2001). Before the launch of Chandra, ROSAT PSPC found a surface brightness transition in the Abell 3667. The energy band of PSPC is, however, narrow and cannot measure the ICM temperature in detail, and thus the structure was interpreted as a shock. Chandra provided a much better resolution image and temperature distribution at the discontinuity. It showed the acquired results are different from what was expected from a shock structure. At the structure, the density expresses an increase but the temperature decreases largely. If this brightness jump were a shock, both temperature and density show increase from pre- to post-region at the shock discontinuity.

This structure is named "cold fronts" from the feature and have been found in dozens of systems to date. Surprisingly, it has been revealed that the phenomenon is more ubiquitous

than shocks in cluster merger. Fig.2.4 shows a toy model explaining how the cold fronts are configured. Ram pressure becomes larger along with increase of colliding velocity in the cluster merger. It strips surrounding gases of clusters' cores having low density reflecting gravitational potential. Then, large density discontinuity is constructed after the removing of the ambient gases.

At cold fronts, density is increased, temperature is decreased, pressure is almost identical (when ram pressure is small) and entropy is declined dramatically. This marks the big difference to a shock, in which gas entropy "increases" in the post-shock region, in other words, in a region with higher density.

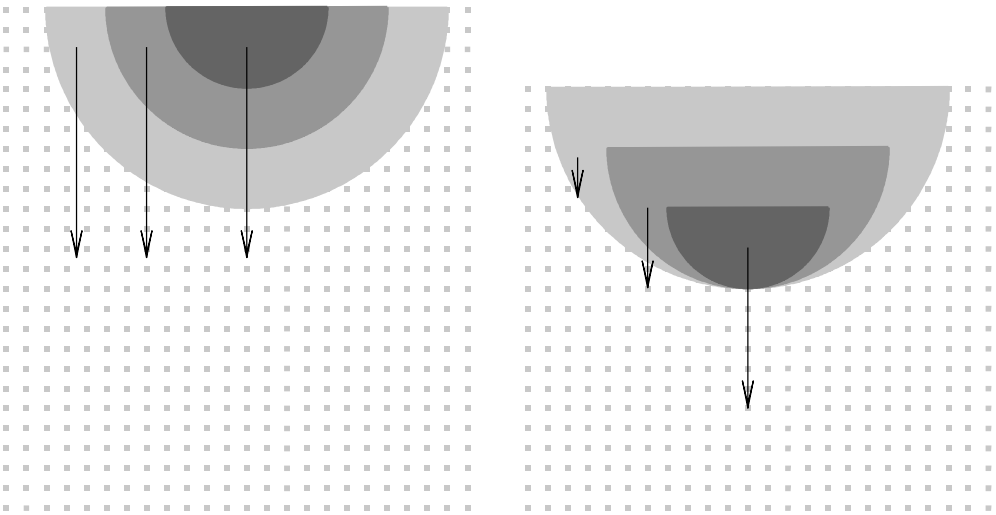

Figure 2.4: The formation process of cold fronts in the event of cluster mergers which originates from Markevitch and Vikhlinin 2007.

Chapter 3

Instruments

The universe is invisible from the ground in X-ray, because atmosphere is optically thick in the energy band. Therefore, the development of rocket to go to space was necessary for the beginning of X-ray astronomy. The start of X-ray observation is the solar observation with a Germany rocket, which was performed by USA in 1948. It discovered that the solar spectrum is extended, surprisingly, from ultraviolet to X-ray. Since then, several tens of X-ray observation instruments have been launched to space ceaselessly. In this thesis, major three X-ray satellites, Suzaku, Chandra and XMM-Newton from Japan, USA and ESA, respectively, were utilized. The capability of those satellites are summarized in this chapter.

3.1 Suzaku

Suzaku (Mitsuda et al. 2007) was lunched in July 10, 2005 as the fifth X-ray satellite of Japan. The full length and amount of mass are 6.5 m and 1680 kg, respectively. Suzaku orbited around the earth in 96 minutes with an inclination of 32 degree and an altitude of 570 km. The diagrammatic illustration and arrangement of detectors are shown in Fig.5.1. Four X-ray charge-coupled devices (CCD), the X-ray Imaging Spectrometer (XIS), and a micro calorimeter, the X-ray Spectrometer (XRS), were onboard in the focal plane of 5 X-ray telescopes, the X-ray telescopes (XRT), each. The XIS and XRS were designed to provide imaging X-ray spectroscopy in the 0.3–12 keV band. Non-imaging hard X-ray Detector (HXD) observing the same direction of these X-ray instruments and covering 10–600 keV is also equipped. Unfortunately, the XRS lost its function without any observations due to an accidental leak of liquid helium soon after the launch. The combination of XIS and HXD instruments provides wide energy band observations of 0.3–600 keV. The observatory operation was ended in August 26, 2015 because of battery depletion.

Suzaku achieved a variety of science results from blackhole to clusters of galaxies, and the peer-reviewed papers of more than 750 had been published [1]. The most prominent feature is the low and stable background. This is because instruments are protected from cosmic rays

[1] see, http://www.astro.isas.jaxa.jp/suzaku/bibliography/journals/index.html.ja

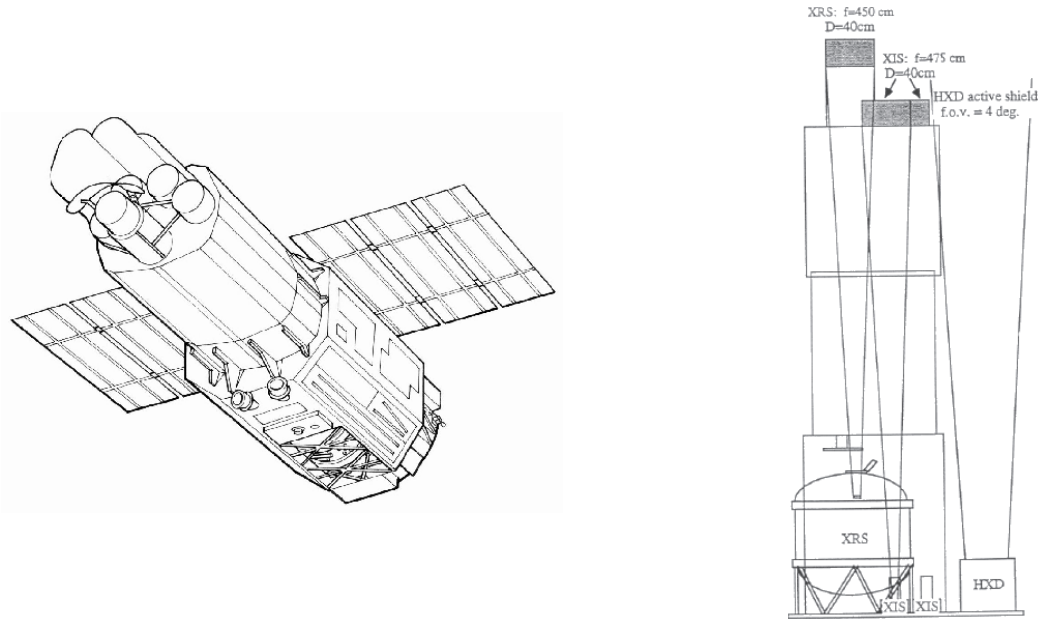

Figure 3.1: *Left panel*: Suzaku whole schematic image. *Right panel*: The cross sectional view of Suzaku. Both of which originate from Pottschmidt et al. (2015).

coming from the Sun or deep space by magnetic field of the earth. Instruments, however, have to stop observations at South Atlantic Anomaly in which charged particles belt exist or when a target is hided behind the earth due to the low altitude, and thus observations efficiency is reduced to 50%.

3.1.1 XRT; the X-ray Telescope

In the X-ray band, a refractive index is slightly just smaller than 1 in metals. The XRT was designed to use total reflection by making an incidence angle of less than 1 degree. It utilizes Walter-I optics design and made of 175 nested reflectors. The reflectors are made from 152 μm thick aluminum coated with gold by replica method (P. J. Serlemitsos et al. 2006). This technology is characterized with light weight, low cost and large effective area. Meanwhile the angular resolution of the reflectors is limited due to distortions in the thin aluminum foils.

Point spread function (PSF) expresses a spread of a point source focused by the instruments response. In Fig.3.2 left, the encircled energy function (EEF), which integrated the PSF and represents the number of photons accumulated within a radius, is shown. A standard indicator of expressing the performance of an angular resolution is half power diameter (HPD) in which half of focused X-ray is enclosed. The HPD of XRT is $1'.8$ to $2'.3$ in the energy band of 0.2-12 keV.

A higher energy photon has smaller refraction angle so that the critical angle of total reflection is close to 0. Therefore, nested reflectors located outer sides cannot reflect a high energy photon and effective area in the band becomes small. The effective area of XRT is

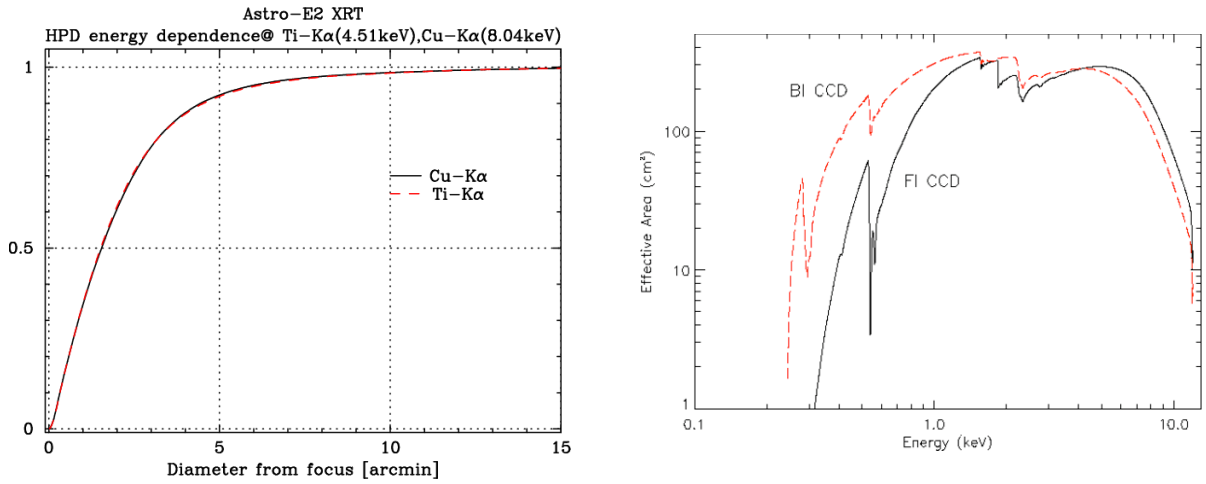

Figure 3.2: *Left panel*: PSF of XRT shown as encircled energy function. *Right panel*: The XIS+XRT on-axis total net effective area, and red and black lines are for BI and FI CCDs, respectively. Both of which originate from Pottschmidt et al. 2015.

440 and 250 cm^2 at 1.5 and 8.0 keV, respectively, and the net effective area of combination with front illuminated (FI) and back illuminated (BI) CCD's quantum efficiency is shown in Fig.3.2 right. FI and BI CCDs are described in Sec.3.1.2.

3.1.2 XIS; X-ray Imaging Spectrometer

Suzaku is installed with 4 XIS, which are CCD cameras recording the position and energy of individual X-ray photons. Each CCD chip has 1024×1024 pixels, with a pixel size of $24\ \mu m = 1''.04$, and a field of view of $17'.8 \times 17'.8$. XIS0, XIS2, XIS3 are FI chips, and

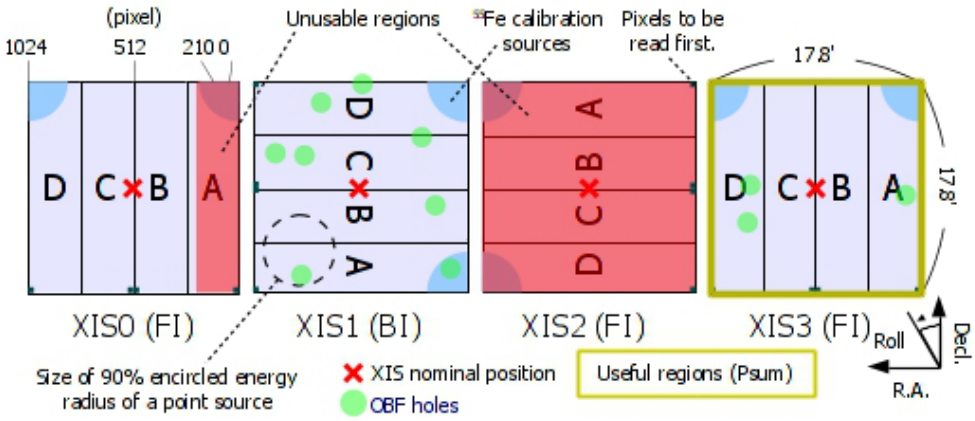

Figure 3.3: The arrangement of XIS CCDs. Each CCD consists of four segments A, B , C and D. The region colored with red is unusable as of 2009 June. It was taken from Pottschmidt et al. (2015).

the other (XIS1) is BI chip. FI CCD has better quantum efficiency of the higher energy because of thicker depletion layer. The thickness are ~ 65 μm and ~ 42 μm for FI and BI, respectively (K. Koyama et al. 2006). On the other hand, BI CCD has higher efficiency below 1 keV, because the CCD electrodes are located at the backside and hence not absorbing soft X-rays. The entire chip of XIS2 and a part of XIS0 were lost because of micro-meteorite hits in 2005 November and 2009 June, respectively, as shown in Fig.3.3. Each XIS carries two calibration sources of ^{55}Fe on two corners. The source emits Mn-Kα and Mn-Kβ lines while decaying at 5.9 and 6.5 keV, respectively. The energy resolution of each XIS chip had been monitored using the 5.9 keV line. It is defined with full width at half maximum (FWHM), and had got worse as time passes owing to damage by cosmic rays. The energy resolution of XIS chips are around 150–200 keV (FWHM).

3.2 XMM-Newton

XMM-Newton was launched on December 10, 1999 by ESA as the second cornerstone mission of ESA's Horizon 2000 programme. The full length and amount of mass reach 10.8 m and 3800 kg, respectively. The appearance diagram is shown in Fig.3.4. XMM expresses "X-ray multi mirror", and three X-ray telescopes and one optical/UV telescope are onboard as the name indicates. The well balanced designs of X-ray telescopes provide a good angular resolution and a large effective simultaneously.

Three CCD units, European Photo Imaging Camera EPIC, MOS1, MOS2, and PN. Two telescopes coupled with EPIC MOS 1 and 2 has a reflection grating plate below the mirror.

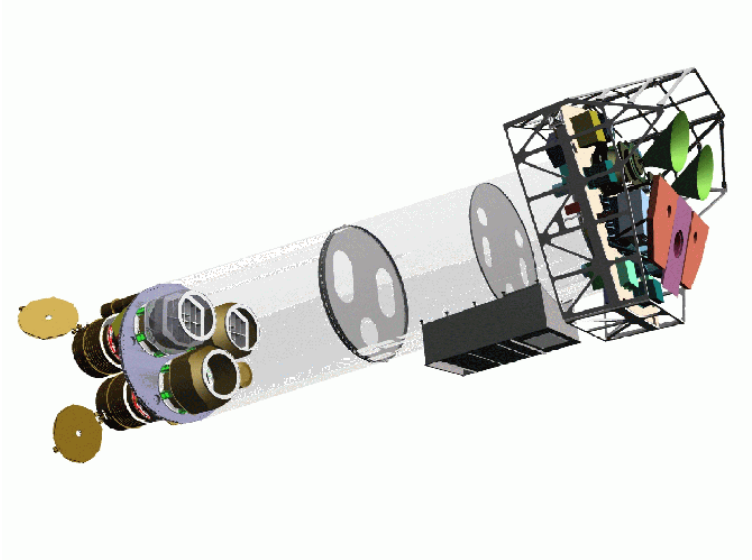

Figure 3.4: XMM-Newton diagram illustration taken from XMM-Newton Community Support Team with contributions from the entire XMM-Newton Science Operations Centre Team 2017.

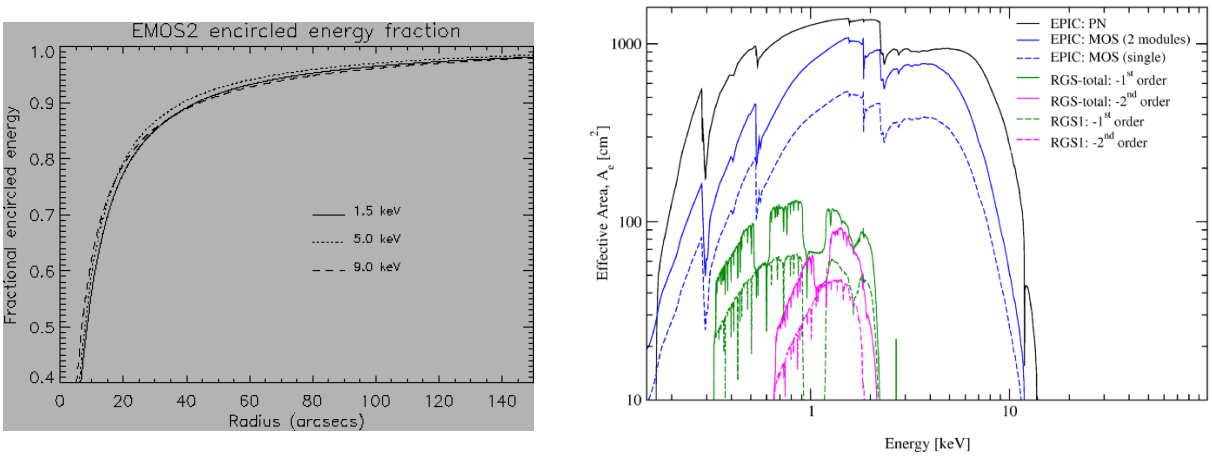

Figure 3.5: *Left panel*: The PSF of X-ray telescope of EPIC MOS2. *Right panel*: On-axis total net effective area of all XMM-Newton X-ray telescopes of EPIC and RGS. Both of which originates from XMM-Newton Community Support Team with contributions from the entire XMM-Newton Science Operations Centre Team 2017.

It is designed to transmit 50 % of X-ray photons to the MOS camera, while reflection 40 % of them into the CCD arrays for fine-resolution-dispersive spectrometer, named RGS. Although RGS has a high resolution spectroscopic power in energy 0.2–0.8 keV, it cannot be applied to diffuse sources such as SNR and clusters of galaxies except for particular bright small regions as it uses a grating system without any slit. The combination of those instruments and Optical Monitor, which works in optical and UV band, makes first simultaneous X-ray and optical/UV observations possible.

3.2.1 X-ray telescopes

Each telescope onboard XMM-Newton consists of 58 nested mirrors. These mirrors are constructed by coating with gold by vapour-depositing to a polished mandrel. Nickel support layer is produced by electroforming onto gold layer. Mirrors are taken off from the mandrel by cooling to shrink the mandrels. Telescopes have a good angular resolution because of thick gold layer, though with relatively large weight.

The on-axis PSF of MOS2 telescope in energies of 1.5, 5.0, 9.0 keV is shown in Fig.3.5 left. Each telescope has almost identical PSF, and the HPD at 1.5 keV are about 15″ (B. Aschenbach et al. 2002). The net effective area of each telescope including the CCD efficiency (Sec.3.2.2) is shown in Fig.3.5 right. It reaches more than 2000 cm^2 in total at 1.5 keV.

3.2.2 EPIC; European Photon Imaging Camera

MOS and PN cameras (Turner et al. 2001, Struder et al. 2001) consist of 7 and 12 CCD chips as indicated in Fig.3.6, respectively. MOS1,2 are front-illuminated CCDs. MOS CCD

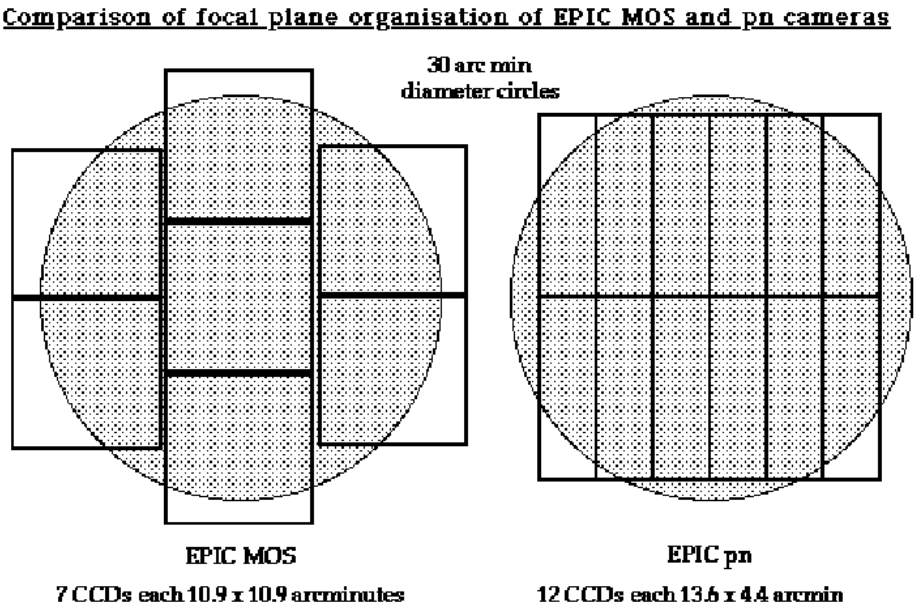

Figure 3.6: The schematic diagram of EPIC MOS and pn, both of which are taken from XMM-Newton Community Support Team with contributions from the entire XMM-Newton Science Operations Centre Team 2017.

chips has 600×600 pixels, and the size of a pixel is $1''.1$. On the other hand, PN is back illuminated CCD. The CCD chips consist of 64×189 pixels with the pixel size of $4''.1$.

EPIC camera has a famous limitation caused by soft protons having energy of a few hundreds keV, which generates strong background signals all over the detectors and effectively hampers the observation. It is caused by the XMM-Newton's long elliptical orbit in which the major and minor axis are 7000 and 114000 km, respectively. Soft protons are considered originating from clouds populating the Earth's magneto-sphere. Thus, the intensity of soft proton depends on factors such as the position of XMM-Newton with respect to the clouds and the altitude as well as solar activity. Protons are reflected and focused by telescopes and generate signals on the CCDs. Therefore, such events are emerged as the background.

Analysis of diffuse sources is strongly affected by soft protons more than point sources. Removing such a background correctly has an impact to the results, and thus its handling method is important.

3.3 Chandra

Chandra is one of NASA's four Great Observatories, and launched by NASA's Space Shuttle Columbia on July 1999. It is indeed a large satellite, and the full length and the mass are 19.5 m and 4790 kg, respectively.

An X-ray telescope, the High Resolution Mirror Assembly (HRMA), having the highest angular resolution in the X-ray band so far is onboard. Two CCDs, ACIS-S and ACIS-I,

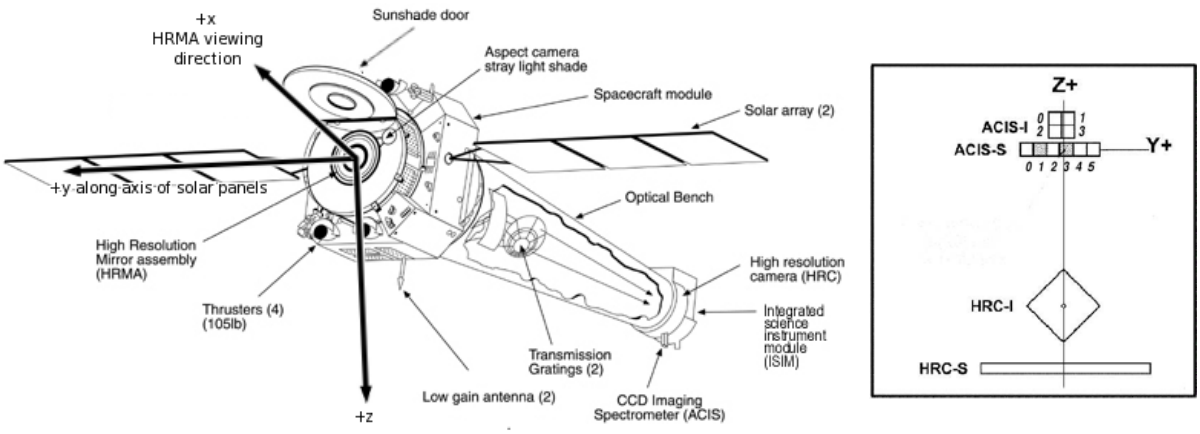

Figure 3.7: *Left panel*: The schematic view of Chandra X-ray observatory. *Right panel*: The arrangement of detectors of Chandra. Both of which are taken from Chandra IPI Teams 2016.

and a microchannel plate instrument comprised of two detectors, High Resolution Camera (HRC), are equipped as focal plane detectors. CCDs and HRC are able to function as a simultaneous imager and spectrometer. Although, HRC has larger an observation filed of view and higher an angular resolution, the spectroscopic power is lower than CCDs. Thus, the combination and HRMA and CCDs are utilized in this thesis.

Two grating systems named the Low Energy Transmission Grating (LETG) and High Energy Transmission Grating (HETG) slide into the focus of the mirror, when needed. They cover energy band of 0.08–0.2 keV and 0.4-10.0 keV, respectively, with the high spectral resolution power. General view and detectors arrangement of Chandra are shown Fig.3.7.

3.3.1 HRMA; High Resolution Mirror Assembly

HRMA comprised of 4 nested mirrors coated with iridium on a binding layer of chromium. The Chandra's great resolution is archived owing to the precise optical surface of glass mirror substrate polished directly with an excellent technique.

The on-axis PSF of HRMA is expressed as EEF with an angular radius at several energies in Fig.3.8 left. The HPD is smaller than 0".5 even at the highest energy of 9.7 keV. The PSF becomes worse towards off-axis regions but still less than 30″ at high energy X-ray of 6.4 keV at radius of 15', which is the almost edge of Chandra FOV. The effective area of HRMA is 400 and 100 cm^2 at energy of 5.0 and 8.0 keV, respectively, as shown in Fig.3.8 right.

3.3.2 ACIS; Advanced CCD Imaging Spectrometer

ACIS is arranged of AICS-I and ACIS-S, with 2×2 and 1×6 array chips, respectively. Each chip has 1024×1024 pixels, and the size of a pixel is 0″.492. Two of the CCDs in

ACIS-S are BI and the others are FI, and 6 chips are usually able to be on an observation simultaneously. The arrangement illustration of ACIS is shown in Fig.3.9.

ACIS FI CCDs had the energy resolution of almost theoretical limit as a Si detector before the launch. The energy resolution is, however, degraded seriously after the launch during Chandra passed radiation belt because of the scattering of low energy protons at CCD

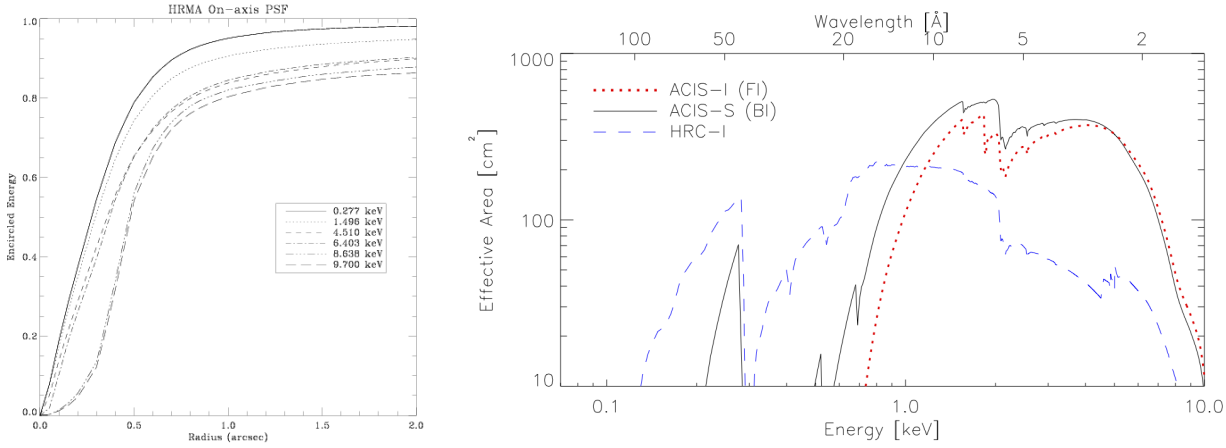

Figure 3.8: *Left panel*: The PSF of HRMA for different energy X-rays. *Right panel*: On-axis total net effective area of ACIS-I, ACIS-S and HRC-I. Both of which originate from Chandra IPI Teams 2016.

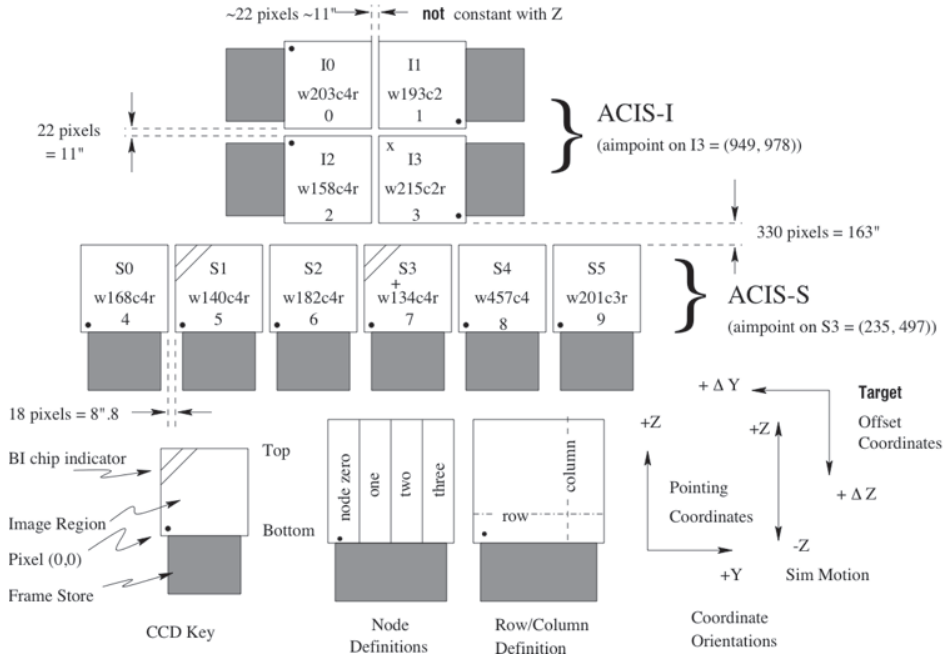

Figure 3.9: The schematic diagram of Advanced CCD Imaging Spectrometer, ACIS-I and ACIS-S, originates from Chandra IPI Teams 2016.

through HRMA. Moving ACIS to a sheltered position was operated soon after the event was noticed, and no further degradation has happened since then. Correction algorithm developed by the ACIS instrument team was applied to the FI CCDs at all energies and which dramatically improved the CTI-induced loss of energy resolution. Although the effect is more minor, the same way also recovers BI CCDs.

3.4 Comparison of capabilities

Comparison of effective area and background count rate between Suzaku, Chandra and XMM-Newton are shown in Fig.3.10. Performance parameters are also summarized in Table.3.1. Suzaku is the best satellite to observe faint outermost region of clusters of galaxies because of the low and stable background as well as decent effective area as shown in the right panel of Fig.3.10. Chandra is the most desirable to investigate the structure of clusters of galaxies around their center due to its supreme angular resolution, but it is not suitable for faint outskirts observation. XMM-Newton is good to observe the overall ICM distribution, since it is able to both find structures and inspect outside regions thanks to its good angular resolution and the large effective area. On the other hand, its background is significantly higher than that of Suzaku, limiting the sensitivity for dim regions. Also, the EPIC calibration is known to have some uncertainty. For example, Schellenberger et al. (2014) found systematic differences between Chandra and XMM-Newton, and the later one gives 23% lower temperature than the former on average, at a cluster temperature of 10 keV. Furthermore, MOS and PN also often show different temperature, and PN detector

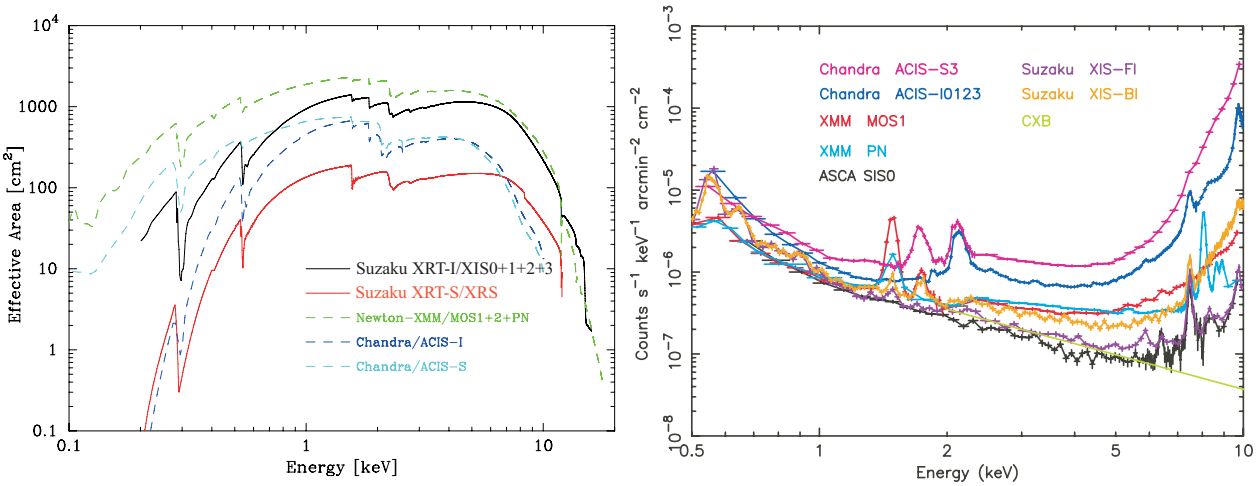

Figure 3.10: *Left panel*: Comparison of effective area between Suzaku, Chandra, and XMM-Newton taken from PJ Serlemitsos et al. (2007). It is not pure telescope effective but quantum efficiency of the CCD, and transmissions of the thermal shield and the optical blocking filter are included. *Right panel*: Comparison of background counting rate as a function of energy taken from Mitsuda et al. (2007).

typically gives the lowest temperatures.

Table 3.1: Performance parameter table of Suzaku, Chandra, and XMM-Newton

Parameter	Suzaku	XMM-Newton	Chandra
Effective area (7 keV)	1250 cm^2	2500 cm^2	800 cm^2
Angular resolution [HPD]	$190''$	$15''$	$< 1''$
Energy resolution [FWHM]	130 eV (6 keV)	140 eV (6 keV)	130 eV (6 keV)
Field of View	$17'.8 \times 17'.8$	$30'$ diamter	$16'.6 \times 16'.6$ (ACIS-I) $8'.3 \times 50'.6$ (ACIS-S)
Launch date	2005	1999	1999

3.5 X-ray Backgrounds

For X-ray data analysis, background signals detected on the detectors must be properly handled especially when analyzing diffuse X-ray sources such as clusters of galaxies. Background signals are roughly divided into two, which originate from celestial X-rays and in-orbit environmental cosmic rays. The latter is called non-X-ray background (NXB). The NXB is generated from the cosmic-rays interaction with detector itself and its housing, and composed of bremsstrhalung emission, fluorescence lines, secondary electrons as well as nuclear radiations from activation of detector materials, neutrons and gamma-rays from Earth albedo. Therefore, it depends on orbit conditions such as terrestrial magnetism. The radiation (or cosmic-ray) environment is not always stable, especially out side of the Earth's magnetosphere. The cosmic-ray flux there is also high. This is the reason why the NXB of Chandra and XMM-Newton is unstable and high. In comparison, Suzaku CCD's NXB is relatively stable. It shows modest variability following the geomagnetic cut-off rigidity, but it can be estimated with accuracy as good as 3–5% referring to these environmental parameters. On the other hand, NXB of Chandra and XMM-Newton must be estimated base on its own data, by referring to the edge of the image, or highest end of the energy band, in which the celestial X-ray emission is relatively weak.

The X-ray background consists of mainly 4 components. Local hot bubble (LHB), Solar wind charge exchange (SWXB), Mikey way halo (MWH) and Cosmic X-ray background (CXB). The details are described below.

ROSAT observation at 1/4 keV (called R12) revealed the existence of weak absorbed soft X-ray emission from the whole sky (Juda et al. 1991, Snowden et al. 1997). The result indicates the earth is located within dilute hot plasma. It is proposed that the gas was heated via a nearby supernova explosion of the earth five to ten million years ago.

SWXB also generates soft X-ray emission (Cravens 2000). Charge exchange emission is created when highly ionized ions in solar wind interact with neutral medium around the

earth. The ion strips an electron from the neutral medium into high energy state. Then, the electron cascades to lower energy states and makes emissions, predominantly line emissions. The intensity is related to solar activity and thus time variable. Local hot bubble and SWXB create similar X-ray emission so that both components are supposed to be expressed with one plasma model simultaneously of temperature of 0.1 keV with solar abundance. In practice, it is modeling the Oxygen line background emission, dominant in the lower energy band of the X-ray data of all 3 observatories used in this thesis.

It has been known that galaxies are surrounded by a dilute and hot plasma gas, and Milky way is also no exception, that is called MWH. The plasma temperature of 0.3 keV corresponds to bounding gravity potential of Milky way. The abundance of solar abundance is also suggested.

CXB has uniform brightness distribution over the whole sky at the X-ray band. The spectrum is represented with a power low model having a photon-index of 1.4. Chandra revealed the emission can be described as a sum of numerous AGN emission through resolving more than 90 % of it into point sources. From its origin, CXB can have a fluctuation depending on the sky region, which can be modeled using the flux distribution of the AGNs observed to date.

3.6 Spectra analysis method in X-ray observatory data

The emission coming from celestial objects is reflected and focused by the X-ray mirror optics. Then, it reaches the detector and interacts via photoabsorption or Compton scattering. In former case, the whole energy is absorbed. Meanwhile only a part of the energy is deposited within the detector in the latter case. The detector has its own energy resolution and it changes the original spectra shape. Consequently, the obtained spectra is different from the initial emission, and those effects are able to be represented with a matrix as a function of input photons energy vs output ADC channels (sometimes called detector response matrix, RMF or RSP). In X-ray astronomy, spectral fitting is executed by multiplying the matrix to the model instead of deriving original spectra, since the matrix does not necessarily have the inverse matrix. This method is called forward fitting. All these issues are handled by the software, XSPEC, provided by NASA. It is made of fitting routine, as well as many spectral models to be compared with the actual data. For example, typical model of ICM emission is made of a thermal emission named *apec*, multiplied with a galactic absorption model *wabs*. Apec (astrophysics plasma emission code) model represents a spectrum from optical thin and collisionally-ionized diffuse gas. ATOMDB code of version 3.0.8 with the chemical abundance table determined by Lodders et al. (2009) is utilized to calculate the intensity of line emissions from heavy elements.

Chapter 4

Research objectives

4.1 Early cluster mergers

Cluster mergers have been investigated with multi-wavelength observations and numerical simulations so as to investigate the physical properties of clusters itself and evolution of large scale structures of the universe or physics of plasma. Although a half of systems show indications of merging, many of them are in their late phase, in which the two cluster cores have already crossed each other.

Late merger is a complex target due to gas mixing and its shock, although clearly seen in many cases, is not bright enough to perform detailed analysis. Here, we summarize the difference of early-phase and later-phase merger clusters in detail. For simplicity, merging of two clusters with almost similar mass, colliding face-to-face is shown as an example. These types of geometry is called "major merger".

First of all, complexity of the later-phase merger makes it difficult to estimate the initial geometry, or the initial energy input itself. In addition, shocks in the ICM generated by

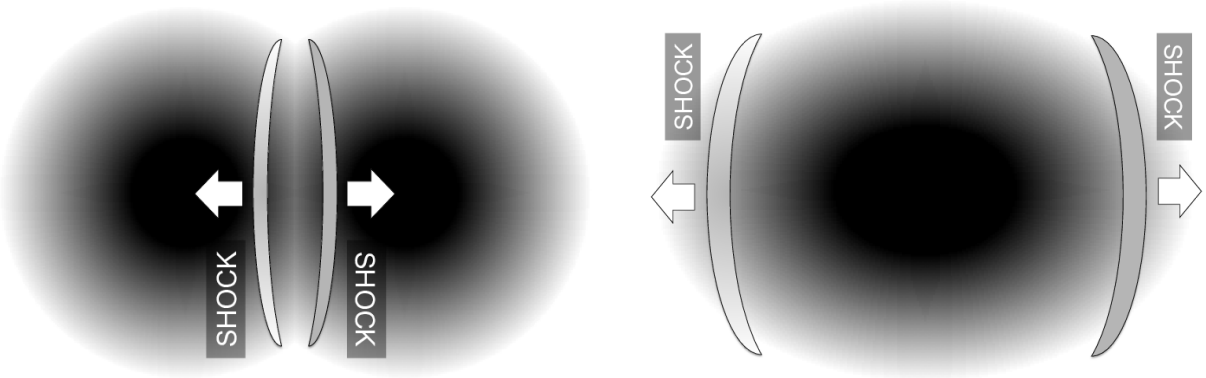

Figure 4.1: *Left panel*: A schematic view of an early stage cluster merger. *Right panel*: A late stage cluster example. In late phase, plasma gases are stirred strongly so that determining the collision geometry is uneasy.

merging have already reached the periphery of the cluster. There, the ICM density is low and its X-ray surface luminosity is dim, which make it difficult to measure the shock structure, as illustrated in the right panel of figure Fig.4.1.

Fig.4.1 left, on the other hand, shows an illustration of early-stage cluster merger. Here, the definition is a system in which cores of the two clusters have not crossed each other. Only about 5 early-stage merger clusters are known to date in the near-by universe (say $z < 0.2$); the Cygnus A cluster, Abell 222–223 pair, Abell 399–401 pair, and 1E2216.0-0401/1E2215.7-0404 pair (Werner, N. et al. 2008, Sakelliou, I. & Ponman, T. J. 2004, Akamatsu et al. 2016). In these systems, the two cluster cores are yet to cross each other, and there is a possibility to have a shock formed in-between the two cluster cores, in which region the ICM density can be high, and its X-ray can be bright.

Such bright shocks would provide rich information regarding collision-less shocks, which have been seen in a variety of places in space such as interplanetary plasma, active galactic nuclei, supernova remnants and so on, with a diversity of shock physical parameters.

As described above, observations of an early-phase cluster merger with shocks have significant impact in understanding the cluster merger itself, as well as the plasma physics. In this thesis, observational results of CIZA J1358.9-4750 (hereafter, CIZA J1359) are described. It is an early stage clusters merger, near-by, and shows bright shock structure in-between the two cores (as shown in Kato el al. 2015 and in this thesis).

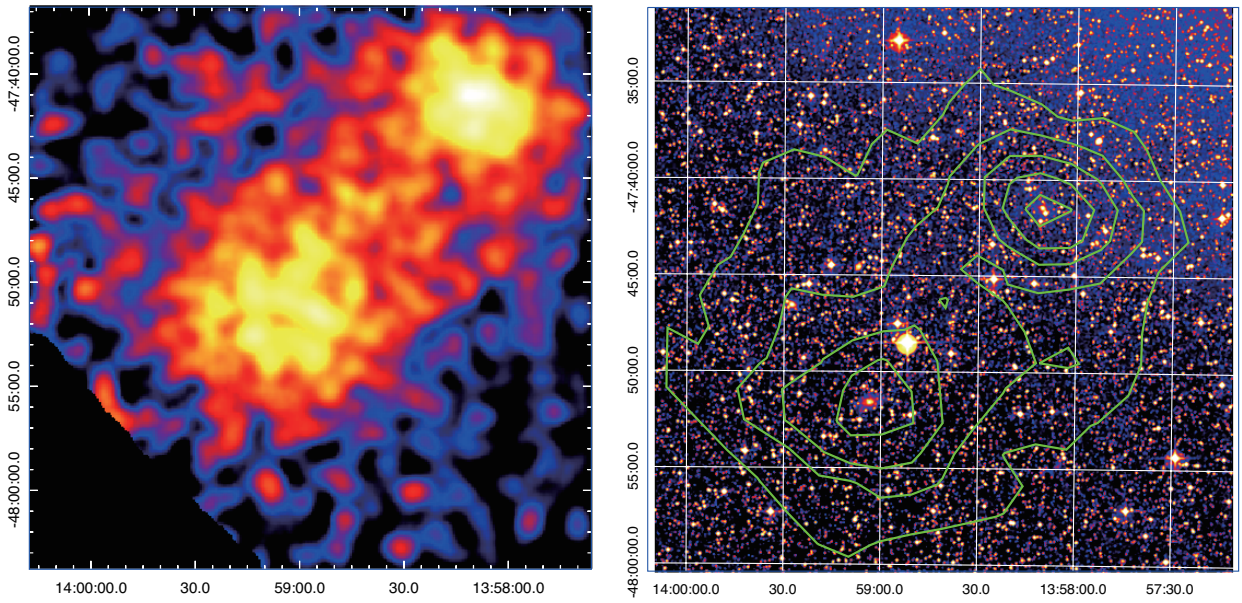

Figure 4.2: *Left panel*: An X-ray image of CIZA J1359 with ROSAT PSPC pointing observation. The energy band is 0.1-2.4 keV. *Right panel*: An optical image of CIZA J1359 with Digital Sky survey. The X-ray contour of ROSAT observation is superposed.

4.2 Overview of CIZA J1358.9-4750

CIZA J1359 is collected in the CIZA (Clusters in the Zone of Avoidance) catalog, which assembles the candidates of clusters of galaxies located at a region with galactic latitude of $|b| < 20^\circ$ (Ebeling et al. 2002, Kocevski et al. 2007). The severe optical extinction and stellar overlap in the direction of Milky Way have made it difficult to identify clusters of galaxies in the optical band. Thus, the coverage of Abell catalog (Sec.2.1.1) had a hole in the region. In the CIZA catalog, candidates are extracted from ROSAT Bright Source Catalogue located within $|b| < 20^\circ$, because the extinction becomes weak in the X-ray energy band. Those objects were checked with the optical band image whether those are clusters of galaxies, and then 250 objects were collected.

CIZA J1359 is the sixth brightest X-ray objects in the list after excluding sources presumably point sources. In Fig.4.2, an X-ray image with ROSAT and an optical image with Digital Sky Survey of CIZA J1359 are shown. The X-ray image is selendipitously detected right at the edge of ROSAT PSPC field of view, when observing another point source. There are a pair of large bright and diffuse X-ray sources located south-east and north-west, and the intermediate region looks bright. The morphology seems like a bridge built across two clusters of galaxies possibly indicating interaction of the two clusters. In the optical image, a bright elliptical galaxies are located at the center of both cluster's cores. The redshift of the elliptical galaxies located south-east and north-wert cores are 0.745 and 0.709, respectively. The close redshift also indicates that those clusters are not merely superposed in the line

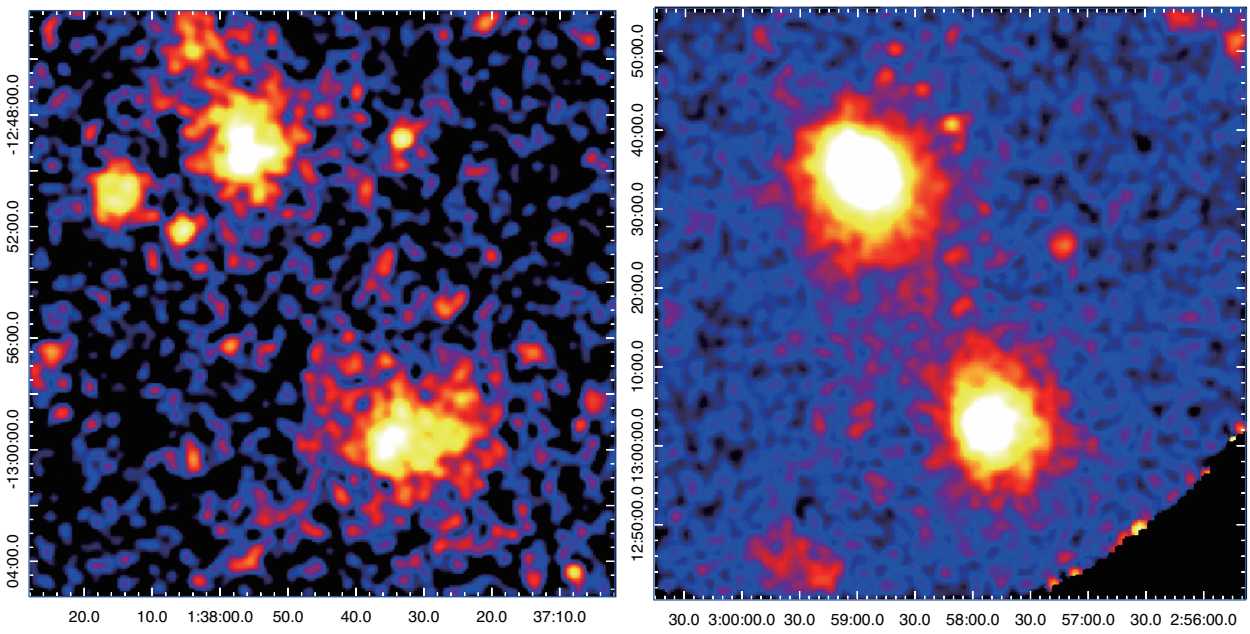

Figure 4.3: *Left panel*: An X-ray image of Abell 222–223 piars with ROSAT PSPC. The energy band is 0.1-2.4 keV. *Right panel*: An X-ray image of Abell 399–401 piars with ROSAT PSPC in the energy band is 0.1-2.4 keV.

of sight. The relatively small value suggests that the object is a suitable target to investigate in detail. The distance between clusters' cores is $13'.5$ which corresponds to (on-plane) 1100 kpc with a redshift of 0.07. Because the Virial radius of this cluster estimated from its temperature (as shown in Sec.6.3) is ~ 2 Mpc, it is not surprising if the ICM interaction has already been started. Although line-of-sight distance is not included in these estimations, X-ray morphology looks promising. This object has not been noticed due to the location in spite of such interesting features.

The morphology is similar to the famous early statge cluster mergers such as Abell 222–223 and Abell 399–401 as shown in Fig.4.3. The significant difference between CIZA J1359 and those two clusters is the degree of progression of merging. The redshift of Abell 222–223 and Abell 399–401 is 0.21 and 0.07, respectively, and the angular distances of center of clusters' cores are $11'$ and $35'$, respectively. Thus the actual on-plane distances of those are 2300 kpc and 2800 kpc, respectively. The distance of CIZA J1359 of 1100 kpc is indeed closer compared to them. The interaction is also much clearer from the brightness enhancement of the intermediate region.

4.3 Observational data used in this thesis

We have observed CIZA J1359 with Suzaku, Chandra, and XMM-Newton as summarized in Table.4.1. Suzaku was utilized to survey the entire spatial plasma temperature distribution, which indicates the collision dynamics of this object through observing from center to outermost region. ICM properties in cluster outermost region can be best studied with Suzaku because it has the stable and low background as well as the large effective area as described in Sec.3.1.1. As specified in Sec.3.3.1, Chandra has the outstanding angular resolution so that it was employed to investigate precise structures of around cluster's cores and shock

Table 4.1: Summary of observations used in this thesis.

Date	Instrument	OBS_ID	Pointing center	Exp. (ks)	PI
2013/01/21-23	Suzaku	807037010	center	62	Nishida
2014/08/10	Suzaku	509025010	north-east	42	Kato
2014/08/11	Suzaku	509028010	north-west	41	Kato
2014/08/12	Suzaku	509026010	south-east	40	Kato
2014/08/13	Suzaku	509027010	south-west	42	Kato
2015/06/02	Chandra	17665	center	20	Kato
2015/06/03	Chandra	17192	center	20	Kato
2016/08/24-25	XMM-Newton	0784980101	center	99	Kato

structures. With XMM-Newton, we inspected fine structures as well as temperature structures of these by taking advantage of the large effective area and the good angular resolution of 15″ represented in Sec.3.2.1. Fig.4.4 shows the field-of-view (FOV) of each satellite, used in this thesis.

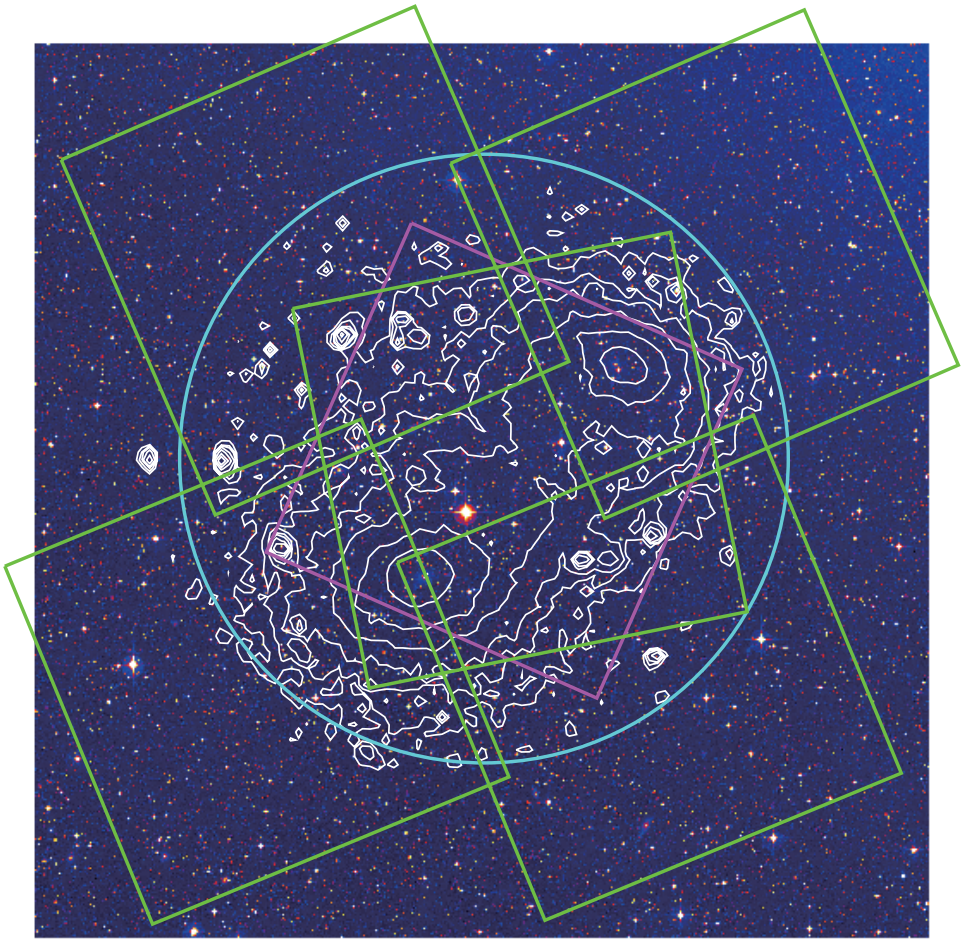

Figure 4.4: The FOV of each observatory. Green, magenta, and cyan represent the FOV of Suzaku, Chandra, and XMM-Newton (MOS2), respectively. An X-ray contour of CIZA J1359 with XMM-Newton in white color is superposed on an optical DSS image of $35' \times 35'$ field of veiw.

Chapter 5

Analysis of Suzaku observation data

5.1 Producing X-ray image

Suzaku 5 pointing observations covered whole this object, and the data were analyzed with standard screening and correction softwares included in HEAsoft package 6.19 and CALDB of 20160607 [1]. The XIS was operated in the normal full-frame clocking mode. In our analysis,

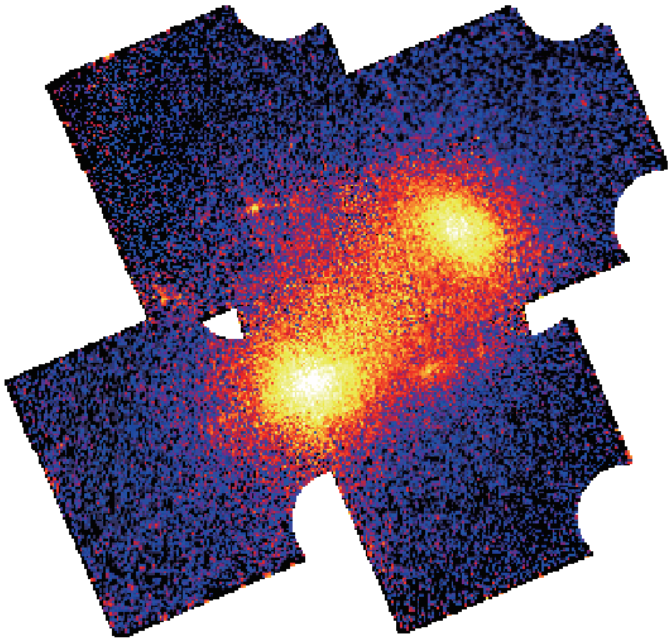

Figure 5.1: 5 pointing Suzaku XIS3 X-ray image of CIZA J1359 in the energy band of 0.5-10 keV. Vignetting correction and NXB subtraction is applied.

[1] see , "The Suzaku Data Reduction Guide" https://heasarc.gsfc.nasa.gov/docs/suzaku/analysis/abc/abc.html

we employed front illuminated CCD, XIS0 and XIS3, because the ICM has temperature of more than several keV and hence the higher energy band is important to determine the temperature. A period time in which the satellite observes the earth or passes through the South Atlantic Anomaly was removed. The effective area of XRT becomes small with the distance from the optical axis, which is called the "vignetting effect". Total usable exposure thus obtained was 62 ks for the central pointing, and $40 - 42$ ks in the other four pointing (as shown in Table.4.1).

With screened data, X-ray images of each observation in the energy band of 0.5–10 keV is created. These images contain the background signal, including the NXB. A tool *xisnxbgen* (Tawa N. et al 2008) provides a NXB image in the corresponding energy band. We run it and subtracted the obtained NXB images from the observation images. In order to correct the vignetting effect, we simulated flat sky images through XRT with the simulation soft, *XISSIM* in which Monte Carlo simulation is utilized, for each observation. Here the input X-ray spectra is modeled as a monotone flat emission at 2 keV for simplicity. Then, the all observations combined image is divided by the simulated images by weighting the each observation exposure. As described in Sec.3.1.2, calibration sources are installed on the corners of each XIS, and the regions are removed from the analysis. In Fig.5.2, the vignetting and exposure corrected image of 5 pointing XIS3 observations, in the energy band of 0.5–10 keV, of CIZA J1359 is shown. Because part of the XIS0 CCD cannot be used for observations, the whole CCD data is not used in this image, for simplicity. As shown below, it was used in the spectral analysis, on the contrary.

The observations captured an evident image of two separated diffuse radiation sources and the clear brightness enhancement connecting the two clusters of galaxies each other. The two sources are cores of each cluster. The bright bridge structure should be constructed owing to the strong interaction of these. There are 5 bright point sources contaminating the image (see also Fig.5.2).

5.2 Spectral analysis

Suzaku X-ray image implied a pair of clusters are colliding in the direction of line connecting each other. Therefore, we sliced spectral extraction regions as shown in Fig.5.2 in view of two objectives. The first is to survey the temperature distribution in the bridge region. The regions are defined towards the direction of the line connecting each cluster's core with a mesh shape. Those have width of $1'.25$ at least. This corresponds to almost half of the $2'$ HPD of Suzaku XRT, and considered as the minimum size to obtain meaningful positional resolution. The second objective is to see the opposite direction of bridge region where the impact of collision probably has not seem to be reached. Usually, clusters show temperature decrease gradient toward outside reflecting gravitational potential before a violent crash. In order to investigate the consequence of the collision, we made annulus regions toward the periphery. If the ICM mixing is not strong on the other side of the core, it will strengthen the assumption that the object is before the core crossing. The annular distance is from $1'.5$

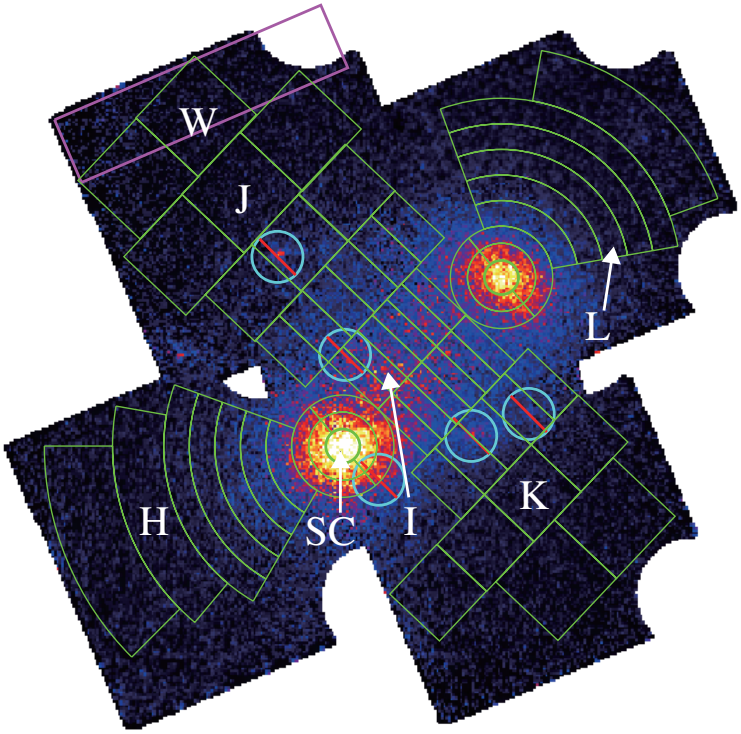

Figure 5.2: The same image as Fig.5.1, but for superposed the regions extracted spectra. The 5 cyan blue circles with radius of 1′.5 were excluded before extracting spectra because of point sources contamination.

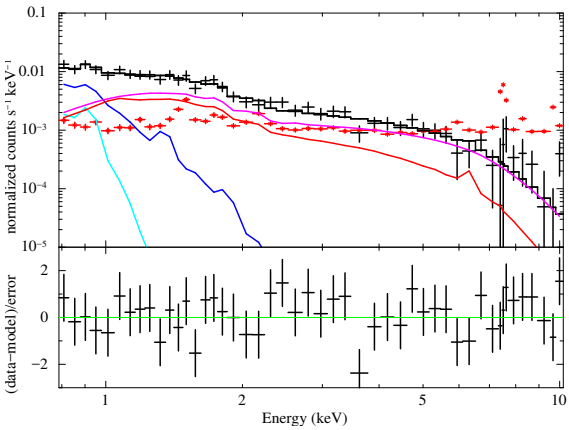

Figure 5.3: The spectra used to derive the parameter of background. Red, magenta, dark blue, and cyan solid line represent the ICM, CXB, MHW, and LHB components. respectively. The red dotted line expresses NXB shown for reference.

Table 5.1: The parameter of background components

	kT(keV)/Γ	norm ($\times 10^{-3}$)†
LHB+SWXB	0.06	400
MWH	0.25	3.13
CXB	(1.41)	(1.05)

† : The normalization of apec or powerlaw component on an assumption of emission from uniform extended objects with radius of $20'$, and thus the values are scaled by $1/400\pi$.

to $4'.0$, depending on the brightness (or statistics) of the region. The radius of circles or semi-circles regions around center of clusters' cores is 1' which is the same as the 2' HPD of Suzaku. The magenta box is to determine the background X-ray components modeling as detailed in the next subsection. We excluded the 5 bright point sources surrounded with cyan circles. XIS0 and XIS3 spectra were utilized and combined together in the analysis because those have similar response functions.

5.2.1 Estimation of X-ray and non-X-ray backgrounds

The X-ray spectra thus extracted contains, signals from the object, contribution from CXB and galactic foreground X-ray emissions (LHB, SWXB, and MHW), and NXB generated in the detector as described in Sec.3.5. To perform scientific data analysis, these background components must be estimated and subtracted from the signal data.

NXB spectra is generated with the *xisnxbgen*. It constructs NXB from the large database of "Night Earth" observations, which are the events obtained when the satellite FOV is looking at the night-side of the Earth. These data are considered to be primarily made of the NXB components, and are sorted by the geomagnetic cut-off rigidity. As already noted in Sec.3.5, It is known that the NXB spectra estimated from the database can reproduce the actual background spectra within an accuracy of 5% (Tawa N. et al. 2008). The NXB was subtracted before spectra fitting.

In order to estimate LHB, SWCX, MWH, and CXB parameters, we extracted a spectrum from the region surrounded by magenta box, as shown in Fig.5.5 left, where ICM emission is considered to be small. In Fig.5.3, the spectrum is shown. We fitted it with a model of

apec[LHB] + *wabs* × (*apec*[MHW] + *powerlaw*[CXB] + *apec*[ICM]) [model in XSPEC] to make the chi-square smallest. Powerlaw model represents the emission from CXB. In the *apec* model, plasma temperature, emission measure and abundance of elements are used as parameters. *wabs* expresses the photoabsorption within milky way by interstellar medium until photons reach the earth. The hydrogen column density is fixed as 11.5×10^{20} cm^2 derived from the intensity of hydrogen 21 cm line emission (Kalberla, P. M. W. et al. 2005) [2]. The relative large value reflects the low galactic latitude. The detail of spectral fit is described in Sec.5.2.2.

As described, SWXB is time variable so that deriving the correct parameters for all observations is uneasy. In order to make the effect small, the energy band < 0.8 keV in which SWCX and LHB dominate the spectra is not used. Similarly, we did not use the energy band above 10 keV, because the effective area of the XRT has a sharp cut-off at this energy and the NXB starts to dominate above this energy. By fitting the NXB subtracted data with the model, χ^2/d.o.f of 32.7/41 is obtained in the best fitting parameters. The derived normalization of CXB was about 20% higher than the average of whole sky. We tried to change and fix the value to the average value given Kushino et al. (2008) and fitted again, and then χ^2/d.o.f of 33.2/42 is acquired. It indicates that the spectrum cannot determine the normalization of CXB because of insufficient statistics. Therefore, we fixed the normalization to the average value. The background parameters used in this thesis are summarized in Table.5.1.

5.2.2 Spectral Fitting

All of NXB subtracted spectra are fitted by a model of with *apec*[LHB] + *wabs* × (*apec*[MHW] + *powerlaw*[CXB] + *apec*[ICM]) as the same to background spectrum fitting. In spectral fitting, the parameters of the background components are fixed as in Table.5.1. The value of redshift and abundance of the *apec* component representing the ICM are also fixed as 0.7 and 0.3 respectively, since the statistics is insufficient to determine those with small error bar. The abundance is typical value among clusters of galaxies (Werner et al. 2013). The all spectra are reproduced with χ^2/d.o.f of ~ 1, and typical examples are shown in Fig.5.4. We could not determine the ICM temperature at the region marked W because of insufficient statistics so that we ignored there.

5.3 Temperature and Density distribution

Fig.5.5 top panels show the plasma temperature distribution map and profile obtained through spectral fitting. The cores of southern and northern clusters of galaxies have the temperature of 6.0 ± 0.2 keV and 4.5 ± 0.2 keV within radius of 80 kpc, respectively. At least in Suzaku data, neighboring regions have similar temperature to the central portion. It implies that they are non-cool core clusters of galaxies. It is known that plasma temperature,

[2] see, https://heasarc.gsfc.nasa.gov/cgi-bin/Tools/w3nh/w3nh.pl

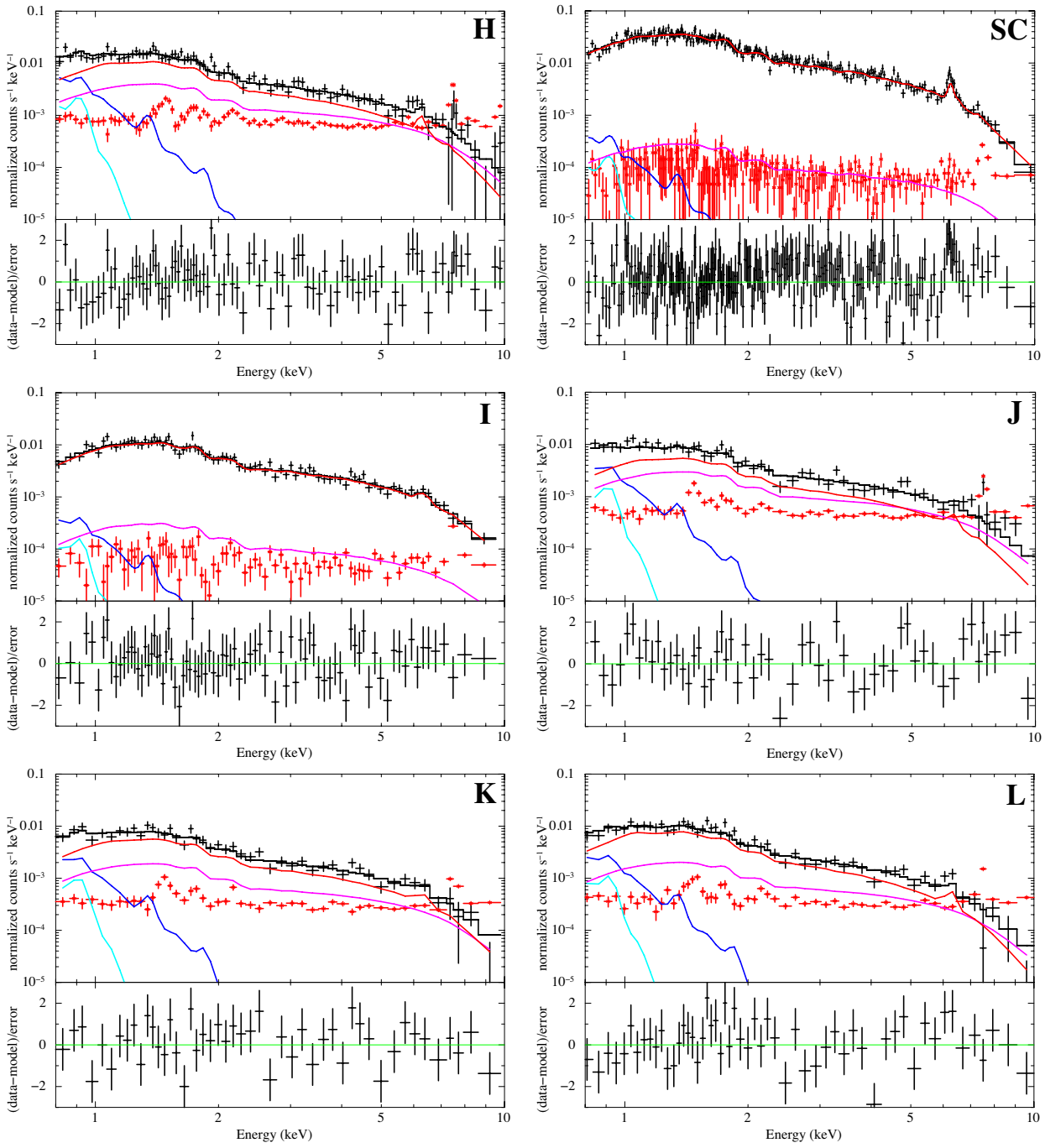

Figure 5.4: Several examples of spectra. The letters corresponds to the regions labeled in Fig.5.2. The colors are the same to the Fig.5.3

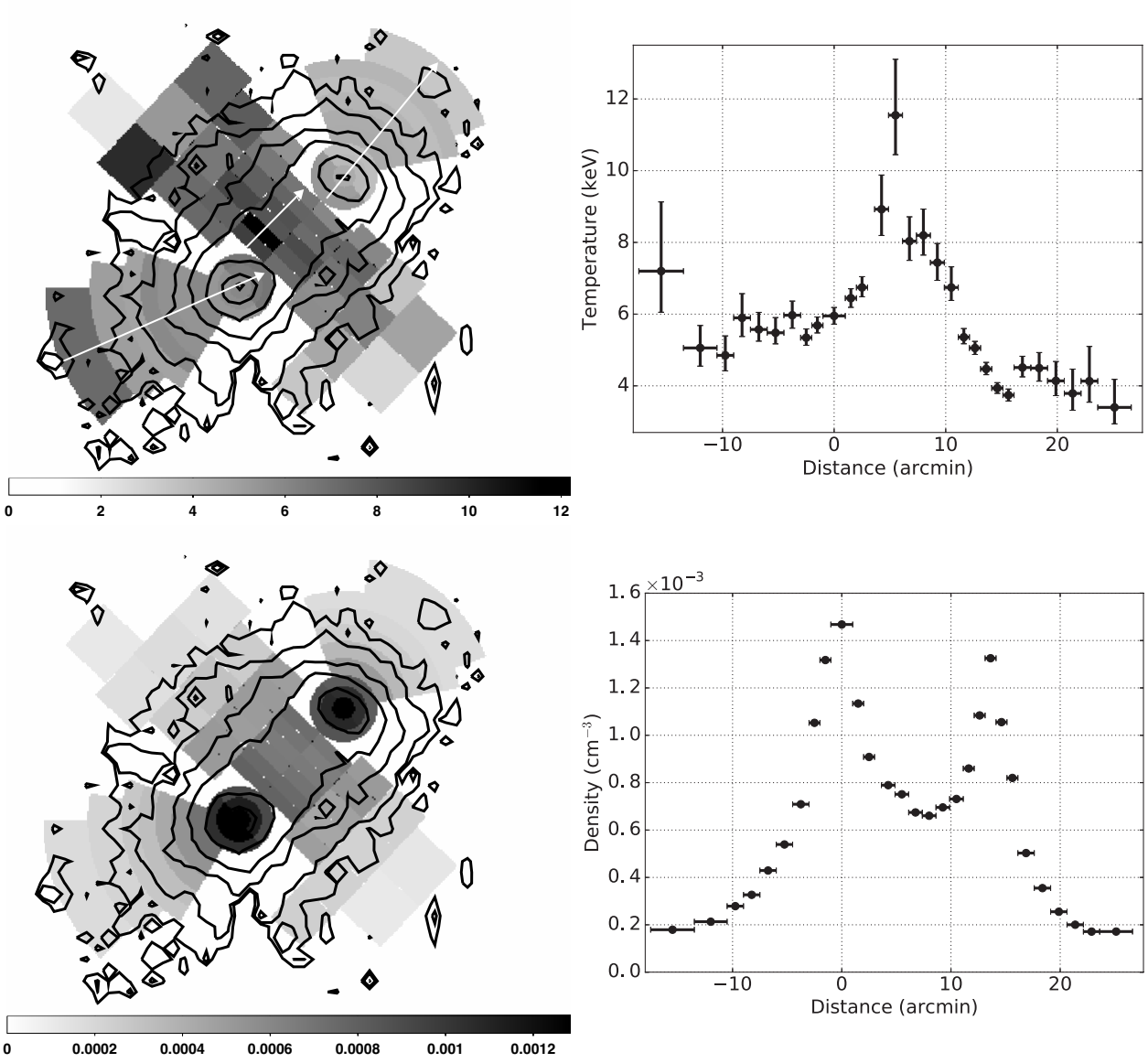

Figure 5.5: Temperature distribution and profile (top panel), and pseudo density distribution and profile (bottom panel) along the direction of the white arrow.

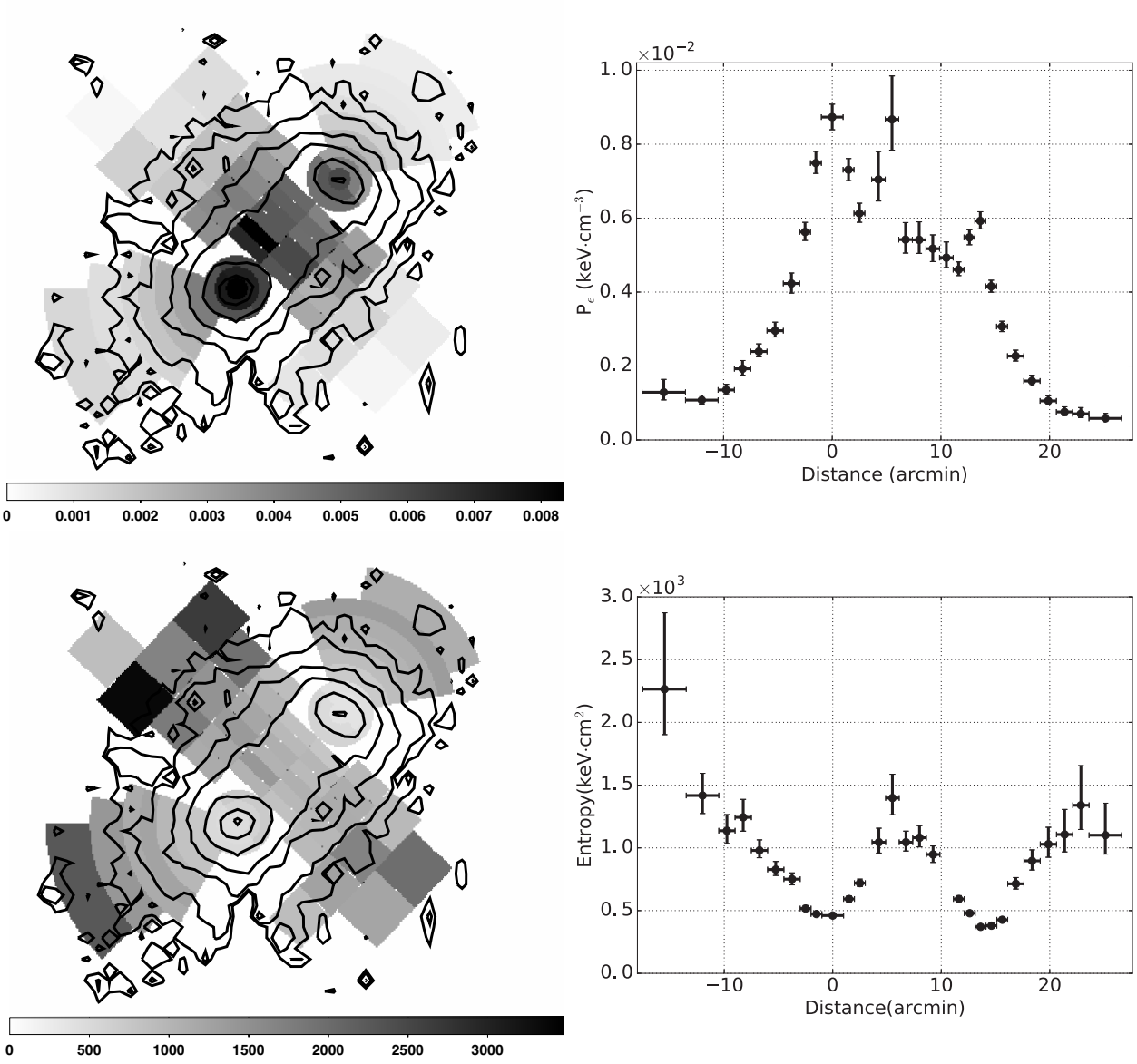

Figure 5.6: Pseudo pressure distribution and profile (top panel), and pseudo entropy distribution and profile (bottom panel) along the direction of the white arrow in Fig.5.5.

excluding the central one in cool core clusters, shows strong correlation with the total mass of a cluster. Therefore, the small temperature difference of about 30% suggests both objects have similar mass.

Temperature of the bridge region is more than 1.5 times higher than those cores, and the peak reaches $11.5^{+2.6}_{-1.8}$ keV at most. The opposite sides of southern and northern cores have tendency of gradual temperature decrease toward outmost regions, resembling a non-merging cluster's temperature profile. The temperature distribution indicates that strong interaction took place around the bridge region while the effect has not reached the opposite sides. This result and the brightness enhancement in the bridge region are the clear evidence for the early stage merger. Actually, the morphology is quite similar to an early phase merger in the numerical simulation of the top middle panel of Fig.1 of Akahori & Yoshikawa (2008). The positions of elliptical galaxies are coincident with the X-ray peaks, and is also supportive.

We also derived the value of density from the normalization as shown in bottom panel of Fig.5.5. An assumption of a shape of regions is necessary so as to transform the normalization to the density. The morphology of CIZA J1359 is, however, complex due to the merger. Therefore, we just assumed the shape of spectra extraction regions with a depth of 1 Mpc all over the regions for simplicity. Here 1 Mpc corresponds to $12'.5$ in the sky plane. The assumption is, of course, too simple, and thus we call the derived value 'pseudo' density. It shows clear bimodal distribution. The bridge region has higher value than the regions having the same distance from cluster cores' center. Therefore, compression should be caused in the bridge region as indicated from temperature distribution.

5.4 Pressure and Entropy distribution

The temperature distribution shows a peak around bridge region. It suggests the existence of a shock there. The good indicators of a shock are pressure and entropy values, because these show transition right behind shocks as described in Sec.2.4.2.

Pressure is expressed as $P_e = n_e k_B T$. We derived the value by multiplying the pseudo density to the temperature. The pseudo pressure map and profile are shown in top panel of Fig.5.6. It has significant jump at the highest temperature region as shown in the profile.

Entropy is defined as $s = \frac{3}{2} k_B \ln\left(\frac{k_B T_e}{\rho^{2/3}}\right)$ for an ideal gas. The contents of logarithmic, $K = \frac{k_B T}{(n_e)^{2/3}}$, is refereed as "entropy" in astrophysics conventionally as described in Sec.2.41. In the bottom panel of Fig.5.6 is the derived pseudo entropy. It indicates the jump at the same position of the pressure. Both of them imply the existence of a shock.

The Mach number of the shock is evaluated from Rankine-Hugoniot relations as described in Sec.2.4.1. Substituting the peak and in the front temperature of $11.5^{+2.6}_{-1.8}$ keV and $8.0^{+1.1}_{-0.9}$ as post- and pre-shock temperature, respectively, for the relations provides the Mach number of $1.44^{+0.21}_{-0.15}$.

5.5 The hot plasma gas extended toward northeast

Northeast part of the bridge region shows higher plasma temperature than southwest. Referring to the cluster merger simulation, the shock generated in-between the two cluster cores must be extended long along the direction perpendicular to the merging axis (Akahori et al. 2008), covering the whole width of the bridge. Current Suzaku temperature and density map implies that the shock is extended to the north-east but not to the south-east. Because the shock Mach number is relatively low, as shown in Sec.5.4, it will be possible that the west end of the collision surface somehow did not meet the shock generation threshold. Also, it is very important to see how the ICM is distributed to the north-east.

In order to study how far the hotter plasma extends, we sliced regions as shown in top left panel of Fig.5.7. From inner to the outer, it is name NW1–7. A point source contaminating the region is removed as the same region size of Sec.5.2. Top right, middle left and right in Fig.5.7 show the derived temperature, pseudo pressure, and pseudo entropy, respectively. We assumed the depth of 1 Mpc so as to estimate density for pressure and entropy as the same to previous section. The hot plasma extends, considerably, toward the outside and shows almost isothermal distribution. It shows sudden decline at 8'. Pressure and entropy also indicate dramatic decrease at the same position. Also, the *apec*-model normalization of NW4 and NW5 are $6.96^{+0.46}_{-0.51} \times 10^{-3}$ and $3.93^{+0.56}_{-0.61} \times 10^{-3}$, respectively. At the regions, the background emissions are dominant rather than ICM. Therefore, the derived parameters would be incorrect if the background components are under or overestimated. The two spectra represented in Fig.5.7 bottom left and right are extracted from region of NW4 and NW5 where ICM parameters transit significantly. Even in the region NW5, the spectra around 1.0–2.0 keV requires emission in addition to the background. Therefore, we certainly were able to see the ICM. NW5 one clearly has smaller ICM component than NW4, and thus the transition should be truthful. Furthermore, in oder to confirm that surely, we changed the normalization of CXB and NXB for a typical estimated value, by ±20% and ±5% (Kushino et al. 2002, Tawa et al. 2008), respectively, and derived systematic error of spectra. Then, region NW4 and NW5 spectra show temperature of $7.84^{+0.71+0.70}_{-1.48-0.72}$ keV (CXB, NXB) and $2.25^{+1.18+0.21}_{-0.54-0.29}$ keV, respectively. In other words, lower limit of the temperature at NW4, 6.19 keV (quadrature sum), is significantly higher than the upper limit at NW5, 3.45 keV. Therefore, we concluded that the parameters rapid transition is real.

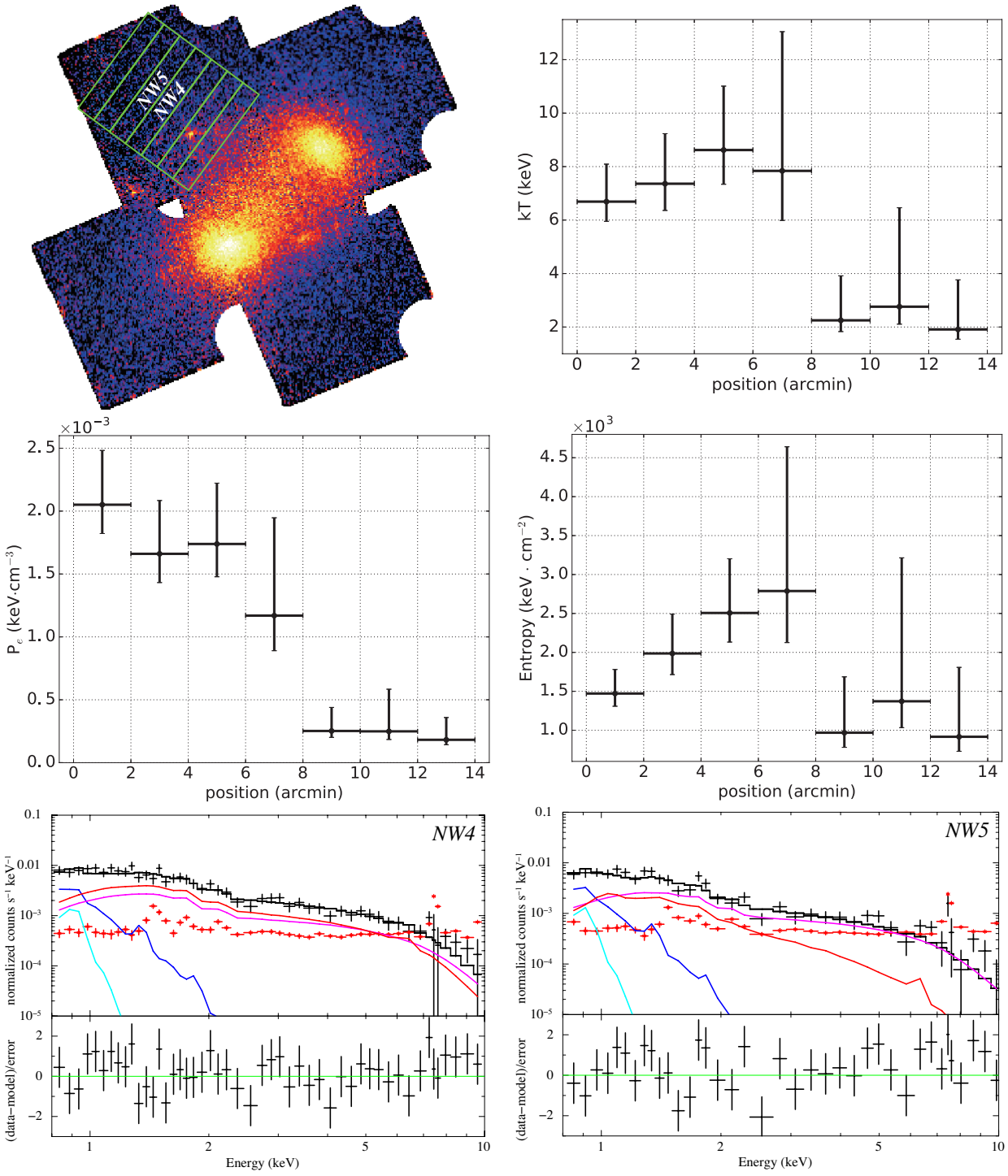

Figure 5.7: *Upper left*: The same image as Fig.5.1, but for superposed the regions extracted spectra. *Upper right*: The temperature distribution in north-east region. *Middle left*: The pseudo pressure distribution in north-east region. *Middle right*: The pseudo entropy distribution in north-east region. *Bottom left*: The spectrum extracted from region NW4. *Bottom right*: The spectrum extracted from region NW5.

Chapter 6

Chandra observation

The Chandra X-ray observatory has a superb angular resolution of $< 1''$, and is capable of identifying detail (or small) structures within the ICM, especially in the region with high surface brightness as described in Sec.3.3. In this observation, ACIS-I is used to cover both clusters' cores and the bridge region. The Chandra data was divided into two observation IDs with an exposure of 20 ks each.

6.1 Data reduction

CIAO version 4.7 and CALDB 4.7.2 supplied by Chandra X-ray Center are utilized to analyze the accumulated data. The event data were recalibrated using the tool *Chadra_repro*, a reprocessing script. Since Chandra often shows high count rates (or flare) intervals within observations due to cosmic-ray flares, it is necessary to exclude the period. In order to remove the flare intervals, we extracted a light curve of ACIS-S3 CCD positioned offset from the cluster. The light curve is screened using the *LC_CLEAN* script written by Dr. M. Markevithch. The acquired filtered data have exposures of 18 ks and 19 ks for the two pointing observations, 17192 and 17665, respectively. An exposure corrected image in the energy band of 0.5–5.0 keV is obtained through combining those data with *merge_obs* script. Point sources within field of view are detected with the scripts *wavdetect* and then removed after inspected by our eyes. Those regions are extrapolated from pixel counts around the regions by sampling the Poisson distribution.

The processed image is shown in Fig.6.1. The image reveals bridge structure and shapes of clusters clearly better than the Suzaku observations thanks to the supreme angular resolution. Both southeast and northwest cores shapes are not spherical, but the former one is extended to north-west direction and latter one has some tail to south-east. Furthermore, the central region of bridge structure in which hot component was discovered with Suzaku showed brightness enhanced structure with a length of 8'$\sim$640 kpc from north-east to south-west, and a thickness of $\sim 2'$ along the merger axis. The enhanced band region is associated with dark band region (or cavity) to the north, which is not apparent to the west.

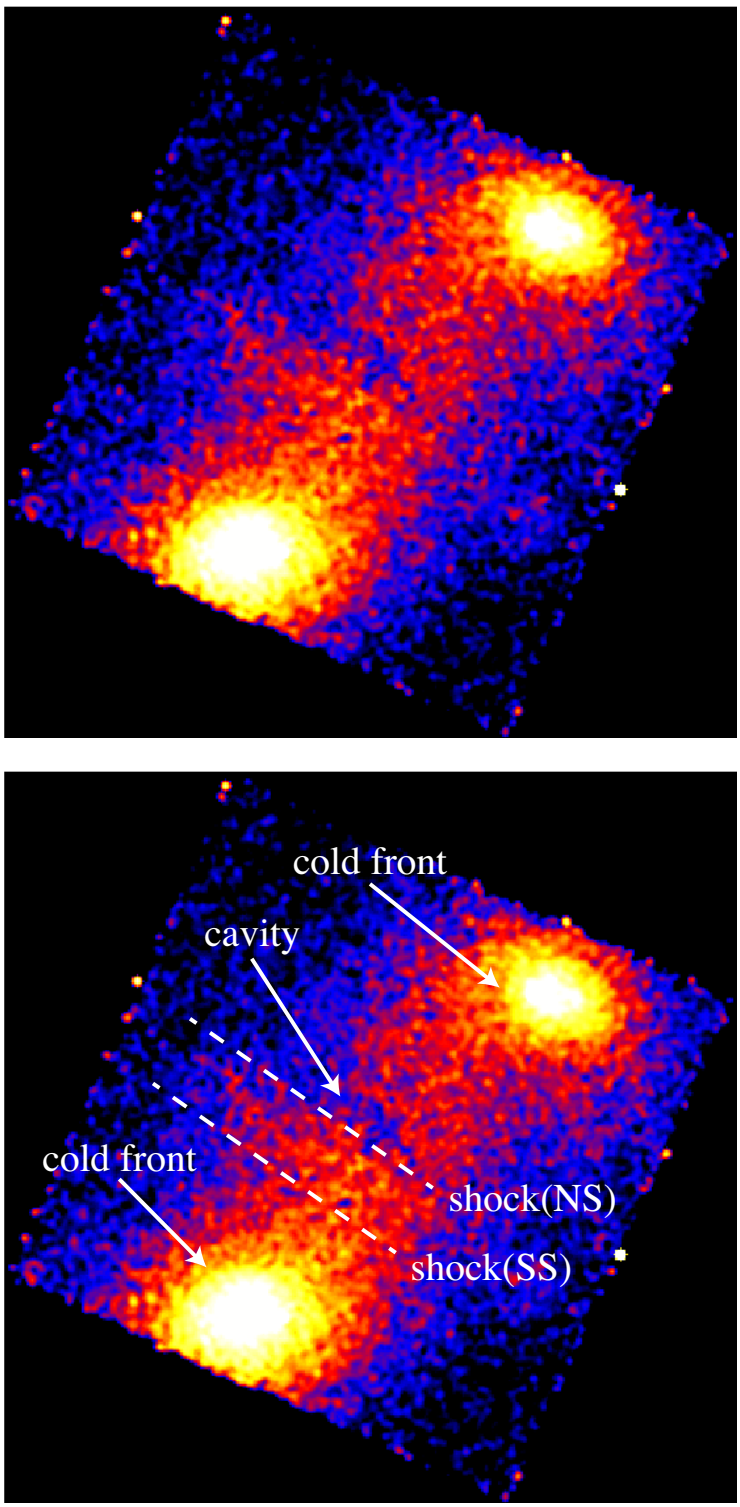

Figure 6.1: Top: An X-ray image of CIZA J1359 with Chandra in the energy band of 0.5-5.0 keV. Point sources are removed and exposure correction is applied. Bottom: The same as the top, but for written the structures.

6.2 The linear brightness enhancement structure

In order to examine those structures thoroughly, we extracted brightness cross-section from 5 belt regions surrounded by while lines named (a)–(e) in the top left panel of Fig.6.2. The regions' size are $120'' \times 900''$. As a result, region (a) exhibits a brightness hump associated with two jumps around $x = 330''$ and $460''$. Here x is defined as the distance from the south-east core. Region (b) shows only one jump, but a one very sharp and significant. Because the location is just on a CCD gap, the dramatic jump would be due to it though the transition itself must be real. In region (c) and (d), the change is small and becomes almost flat in region (e). Those transitions are relatively sharp so that it is suggested the merging is taking place almost within the sky-plane.

The position of brightness transition corresponds to the region where the ICM temperature and entropy derived with Suzaku showed a positive jump. The transition is significant in north-east and becomes weak gradually toward south-east. The result is quite similar to the temperature distribution of Suzaku. The positional coincidence between the temperature peak and the brightness transitions is clear signature of shocks. The two transition in (a) indicates there are a twin shocks. Let us tentatively call them North Shock (NS) and South Shock (SS), as indicated in Fig.6.1.

We also found a clear dip in front of the shock-candidate. It can be caused by another brightness enhancement to the north, or as a cavity in this region. The brightness rapidly increase in front of the dark band (or at the northern edge of the dark band) again as clearly indicated in region (b) and (d). This structure will also be discussed in Sec.9.2.

6.3 Cold fronts structure

In Chandra image of CIZA J1359, there seems to be surface brightness transitions around both clusters' cores. In order to investigate the symptoms, we extracted surface brightness distribution from the region surrounded black, red, and green annular in left panel of Fig.6.3. The right panel of the figure shows the distribution and the colors corresponds to the regions extracted the brightness. The core of south cluster (green) shows two transitions at $x = 40'' - 45''$ and $80'' - 85''$ with 2.7 and 4.0 σ, respectively. Here x is defined as a distance from each cluster core. In the north one, the direction of bridge region (red) suggests surface brightness transition at $x = 35'' - 45''$ and $65 - 75''$ with 2.6 and 2.9 σ, respectively. The opposite side (black) indicates jump at $x = 70'' - 75''$ and $110 - 115''$ with 3.5 and 2.7 σ, respectively. Those indicate the existence of cold fronts.

Cold fronts forward to the two cores can be qualitatively explained if the merging is causing gas stripping. Actually, the distance between the two cores is only 1.1 Mpc. From the temperature of the cores, the estimated Virial radius of the north and south clusters are 1.8 Mpc and 2.1 Mpc (D.M Newman 2005), respectively. Therefore, gas compression must be already started and cold front existence is consistent with this view.

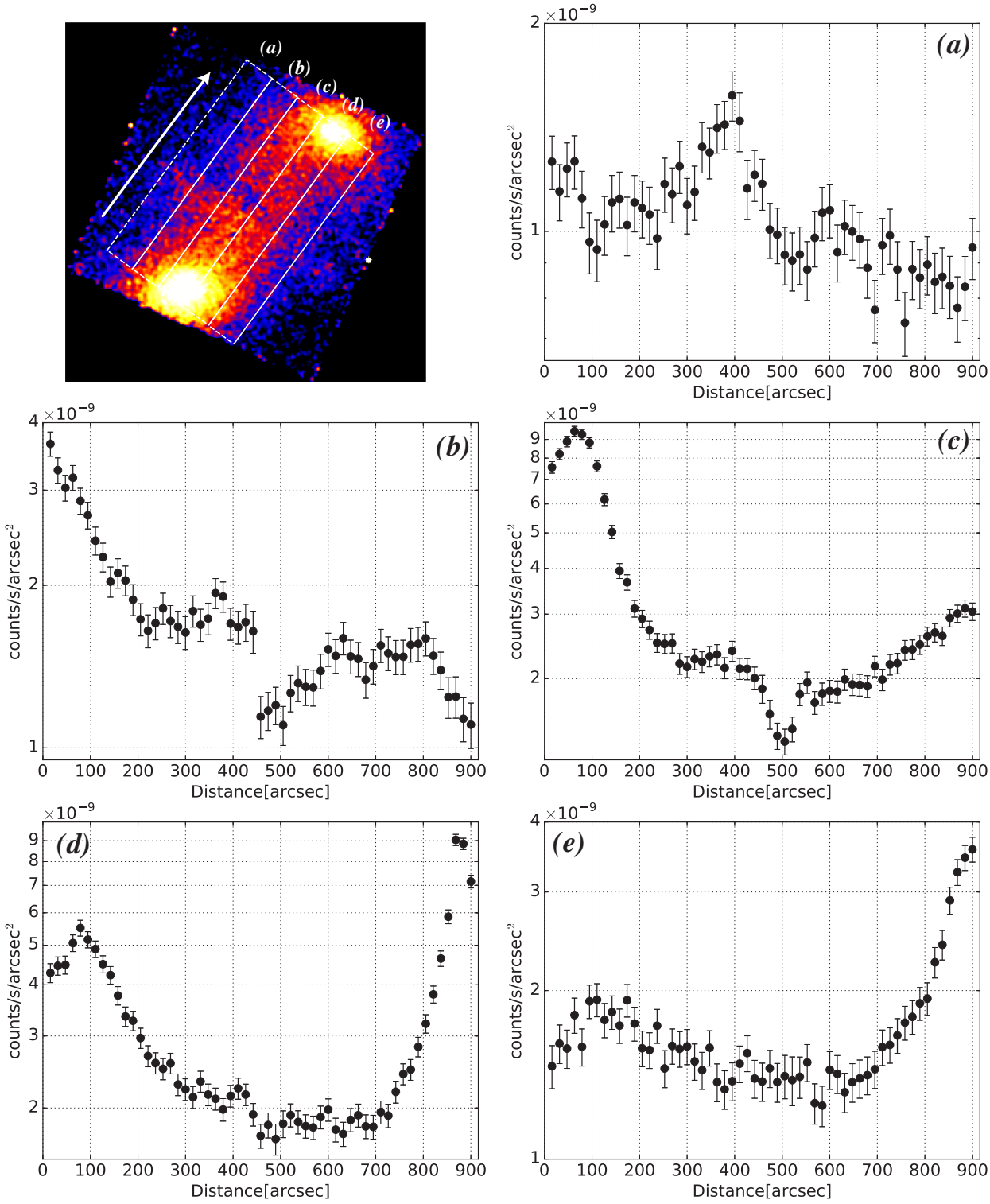

Figure 6.2: The brightness distribution of CIZA J1359 with Chandra. Those are derived from the regions surrounded with white boxes along the direction of the arrow in top left panel. The letters indicate the position.

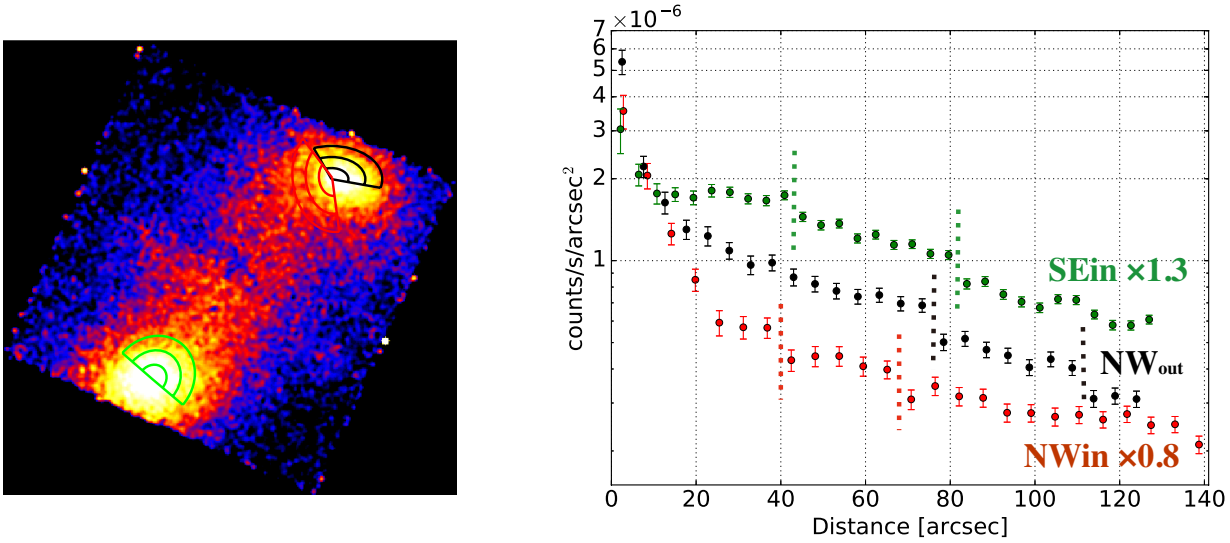

Figure 6.3: Left: The same image as Fig.6.1, but for supposed the regions where brightness distribution is extracted. Right: The surface brightness of both cores of clusters. The colors correspond to the regions in the left panel. The dot lines represent the position where the brightness express transitions.

Chapter 7

XMM-Newton

As described in Sec.3.2, XMM-Newton has large FOV with a radius of $30'$ and good angular resolution of $5' - 15'$ so that it is suitable to investigate general view of a cluster system. We conducted a long exposure observation of CIZA J1359 with XMM-newton in 2016.

7.1 Data reduction

The observation data is proessed using the Science Analysis System (SAS) software v16.0.0. The analysis of extended source needs special care so that XMM-Newton Extended Source Analysis Software (XMM-ESAS) package was developed. We used the XMM-ESAS version 5.9 (S. L. Snowden & K. D. Kuntz 2014) in this thesis.

According to COOK BOOK of ESAS [1], we run *emchain* or *epchain* and *mos-filter* or *pn-filter* for the MOS or PN data, respectively. Those scripts process and filter the data. In order to exclude soft proton flares (similar to those seen in Chandra), *mos-filter* or *pn-filter* makes count rate histogram from the FOV data, and fit it with a Gaussian function to the peak. It removes the time-intervals with count-rate lower or higher than 1.5 σ. The obtained cleaned data exposures are 85, 86, and 65 ks for MOS1, MOS2, and PN, respectively.

With the cleaned data, we created the images of CIZA J1359 with MOS1 and MOS2 in the energy band of 0.8–1.25 and 2.0-7.2 keV using a script *mos-spectra*. As the same to MOS, the image with PN is generated using a script *pn-spectra*. The energy band of 1.25–2.0 KeV is contaminated from Al Kα ($\sim$ 1.49 keV) and Si Kα ($\sim$ 1.75 keV) fluorescent instrumental lines for MOS, and Al Kα ($\sim$ 1.49 keV) for PN, and thus ignored. The energy screened images are combined and exposure correction is applied for using scripts *comb* and *adapt*, respectively. Fig.7.1 shows MOS1, MOS2, and PN individual images. Two (CCD3 and 6) of the MOS1 CCD chips are not working well since 2005 and 2012, respectively, and thus not used here.

[1] see, https://heasarc.gsfc.nasa.gov/docs/xmm/esas/cookbook/xmm-esas.html

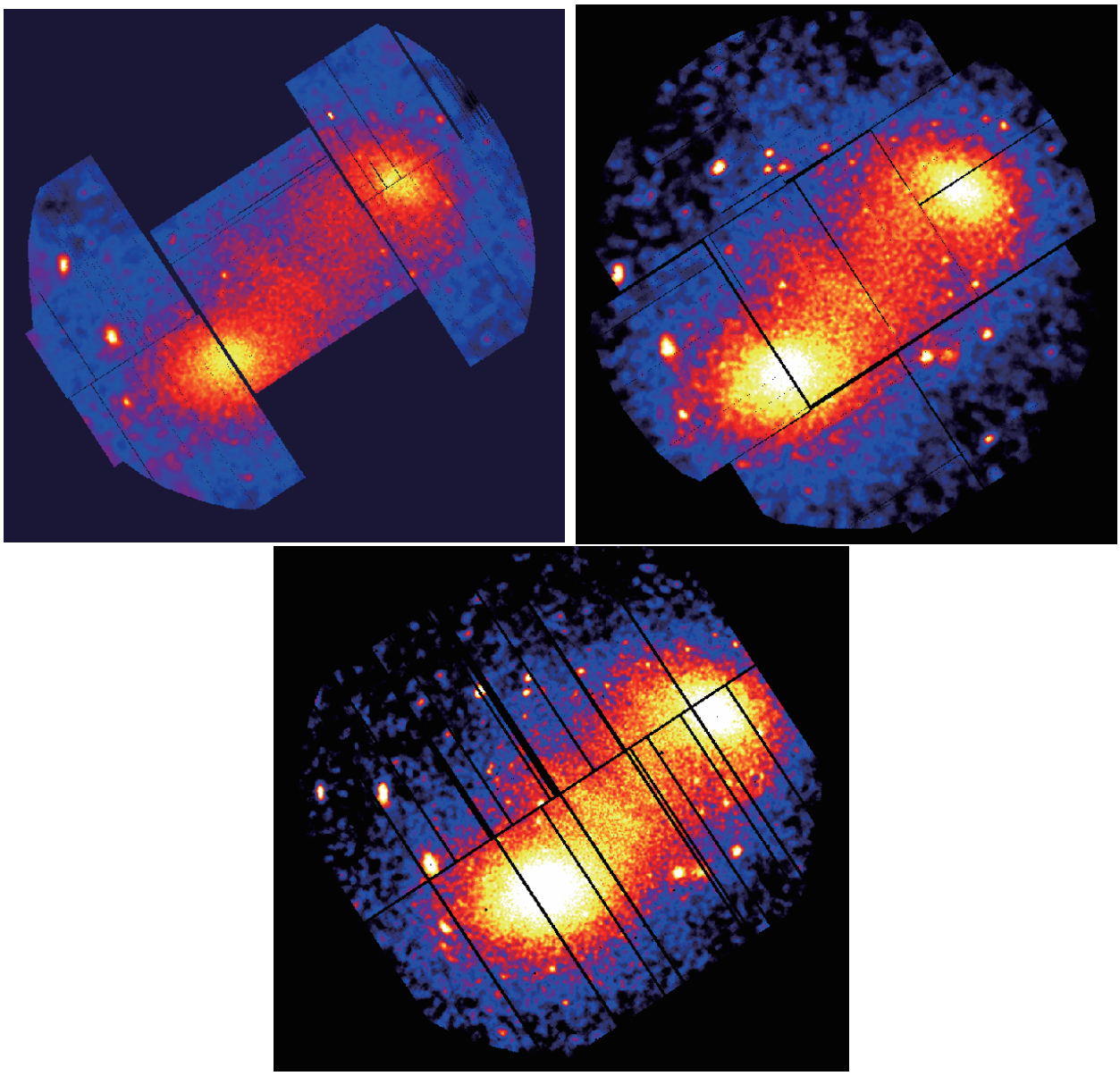

Figure 7.1: The exposure corrected and background subtracted X-ray images of CIZA J1359 in energy band of 0.8–7.2 keV with MOS1 (left), MOS2 (right) and PN (bottom).

7.2 Reconfirmation of the linear structure

To increase statistics, we combined MOS2 and PN images as shown in Fig.7.2. Here MOS1 is not used to keep the exposure (and hence the statistics) relatively flat. The X-ray image reconfirms the clear brightness enhancement and the dark band (or cavity) in the bridge region thanks to the large statistics. There is another enhancement on the northern part of the bridge region. In MOS images in Fig.7.1, however, there is no such a structure. Therefore, we concluded that the edge to the north here a phony structure caused by CCD gaps of PN as it is just right on the gaps. The location of these structures are written in Fig.7.2.

As the same to Sec.6.2, we extracted brightness distribution from (a)–(e) to investigate structures with the higher statistics. The geometry of the 5 regions are the same as those used in the Chandra analysis. Point sources are removed and extrapolated with the same method used in Chandra analysis before extracting the brightness to avoid contaminations.

Fig.7.4 shows the results of brightness distribution. All of them have similar distribution to those of Chandra, and reveal the structures clearer, with the higher statistics. (a) indicates explicit significant transition twice at $x = 250''$ and $450''$. There also is a jump at around $350''$. (b) shows a jump at $x = 330''$ which could not be seen in Chandra due to the small statistics, though it is small. The gradual decrease of the profiles is observed around $x = 400'$–$500'$, while the sharp edge seen in Chandra image is not confirmed. We thus conclude the edge observed with Chandra is caused by systematics around handling the CCD edge. The transition at $660''$ is a phony jump caused by a PN CCD gap (see the next section). (c)–(d) are quite similar to the results of Chandra.

7.3 The dark band and phony structure

As discussed in Sec.7.1, a structure probably caused by PN CCD gap is found in northern part of the bridge region. In order to confirm that this is a false structure, and also to inspect the dark band region behind the structure. We extracted the brightness distribution of PN+MOS2 and MOS2 images from a green box with a size of $240'' \times 480''$ in the left panel of Fig.7.5, respectively. The right panel of Fig.7.5 shows the result. Apparently, PN+MOS2 one shows brightness transition at $x = 300'' - 310''$, whereas MOS2's profile indicates flat distribution. Also, it is located on the CCD edge of the PN detector. Therefore, the transition is certainly a phony structure.

The dark band (or cavity) structure, which is also indicated by Chandra, is seen clearly. The brightness change itself is large and reaches 25 % from peak to the bottom, but gentle. The temperature distribution with Suzaku does not show significant jump there. Therefore, the cavity structure would be neither shocks nor cold fronts.

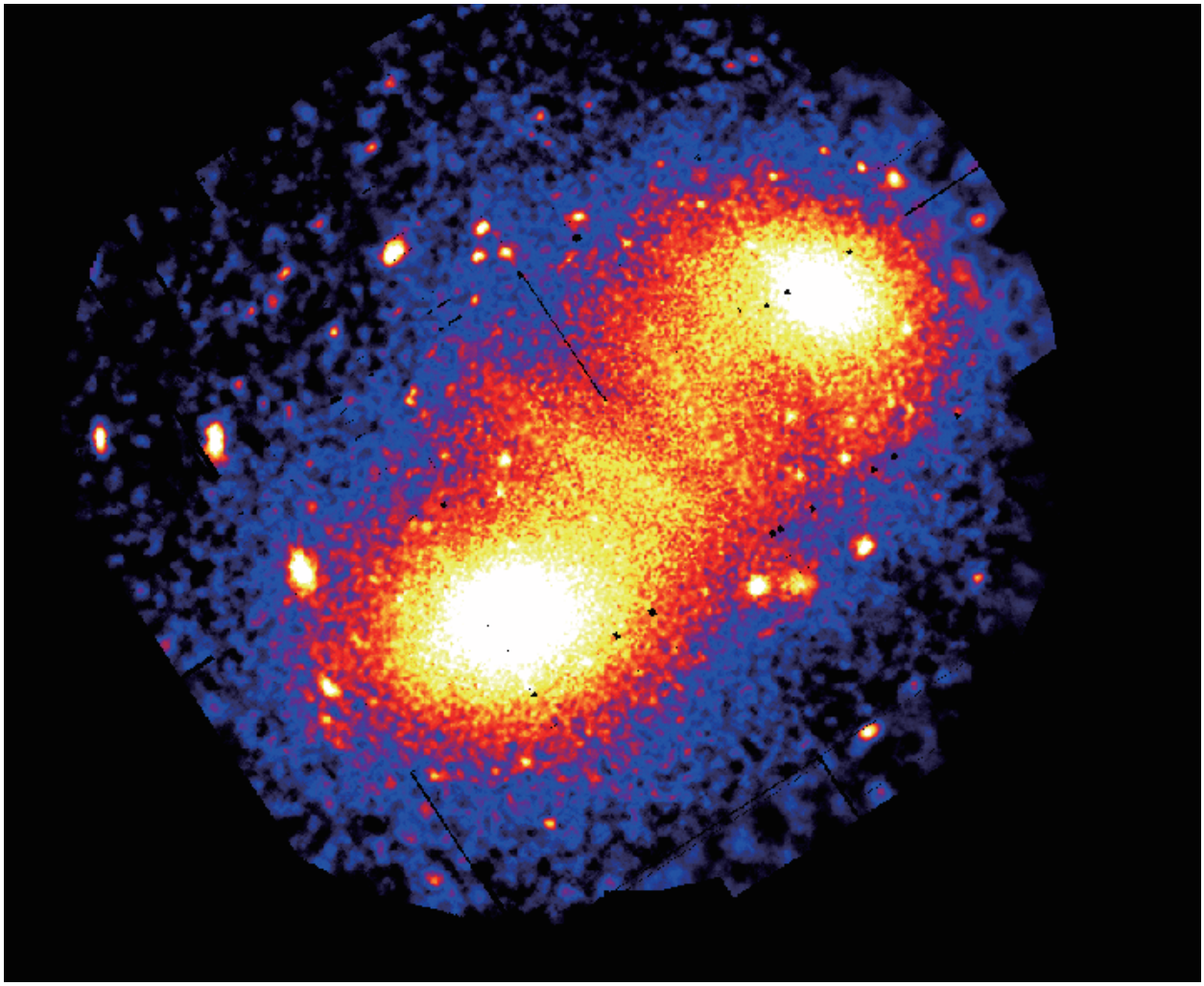

Figure 7.2: The MOS2 and PN combined X-ray image of CIZA J1359 with the energy band of 0.8–7.2 keV.

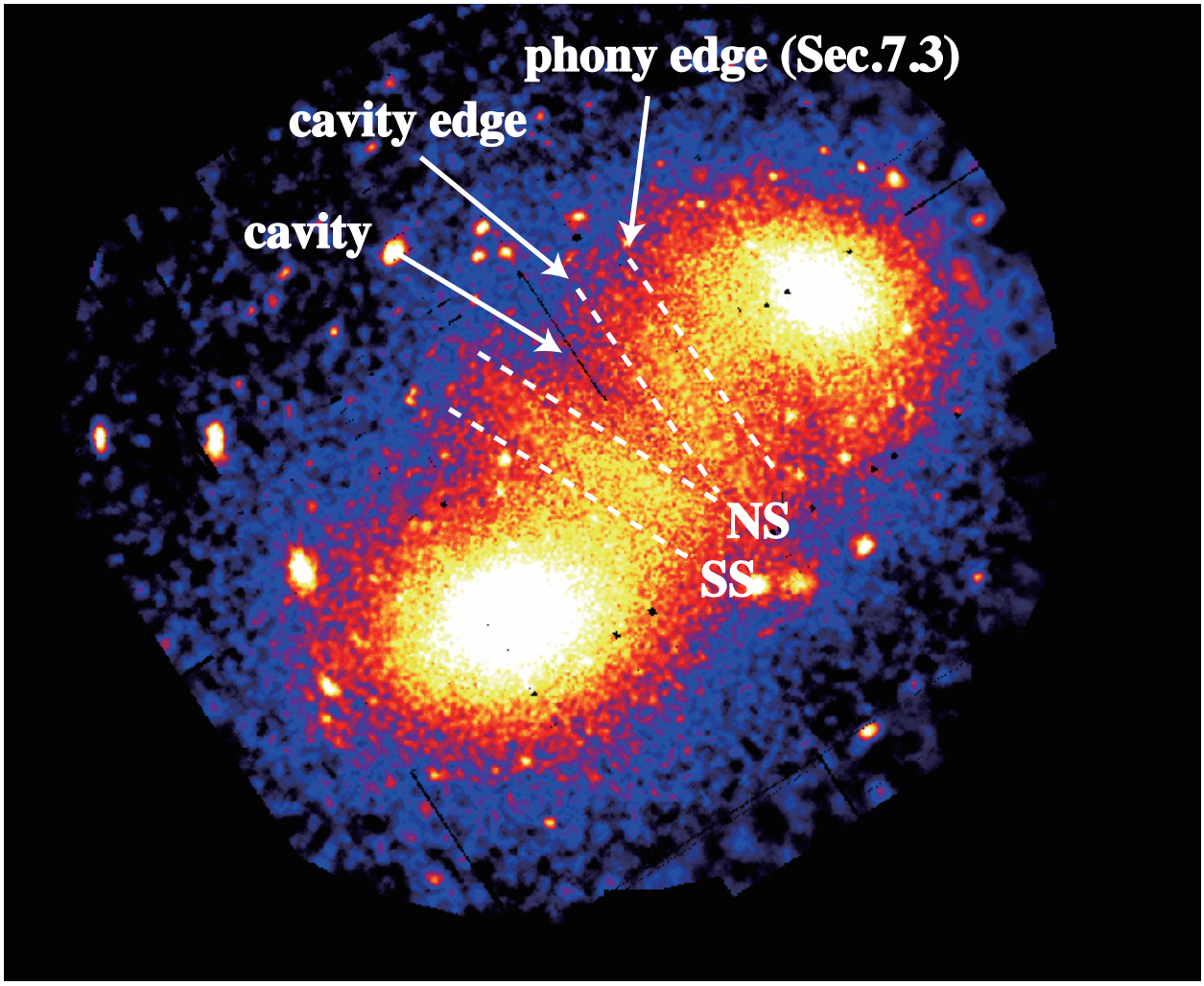

Figure 7.3: The same image as Fig.7.2, but for written the structures.

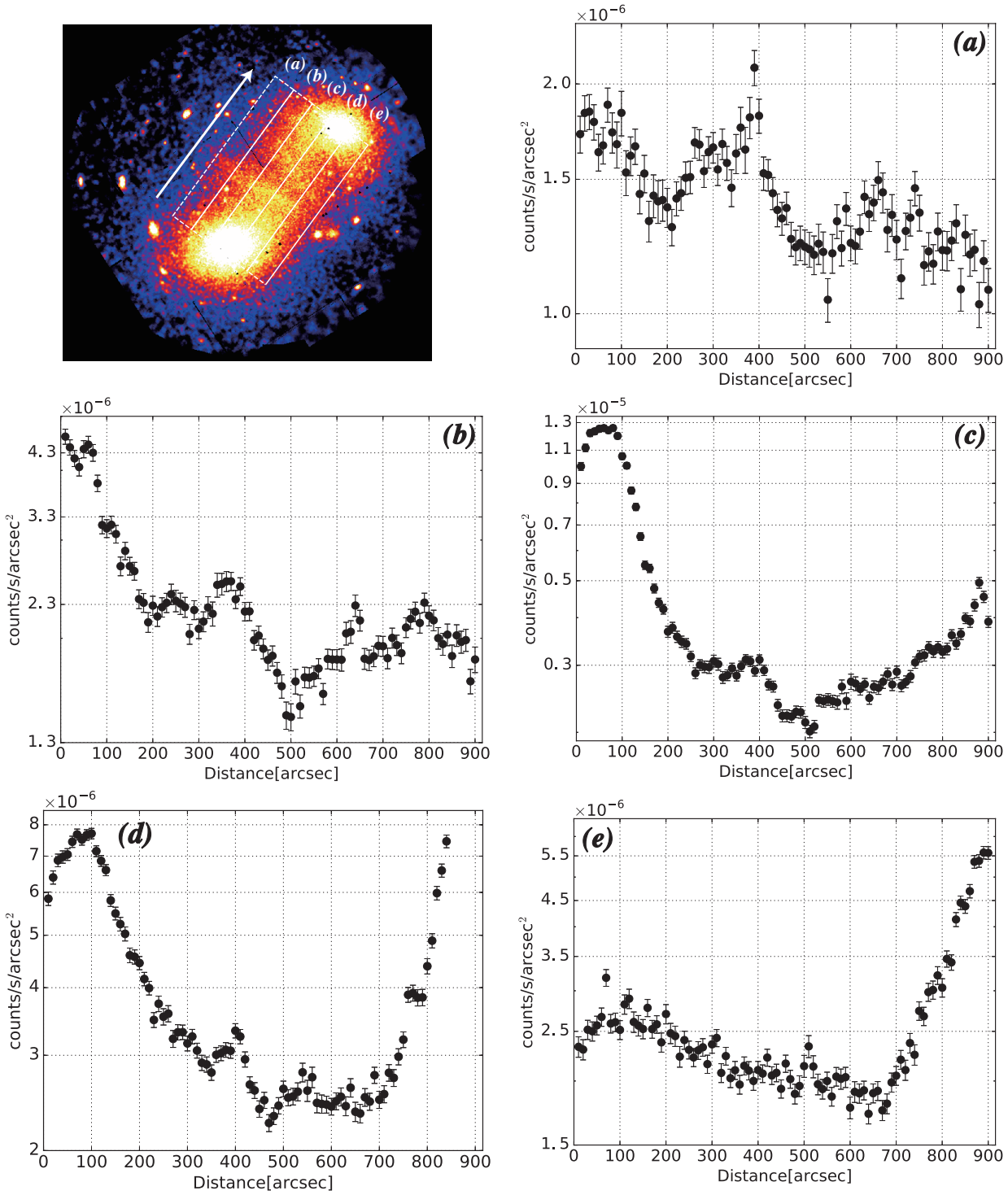

Figure 7.4: The brightness distribution of CIZA J1359 with XMM-Newton. Those are derived from the regions surrounded with green boxes in top left figure. The letters indicate the position.

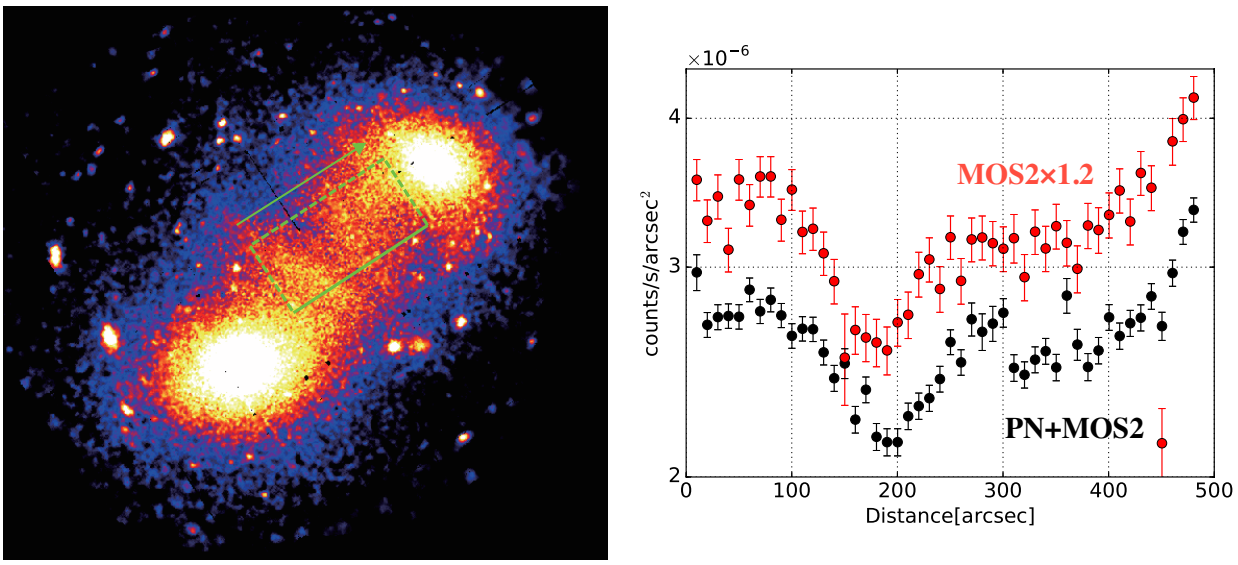

Figure 7.5: Left: The same image as Fig.7.1, but for supposed the region where brightness is extracted. Right: The brightness distribution of MOS2 (red) and PN+MOS2 (black) along the direction of the arrow in the left panel. MOS2's distribution is multiplied 1.2 times.

7.4 ICM parameters

XMM-Newton has much higher angular resolution than Suzaku. Therefore, it enables us to inspect ICM parameters with smaller size regions. In order to derive the parameters around the brightness enhancement regions, we sliced regions as green boxes with size of $30'' \times 480''$ as shown in the top left panel of Fig.7.6. Since the MOS1 data shows some anomaly in CCDs except CCD1, the data analysis becomes complicated while it contributes only 1/4 of the statistics. In this regard, we decided not to use MOS1 in this analysis. We used *cheese* script so as to detect point sources which has flux of more than 1.0×10^{-14} erg cm^{-2} s^{-1}. These regions are excluded from spectra extraction regions. *mos-spectra* or *pn-spectra* also provides ARFs and RMFs. The NXB spectra were derived with a script *mos-back* or *pn-back*. The scripts construct these from quiescent particle background data included in CALDB.

We fitted the background subtracted spectra with the model of *apec*[LHB] + *wabs* × (*apec*[MHW] + *powerlaw*[CXB] + *apec*[ICM]) as the same to in Sec.5.2. The X-ray backgrounds parameters are fixed in Table.5.1 in the same way as Suzaku spectral analysis. In the top right panel of Fig.7.6 shows an example of spectrum of MOS2 (red) and PN (black) extracted from region B5 as shown in the left panel of Fig.7.6. The energy band of 1.35–1.9 keV is ignored for MOS2. This is because the contamination of Al Kα and Si Kα lines as described in Sec.7.1. The same as MOS2, the energy band of 1.35–1.6 keV is ignored in the PN data due to Si Kα line.

We derived the ICM parameters from MOS2 and PN separately, because it is known that they often show inconsistent temperature due to non-negligible calibration inaccuracy. The middle left panel of Fig.7.6 shows the results of temperature. Apparently, MOS2 and PN

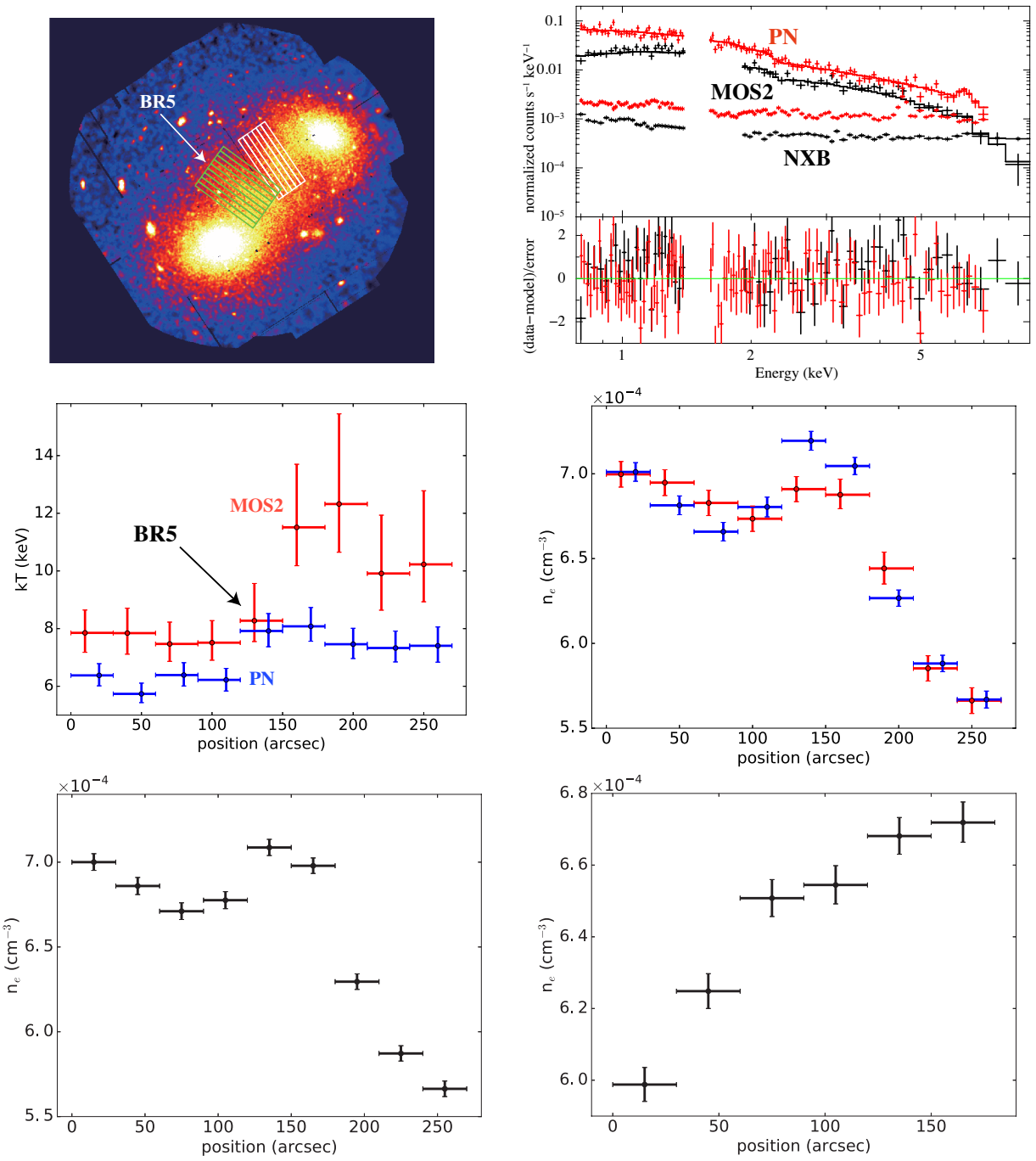

Figure 7.6: Top left: The same image as Fig.7.1, but for supposed the region where spectra are extracted. Top right: An example of spectrum of MOS2 (black) and PN (red) from BR5. Middle left: The temperature distribution derived from green boxes with MOS2 (red) and PN (blue) separately. Middle right: The density distribution derived from green boxes with MOS2 (red) and PN (blue) separately. Bottom left: The density distribution from green boxes derived simultaneous fitting of MOS2 and PN spectra. Bottom right: The density distribution from white boxes derived simultaneous fitting of MOS2 and PN spectra.

offset each other. Overall, the XMM-Newton's calibration has some ambiguity especially for hotter ICM temperature, as also seen as inconsistent shift in the MOS and PN profiles. This is considered to be originating from the inconsistency of effective area calibration between MOS and PN, as well as those to Chandra ACIS and Suzaku XIS. Usually, MOS2 shows more consistent temperature with Chandra results than PN (Schellenberger et al. 2015). Therefore, we should use the result of MOS2. The statistics is, however, small and the errorbar is large so that we decided not to use the temperature distribution in this thesis.

We also obtained the pseudo density distribution on the same assumption as Sec.5.3. The values are almost consistent between MOS2 and PN while the temperature is not. Hence, the density would be correct. To increase statistics, we fitted MOS2 and PN spectra simultaneously to derive the density. The result is shown in the bottom left panel of Fig.7.6. It shows a twin jump which corresponds to brightness distribution. These are caused by shocks so that we are able to obtain the Mach number from the density ratio of pre- and post shock regions. The Mach number of SS and NS are $1.04^{+0.01}_{-0.01}$ and $1.07^{+0.01}_{-0.01}$, respectively. The values are quite low and indicate the activated shocks are peculiar. In addition, the value itself is even lower than those derived from Suzaku temperature jump. This issue is discussed in Sec.9.2.

In the same method as green boxes, we also derived the density distribution from white boxes in the top left panel of Fig.7.6 so as to see the density variation around the cavity structure. The bottom right panel of Fig.7.6 shows the result. It shows density decline as expected, and the change about 10 %. Nature of this jump is briefly discussed in Sec.9.3, as well.

Chapter 8

Comparison between satellites results

We found a signature of a twin shocks and a post-shock region candidate in between, using Suzaku, Chandra, and XMM-Newton. In order to confirm the consistency of the results from 3 different observatories, we compared brightness, temperature, and density profiles from them, using the region shown in Fig.8.1. The over all region covers the same one as we used in the XMM-Newton observation (at Sec.7.4), as shown in Fig.7.6, while the binning size differs among the observatories.

The brightness distributions are shown in the top-left panel of Fig.8.2. Here, for comparison, the absolute value is arbitrary changed by multiplying a factor to Suzaku and Chandra brightness profiles. These of Chandra and XMM-Newton are apparently consistent each other. On the other hand, that of Suzaku is lower around $\sim 130''$ and higher at $> 200''$. Because the angular resolution of Suzaku is $120''$ HPD (or $1'$ half-power-radius), these deviations can be explained by the smoothing effect caused by it. Also, it should be noted that the attitude reconstruction accuracy of Suzaku is also low, $\sim 20''$ (Uchiyama et al. 2008).

Apparently, Suzaku and Chandra do not have enough PSF and statistics, respectively, to determine the correct location of the shocks. Therefore, we decided to use XMM-Newton data having the largest statistics for determination of the shocks' location. For clarity, we draw two vertical red lines in the top-left panel of Fig.8.2, as defined as 10% level of count increase in the brightness jumps. The location of shocks are $105''$ and $215''$ so that the width of post-shock region is 110" $\sim$ 70 kpc.

We also compared the physical parameter obtained by the spectral fitting. Suzaku has good statistics as well as smaller background but because of its $120''$ HPD angular resolution, we divided the region by $54''$ apart. Chandra has the best angular resolution, but with the least statistics. Therefore, we also defined the region width to be $54''$ here. The region definition of XMM-Newton is in $30''$ width, which is the same as we used in Sec.7.4. Here, to see the consistency, the same energy band of 0.8–7.0 keV was used among all the data. The derived temperature and density are shown in the top-right and bottom panels of Fig.8.2, respectively.

The tendency of density profiles of three satellites are similar to each other, although Suzaku and Chandra have an offset of about 10%. This shall be explained by the PSF

differences as the same to the brightness profiles and the absolute effective area calibration accuracy.

The Suzaku temperature profile shows an increase around $x = 120''$, presumably around the shock. Compared to the analysis in Sec.5.3, the hottest temperature is modest. This can be caused by wider (east-west) size of the region, which is averaging the temperature jump along the candidate shock-front. Similarly, PN (blue) driven temperature shows jump around $x = 120''$. On the other hand, temperature profile of Chandra data shows deviation at around $x = 70''$, i.e. the 2nd region from the left edge, and that of MOS (red) shows deviation at around $x = 170''$, i.e. the 7th region from the left edge. The temperature profiles in other regions are generally consistent within 90% confidence interval. Among the 2 problematic regions, the former (of Chandra) has low statistics and some dip in at $E < 1.0$ keV and hump at $E > 5.0$ keV is seen. If we ignore the energy band below 1.0 keV, the spectral fitting with a fixed temperature 8.0 keV is statistically acceptable with $\sim 1.4\%$ null-hypothesis probability.

The letter one (i.e. the 7th region of XMM-Newton) is also difficult to explain. Following Ogrean et al. (2013), we shifted the NXB by 10% to investigate systematic error possibly caused by the NXB fluctuation. The shift is $\sim$ 0.5 keV in ICM temperature and still cannot explain the difference of the MOS-derived high-temperature, to those determined from Suzaku and PN. It is known that PN and MOS often indicate different temperature as written in Sec.3.4 so here we consider that the results shall be because of such systematic difference. Therefore, we conclude that, basically, all satellites show consistent brightness, density, and temperature profiles, and what is more, the existence of shock as seen by the brightness jump and temperature increase is sure. The spectra of regions BR1–9 from XMM-Newton in the energy band of 0.8–7.0 keV are shown in Appendix.

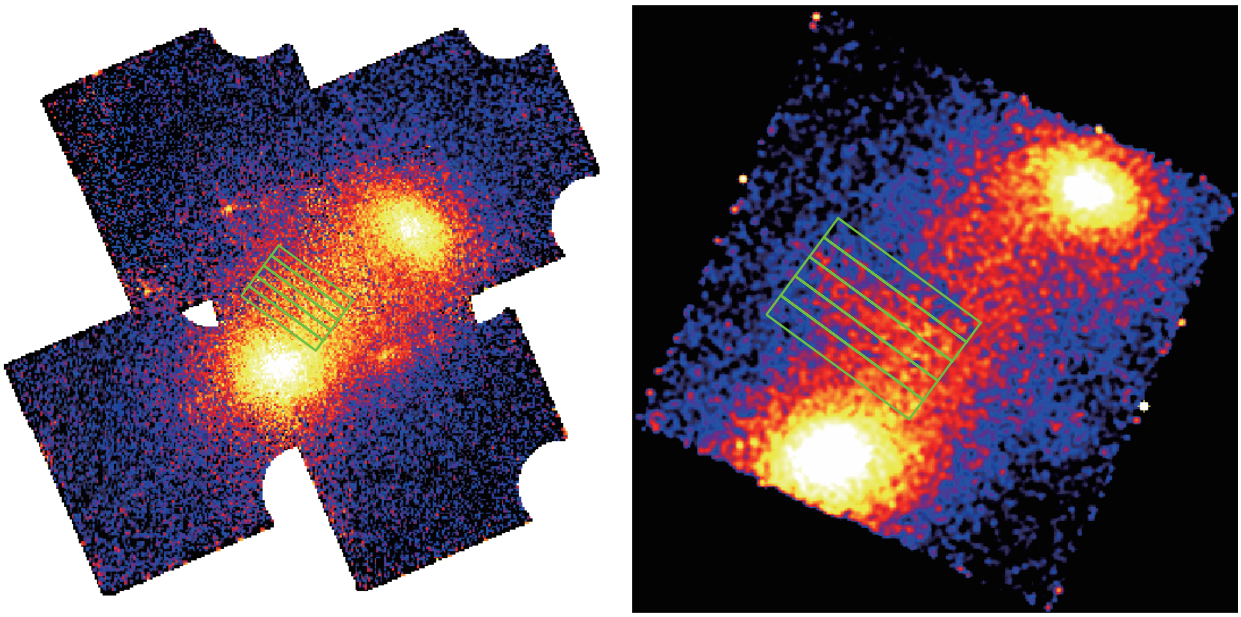

Figure 8.1: The images of Suzaku (left) and Chandra (right) superposed the regions where brightness and spectra are extracted.

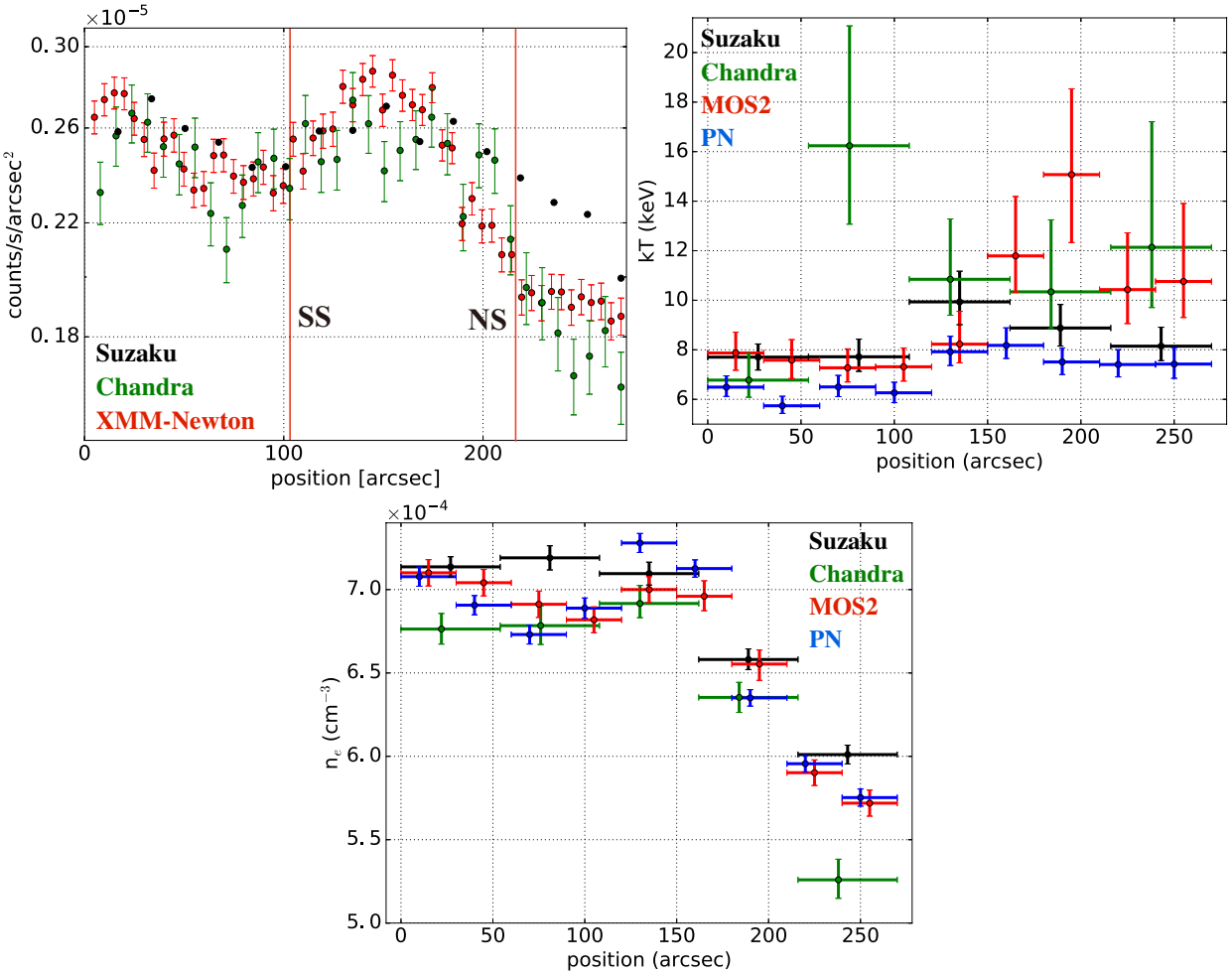

Figure 8.2: The brightness (top-left), temperature (top-right), and density (bottom) distribution of Suzaku (black), Chandra (green), and XMM-Newton (MOS2 in red, and PN in blue).

Chapter 9

Discussion

9.1 Overall observational results

We investigated the geometry and the phenomena induced in the ICM of CIZA J1359 with X-ray observations using Suzaku, Chandra, and XMM-Newton. The observations revealed following results.

- With Suzaku, a pair of clusters' cores and X-ray bright bridge structure between them were revealed.
- The spectra indicated that the two clusters have ICM temperatures of $\sim$ 6 keV and the bridge region has high temperature. The peak temperature reaches $11.5^{+2.6}_{-1.8}$ keV (Sec.5.2) by the Suzaku observation. The opposite directions of the bridge show a tendency of temperature decrease towards outside. These results are similar to the profile shown in simulations, such as Fig.1 and 2 of Poole et al. (2006,) as well as Fig.2 of Akahori et al. (2010). Hence, it is an explicit signature of an early-phase merger. The positional coincidence between X-ray peaks and elliptical galaxies also supports the view.
- The hot belt in the bridge region extends toward north-east direction while no strong heating is seen toward south-west direction (Sec.5.5).
- The brightness distribution extracted with both Chandra and XMM-Newton exhibit a twin transitions right on the temperature peak (Sec.6.2, Sec.7.2). These are clear signature of a twin shocks surrounding a brightness hump, which is considered to be a post-shock region.
- Chandra supreme angular resolution captured brightness transitions around both south-east and north-west clusters' cores (Sec.6.3). These are candidates of cold fronts in the early-phase mergers.

- Chandra and XMM-Newton found a candidate cavity structure in the bridge region in front of the temperature peak with size of about $80 - 240$ kpc, or an enhancement in X-ray emission to the north of this edge (Sec.7.3).

9.2 Detail of the shock structure

Fig.9.1 shows temperature cross-sectional views of the bridge region plotted along the five arrows shown as L, M, N, O, and P, obtained from the Suzaku observations. The profile along the N line shows two temperature jump at $x = 1' - 3'$ (or a single temperature peak at $x = 2'$). That of the O line shows a temperature jump at $x = 3' - 4'$. Although the profile in L, M, and P lines show hot components, strong temperature transitions are not seen. It is difficult to assess whether the hot temperature is caused by shocks or adiabatic compression in the lines in this "modest" regions. In many X-ray studies of ICM in merging clusters (e.g. Akamatsu et al. 2013), the pressure increase associated with that of temperature and with density increase is interpreted as a shock. Also, location of the pressure and temperature increase and the low Mach number suggested from them in CIZA J1359 are very similar to the properties of shocks predicted in the ICM simulation of merging clusters at their early phase (e.g. Akahori & Yoshikawa 2010, Gregory B. et al. 2006). We therefore conclude the temperature enhancement is caused by merger shocks.

The shock Mach number can be estimated from the temperature jump (see Sec.2.4), but line-of-sight effect and Suzaku's moderate angular resolution will all make it underestimated. Therefore, we decide to use N line so as to derive the Mach number of the shocks. The pre- and post-shock temperature of SS is $8.9^{+1.6}_{-1.2}$ and $11.5^{+2.6}_{-1.8}$ keV. The ratio provides a Mach number of $M_{SS} = 1.30^{+0.21}_{-0.16}$. As the same to SS, we also derived the NS Mach number of $M_{NS} = 1.44^{+0.21}_{-0.15}$ (Sec.5.4). On the other hand, temperature jump at other regions is a little modest. In other words, the highest derived Mach number is $M = 1.44^{+0.21}_{-0.15}$.

XMM-Newton observation also gives pre- and post-shock density of SS and NS. The derived Mach number of SS and NS are $1.04^{+0.01}_{-0.01}$ and $1.07^{+0.01}_{-0.01}$, respectively. These are smaller than the Mach numbers estimated from the Suzaku temperature. Although a careful handling will be needed, we interpret that this is caused by superposition effect of the line of sight.

Dozens of cluster mergers have regions bright in the radio band. This is because $\sim$ GeV electrons accelerated by the shocks emit diffuse synchrotron radiation in the GHz frequency band by interacting with a μG inter-galactic magnetic field (Sec.2.3). In Akahori et al. (2017), we executed observations of CIZA J1359 with a radio interferometer, Australia Telescope Compact Array (ATCA), in the energy band of 1.3–2.1 GHz to search such a diffuse emission. The detection sensitivity is set to be able to detect it with 10 σ if there is a typical diffuse radio emission observed in other merging clusters. However, no significant emission was found. This would be due to the small Mach number because the value is low even among cluster mergers shocks. Another possibility is that the shocks are too young and GeV electrons are yet to be generated. In this case, future observation with 100 MHz

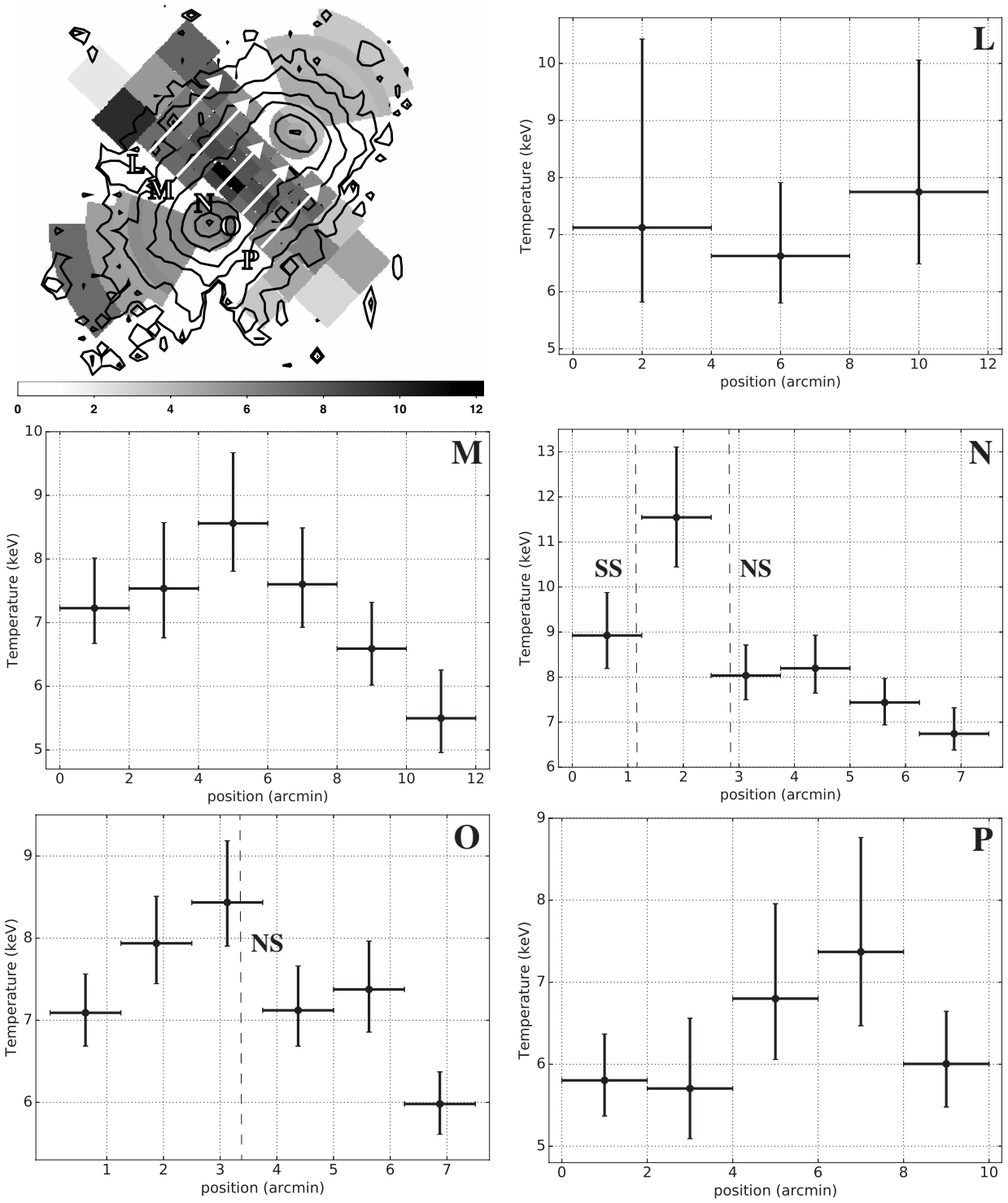

Figure 9.1: The same image as top left panel in Fig.5.5, but for shows the lines where temperature extracted (Top left). Temperature distribution along the arrows of top left panel.

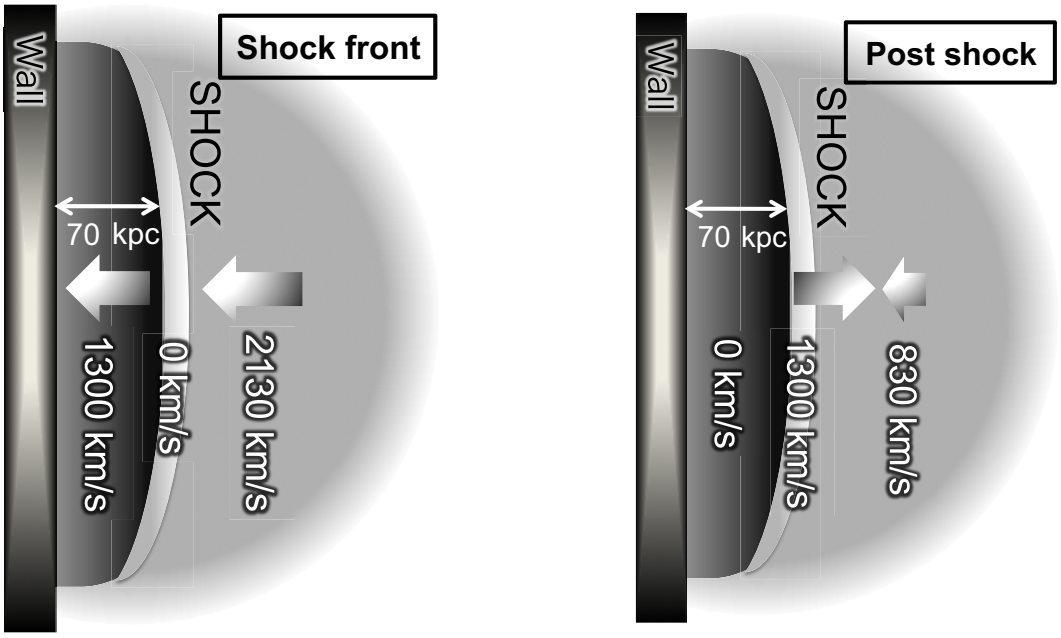

Figure 9.2: The shock geometry of CIZA J1359. On the system of the shock front (left) and the post-shock region (right), respectively.

band will give us better view.

The location of the shocks are around the middle between the pair of clusters, but are slightly closer to the south-east one. Generally, shape of clusters are elliptical (not completely spherical) and distance to the core does not necessarily mean the same ICM density nor the same gravitational potential depth (see, e.g. Fig.36 of Snowdon et al. 2008). Also, the shape of north-west ICM is apparently not spherically symmetric, which might indicate it was not fully dynamically relaxed when the collision started. Therefore, the slight shift of merger shock location can be presumably explained by the inherent modest ellipticity of the ICM distribution.

9.3 Estimation of merger geometry and the shocks age

The mass of the two clusters of galaxies merging in CIZA J1359 are similar, as described in Sec.5.3. Also, the Mach number of both NS and SS have almost identical values so that we can say the collision is almost symmetric. In other words, the merger geometry can be approximated as a major merger.

In principle, information of the existence of the shock cannot be propagated into the pre-shock region. Therefore, cold fronts have to be formed prior to the shock formation, when the ICM interaction has remained sub-sonic. From the above considerations, we illustrate the merger history as follows. First, two clusters attract each other with the huge gravity. The ICM of clusters began interacting each other. This will be in a similar situation as in

Table 9.1: Transition properties of each phenomenon

pre → post	kT	$n_{(density)}$	$P_{thermal}$	$S_{(entropy)}$
Shock	up	up	up	up
Cold front	down	up	equilibrium or down†	down
Cavity	equilibrium	down	down	up

† : When the ram pressure supports certain part of total pressure.

Abell 399–401 pair and Abell 222–223 pair. The ambient gas of clusters' cores are stripped steadily by the ram pressure, and then cold fronts were formed. As the merger proceeds, the gravity accelerated the colliding velocity and finally it reached the sound velocity of the ICM. Then, the shocks are activated, and they are running opposite directions each other and expanding the post-shock region. CIZA J1359 is considered to be in a timing, right after the formation of these shocks.

The sound velocity of ICM in the pre-shock region is 1550 km s^{-1} from the pre-shock temperature of 8.9 keV (Sec.5.3). Here, we use NS as a representative, and the Mach number of 1.4 derived from the temperature ratio. Because line-of-sight overlap of ICM emission always makes us under-estimate the shock value, here we used the highest one derived from the data. The pre- and post-shock region velocities are calculated to be 2130 km s^{-1} and 1300 km s^{-1}, respectively, when measured from the shock front. We illustrated the geometry in the left panel of Fig.9.2 as a cluster colliding into a wall (or under the assumption of a symmetry). In order to estimate the age of the shocks, we transform the coordinate from the shock front to post-shock region. In this standpoint the post-shock region must have the velocity of 0 km s^{-1} as illustrated in the right panel of Fig.9.2. Therefore, the shocks have a velocity of 1300 km s^{-1}. The distance between the twin shocks is 110" $\sim$ 70 kpc. Dividing the half of the distance by the velocity provides the shocks age of 55 Myr. The value is quite small, i.e. the shock is among the youngest as cluster merger shocks, since the dynamical evolution time scale of clusters of galaxies is as much as 1 Gyr.

With Chandra and XMM-Newton, we found a X-ray dim structure (or cavity structure) in front of the NS. Although the cavity itself can be considered to be the pre-shock (and hence lower density) region at NS, the northern edge of the cavity (see Fig.7.3) is not well understood yet. The edge shows no significant temperature jump in the Suzaku (for example in the N line in middle right panel of Tab.9.1) observation, while density shows a decline in the XMM-Newton observation. It indicates thermal pressure decline and entropy increase from north-south direction. The transition properties are summarized in Table.9.1. For comparison, the properties of shocks and cold fronts are also shown. Although current data is not enough to conclude its origin, the feature is apparently different from shocks or cold fronts.

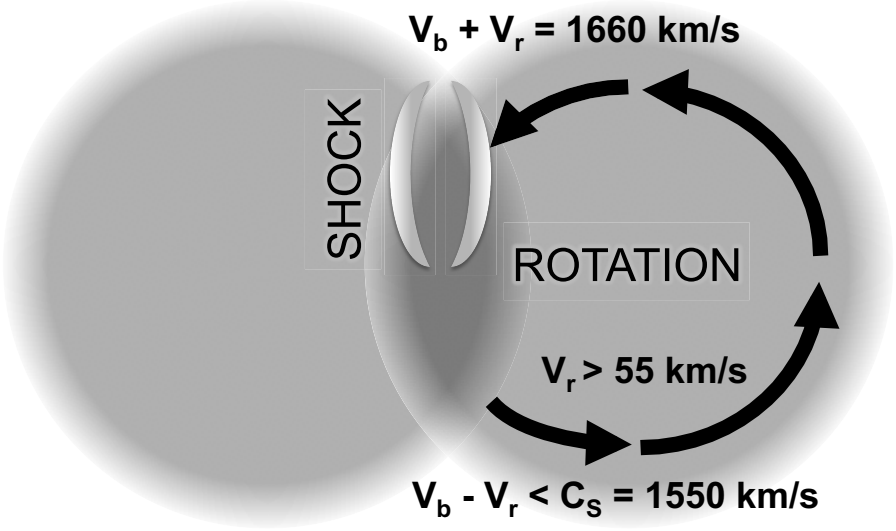

Figure 9.3: The illustration of rotating scenario. V_b and V_r are the bulk and rotation velocity, respectively.

9.4 East-west anisotropy of hot-belt and possible outflow

We assumed a symmetric collision in the previous section. South-west direction, however, does not show strong brightness transition in the bridge region, while north-east direction does. It suggests the shocks are only activated in the north-east region of the bridge region. The temperature distribution also supports the view. It indicates the asymmetry of the collision. Because the interaction of two body must be axisymmetric, the left-right difference (or chiral asymmetry) cannot be easily produced. On the other hand, because the Mach number is not so large, relatively minor effect can cause this difference. Two simple cases will be (1) initial rotation of the north-west and/or south-east clusters, and (2) existence of a third cluster in between. The 2nd candidate invokes variety of possibilities and hence not easy to restrict the condition. We also observe no candidate remnant of the 3rd cluster (i.e. the 3rd core). Thus, here we briefly discuss about the 1st scenario.

Provided clusters are rotating, the direction of rotation has higher colliding velocity than the opposite direction. Then, there can be a case that only one side exceeds the sound velocity while the opposite side cannot. In such a circumstance, the asymmetrical shocks shape is explainable. In the situation of CIZA J1359, the colliding velocity is approximated as 2×830 km s^{-1} (Sec.9.2), and it should be equal to the sum of the bulk velocity (V_b) and rotating velocity (V_r) as shown in Fig.9.3. Here, we assume that the north-west cluster is rotating counterclockwise. The south-west region must have the colliding velocity of $V_b - V_r < 1550$ km s^{-1} (the sound velocity) not to activate the shocks. In order to satisfy

the above condition, the rotation velocity is required to be only > 55 km s^{-1}. The value is very low and would be possible. In other words, if 0.1% of the kinetic energy resides in rotation motion, it is enough to invoke such axisymmetry. The situation is caused when the colliding velocity is almost equal to the sound velocity and the shock generation conditions are nearly in its threshold. Hence, this is a peculiar case seen only within a short duration of right after the development of shocks. The derived Mach number of ~ 1.4 supports this view.

As described in Sec.5.5, the hot components extend to up to $14' \sim 1100$ kpc towards north-east direction from the line connecting the two cores, and show sudden temperature decline. This could be simply the northern end of the shock, but the temperature and density jump are very significant, and cannot be easy to explain the suddenly break of such a strong shock. We considered three possible scenarios to explain the discontinuity, 1) gas eruption towards the north-east direction, 2) a sound wave generated when the clusters began the merger, 3) perpendicular shocks to merger axis activated by mass accretion from yet unknown filaments to the north-east of large scale structure.

The gas eruption can be induced by the adiabatic (or free) expansion of the heated and out-going gas from the higher-density central region of the bridge towards the lower-density north-east direction, generated via the combination of the shocks formation or adiabatic compression in the bridge and the merger anisotropy. Generation of such anisotropy is generally consistent with our cluster rotation scenario, while we need to wait for detailed merger simulations to verify if such an outflow can be initiated. Since the temperature of the hot region is considerably higher than those in the outside, and therefore the sound velocity of the inner region is significantly higher than that in the outer region, the outflow possibly develops another shock proceeding perpendicular to the merger axis.

A sound wave is basically an adiabatic change and thus conserves entropy in an ideal gas. Because the observed entropy shows a huge transition from 2790^{+3040}_{-1090} to 970^{+1180}_{-310} keV$\cdot$cm^2, the explanation of sound wave is not plausible.

The third candidate is infalling matter from a filament east-north-ward. In Akamatsu et al. (2016), they found a similar temperature transition in Abell 399-401 pair, which is an early phase cluster merger in a little earlier stage than CIZA J1359, in the direction perpendicular to the merger axis. They interpreted the transition is caused by a shock perpendicular to the merger axis generated by mass accretion from a filament of large scale structure. They considered that the merger increases the mass of the intermediate region, and it boosted the accretion medium velocity from a filament enough to generate a shock. It could be possible in our situation as well, however, it needs a peculiar geometry in which a filament is connected to the intermediated region. We checked galaxy distribution in CIZA J1359 and could not find such a filament structure, although the number of galaxies in the list is small. Hence, an extensive optical observation is necessary to pursuit (or reject) this scenario.

At the first look, we conclude that the eruption scenario is plausible. If this is true, this kind of eruption must be ubiquitously seen in many of the early stage mergers. With future high-sensitivity X-ray observations, eruption signatures similar to those seen in CIZA J1359

will be frequently observed. If we interpret the discontinuity as a shock, pre- and post-shock region temperature of $2.3^{+1.7}_{-0.4}$ and $7.8^{+5.2}_{-1.8}$ keV postulate a strong shock, with a Mach number of $\sim 2.9^{+1.5}_{-0.5}$.

9.5 Future prospects

The X-ray surface brightness of the shocks in CIZA J1359 is one of the largest among the cluster mergers. Especially, the pre-shock region is about 10 times brighter than that of the western-shock of the bullet cluster, which has been studied well with a long exposure Chandra observations as a textbook example of a shock (M Markevitch et al. 2001). Also the post-shock region is among the brightest one known to date. Since CIZA J1359 is the nearest of such examples, it will be the best target to study the spectral, spacial, and kinetic structure in the ICM shock in detail. Also, its very low Mach number provides unique coverage of the parameter space to understand the ICM shocks.

In 2020, the X-ray satellite XARM is supposed to be launched from Japan. It is a recovery mission of Hitomi launched in 2016. Hitomi onboard calorimeter had an energy resolution of ~ 5 eV, and was able to detect turbulent motion with an accuracy of $10 - 20$ km s^{-1}. The energy resolution is 20 times better than current X-ray observatories used in this thesis. Unfortunately, the satellite stopped the observations due to operation mistakes. XARM is equipped with the same calorimeter. The instrument can measure the width of fluorescent lines emission. We will be able to detect how much the turbulence is excited in the shock. It is pointed out that particle acceleration within cluster mergers would be caused by turbulences, because the locations of the shocks discovered with X-ray and diffuse radio emission sometimes show offset (Fujita et al. 2015). CIZA J1359 has bright shocks and show post-shock temperature of 10 keV, in which Fe kα fluorescent lines (~ 6.7 keV) emission is strong. Because the pre-shock region also is bright, the target will also provide how the turbulence is enhanced at the shock front.

ATCA was not able to detect diffuse synchrotron GHz radiation from $\sim$ GeV electrons accelerated by the shocks. Therefore, better sensitivity additional radio observation is necessary to investigate further. Outstanding radio interferometers such as Low-Frequency Array and Giant Meterwave Radio Telescope are located in northern hemisphere. CIZA J1359 is, however, located in near the south pole. It has been a obstacle for deeper radio observations. Square Kilometer Array is going to work in 2020s with 100 times higher sensitivity than current radio observatories covering the sky of deep south. It will reveal the property of particle acceleration in the early-phase merger.

Chapter 10

Conclusion

In this thesis, we explored plasma structures within CIZA J1359 with Suzaku, Chandra, and XMM-Newton. Following results are revealed .

- The pair of clusters are in an early phase merger. The bridge structure is constructed by the interaction. The hot component there is generated by adiabatic compression and shocks. At the other side of the two cores, the overall temperature structure is consistent with normal cluster, which further strengthens the early-merger scenario.
- In the bridge region, a twin shocks running opposite directions each other are activated. Based on the temperature jump from pre- to post shock regions, the colliding velocity is derived as 1660 km s^{-1}. The age of the shocks are estimated as 55 Myr, and hence a quite young example as cluster merger shocks compared to typical dynamical timescale of them.
- The anisotropy of hot belt or shocks shape between north-east and south-west regions is clearly observed. It can be explained by a small velocity rotation of the two clusters of galaxies. Also we discovered a temperature and density jump at 1.1 Mpc north-east to the shock axis. This jump can be a shock front or just the edge of the expanding hot gas, triggered by the gas out-flow from center of the bridge region.
- The brightness of both the pre- and post-shock regions are one of the most largest. Therefore, the object is very promising target for XARM or other X-ray missions in the future to measure the turbulence excitation in the post-shock region as well as the pre-shock region which is apparently already compressed to some extent by the ICM interaction. Also, our team has shown that the shock is not a bright GHz synchrotron emitter. Search for such emission at the 100 MHz band will be also important to understand the efficiency of particle acceleration.

References

Abell, G. O., Corwin, H. G., Jr., & Olowin, R. P. 1989, ApJS, 70, 1

Akahori, T. & Yoshikawa, K. 2008, PASJ, 60, 4,

Akamatsu, H. & Kawahara, H. 2013, PASJ, 65, 16

Akamatsu, H., Gu, L., Shimwell, T. W., Mernier, F., Mao, J., Urdampilleta, I., de Plaa, J., Rottgering, H. J. A., & Kaastra, J. S. 2016, A&A, 593, id.L7

Aschenbach, B. 2002, in Society of Photo-Optical Instrumentation Engineers (SPIE) Conference

Briel, U. G., Finoguenov, A., & Henry, J. P. 2004, A&A, 426, 1

Chandra IPI Teams. 2017, The Chandra Proposers' Observatory Guide, Version 20.0

Clarke, T. E. 2004, Journal of Korean Astronomical Society, 37, 337

Cravens, T. E. 2000, ApJ, 532, 2

Ebeling, H., Mullis, C. R., Tully, & R. B. 2002, ApJ, 580, 774

Finoguenov, A., Sarazin, C. L., Nakazawa, K., Wik, D. R., & Clarke,T. E. 2010, ApJ, 715, 1143

Fujita, Y., Takizawa, M., Yamazaki, R., Akamatsu, H., Ohno, & H., 2015 ApJ, 815, 2

Juda, M., Bloch, J. J., Edwards, B. C., McCammon, D., Sanders, W. T., Snowden, S. L., Zhang, J. 1991, 367, 18

Kalberla, P. M. W., Burton, W. B., Hartmann, D., Arnal, E. M., Bajaja, E., Morras, R., Poeppel, W. G. L. 2005 A&A, 440 775

Kato, Y., Nakazawa, K., Gu, L., Akahori, T., Takizawa, M., Fujita, Y., & Makishima, K., 2015, PASJ, 67, 4

Kocevski, D. D., Ebeling, H., Mullis, C. R., & Tully, R. B. 2007, ApJ, 662, 224

Kushino, A, Ishisaki, Y., Morita, U., Yamasaki, N. Y., Ishida, M., Ohashi, T., & Ueda, Y. 2002, PASJ, 54, 327

Lodders, K., Palme, H., Gail, & H.-P. 2009, LamB

Makishima, K., et al. 2000 ApJ, 535, 2

Markevitch, M. et al. 2000, ApJ, 541, 542

Markevitch, M., Vikhlinin, A., & Mazzotta, P. 2001, ApJ, 562, L153

Mitsuda, K., et al. 2007, PASJ, 59, 1

Nakazawa, K., et al. 2009, PASJ, 61, 339

Neumann, D. M. 2005 A&A, 439, 2

Ogrean, G. A., Bruggen, M., van Weeren, R. J., Rottgering, H., Croston, & J. H., Hoeft, M. 2013, MNRS, 433, 1

Poole, G. B., Fardal, Mark A., Babul, Arif, McCarthy, Ian G., Quinn, Thomas, & Wadsley, James. 2006, MNRS, 373, 3

Pottschmidt, K., ISAS/JAXA, & the X-ray Astrophysics Laboratory, NASA/Goddard Space Flight Center. 2015, The Suzaku Technical Description, Version: January, 2015

Rybicki, G. B. & Lightman, A. P. 1979, Radiative process in astrophysics (New York Wiley-Interscience)

Sakelliou, I. & Ponman, T. J. 2004, MNRAS, 351, 1439

Schellenberger, G., Reiprich, T. H., Lovisari, L., Nevalainen, & J., David, L. 2014, A&A, 575, id.A30

Serlemitsos, P. J., et al. 2007, PASJ, 59, 9

Snowden, S. L., Egger, R., Freyberg, M. J., McCammon, D., Plucinsky, P. P., Sanders, W. T., Schmitt, J. H. M. M., Trumper, J., Voges, W. 1997, ApJ, 485, 1

Snowden, S. L., Mushotzky, R. F., Kuntz, K. D., & Davis, D. S., 2008 A&A, 478, 2

Spitzer, L. 1965, Physics of fully ionized gases (New York: Interscience Publication)

Struder et al. 2001, A&A, 365, L18

Suto, Y. 2002, Gingadan no tahacho kansoku to utyuron (Observation of cluster galaxies with multiwavelength and Cosmology)

Takizawa, M. 1999, ApJ, 520, 514

Tawa, N., et al. 2008, PASJ, 60, 11

Turner, et al. 2001, A&A, 365, L27

Uchiyama, Y. 2008, PASJ, 60, S35

Vikhlinin, A., Markevitch, M., & Murray, S. S. 2001, ApJ, 551, 160

Vink, J., 2012 A&A, 20, 49

Weinberg, S. 2008, Cosmology (Oxford University Press)

Werner, N., Finoguenov, A., Kaastra, J. S., Simionescu, A., Dietrich, J. P., Vink, J., & Bohringer, H. 2008, A&A, 482, L29

XMM-Newton Community Support Team & XMM-Newton Science Operations Centre Team. 2014, XMM-Newton Users Handbook, Issue 2.12

Zwicky, F., 1937, ApJ, 86, 217

Acknowledgement

First, I would like to express my sincere gratitude to my supervisor Dr. Kazuhiro Nakazawa. He has a lot of enthusiasm, and supported and encouraged me incessantly for five years. I learned from him how to conduct research, and he let me experience various things through research. Without him, I was not able to come this far.

I am very grateful to Dr. Gu, Dr. Fujita, Dr. Takizawa, Dr. Akahori, and Dr. Aurora. They always gave me a lot of knowledge regarding clusters of galaxies. Their inspiring opinions and comments always helped me.

Dr. Makishima and Dr. Bamba were always supportive and advised me. I sincerely appreciate their kindness.

I have been helped by a lot of people. I wish to express my deep appreciation for the everyone who supported me.

Appendix A

Spectra of BR1–BR9

The XMM-Newton spectra obtained from regions BR1–BR9 in Sec.8. Those from BR1–6 are shown in Fig.A.1, and those from BR7-9 are in Fig.A.2. In Fig.A.3, we present the residual ratio of the PN and MOS2 spectra in the region BR7, with a fixed temperature of 10 keV. Apparently, MOS2 has a hump above 5 keV, which is causing the fitted-temperature difference.

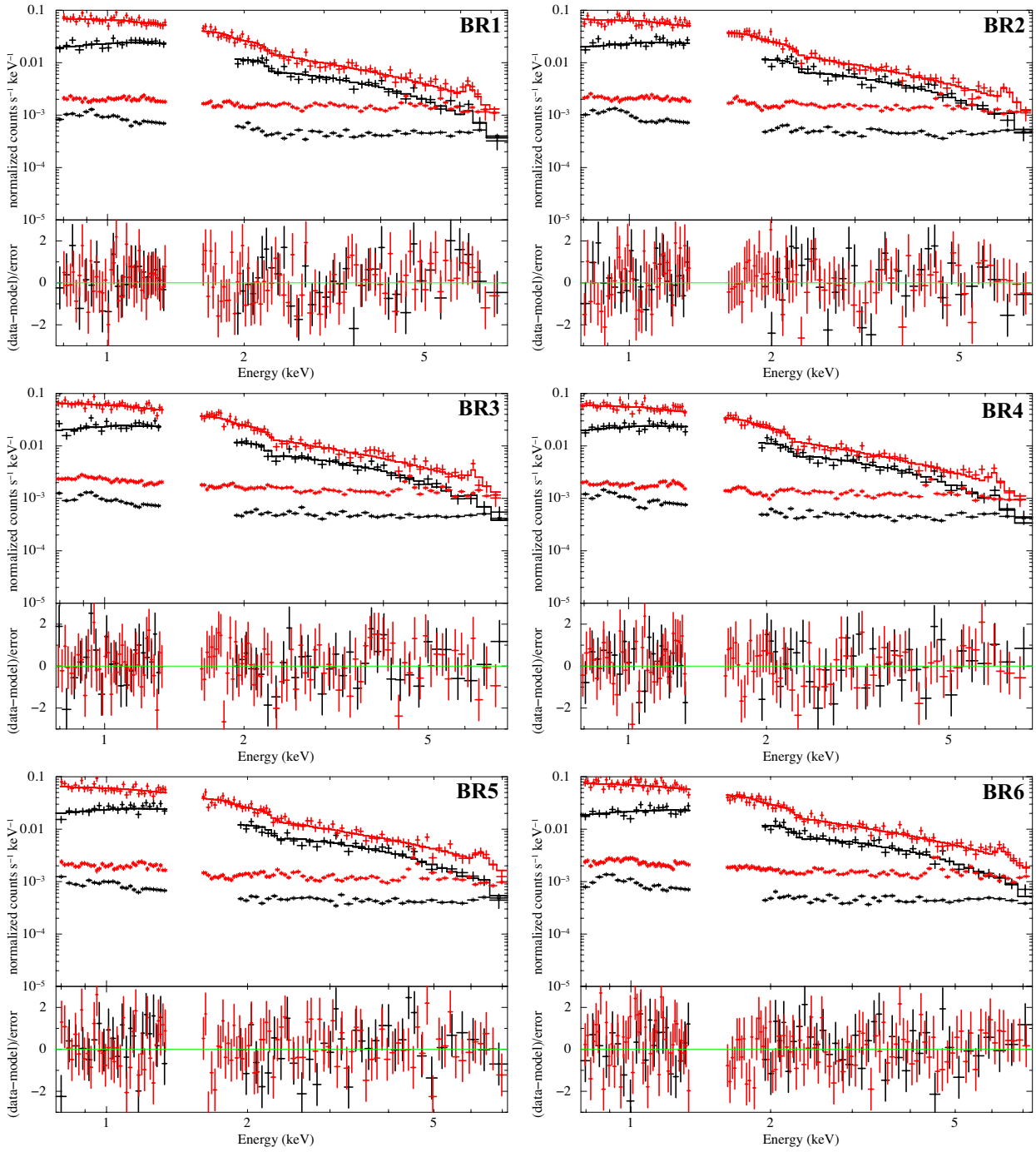

Figure A.1: The spectra of BR1–BR6. Black and red express MOS2 and PN, respectively.

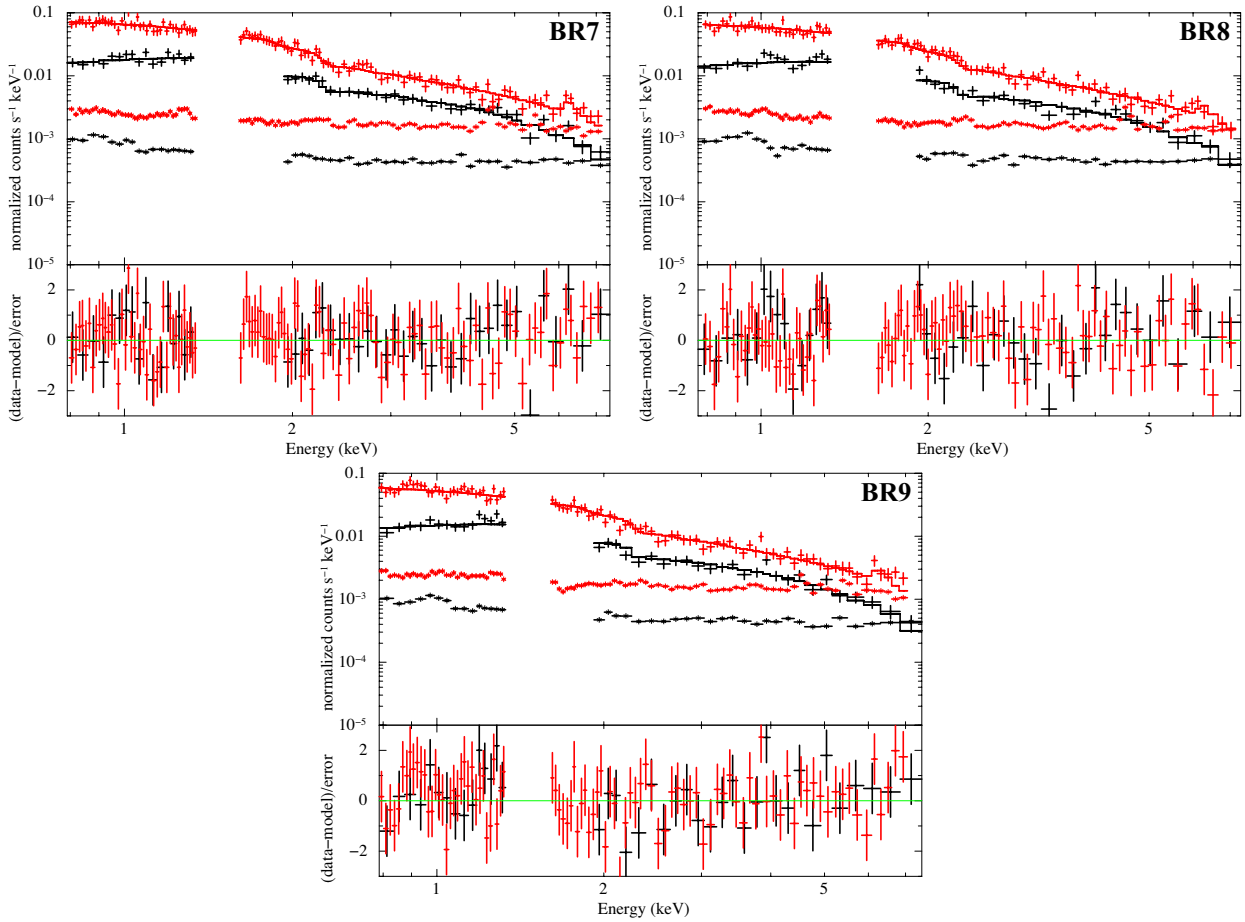

Figure A.2: The spectra of BR7–BR9. Black and red express MOS2 and PN, respectively.

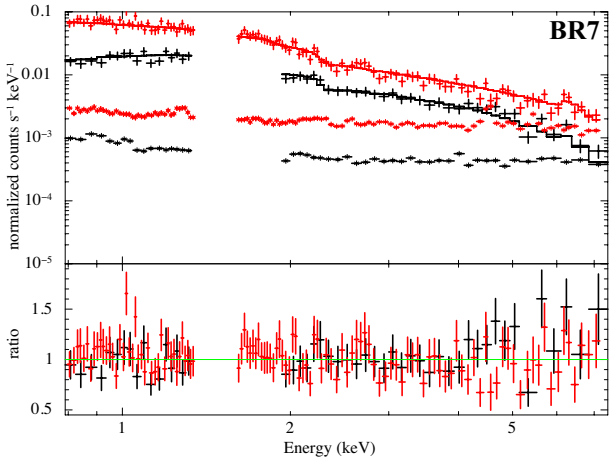

Figure A.3: The residual ratio of the PN and MOS2 spectra of BR7, fitted by a thermal model with a fixed temperature of 10 keV.